Gøril Jahrsengene

Coke Impurity Characterisation and Electrochemical Performance of Carbon Anodes for Aluminium Production

Gøril Jahrsengene

Doctoral thesis

NTNU
Norwegian University of Science and Technology
Thesis for the Degree of
Philosophiae Doctor
Faculty of Natural Sciences
Department of Materials Science and
Engineering

⊡ NTNU
Norwegian University of
Science and Technology

⊡ NTNU

Gøril Jahrsengene

Coke Impurity Characterisation and Electrochemical Performance of Carbon Anodes for Aluminium Production

Thesis for the Degree of Philosophiae Doctor

Trondheim, November 2019

Norwegian University of Science and Technology
Faculty of Natural Sciences
Department of Materials Science and Engineering

◻ NTNU

Norwegian University of
Science and Technology

Preface

This thesis has been submitted to NTNU, Norwegian University of Science and Technology, in partial fulfilment of the requirements for the Degree of Philosophiae Doctor.

The work was mainly performed at the Department of Materials Science and Engineering (IMA) at NTNU in Trondheim from 2015 to 2019. The work was supervised by Ann Mari Svensson (main supervisor, Professor, NTNU), Arne Petter Ratvik (Senior Research Scientist, SINTEF), Lorentz Petter Lossius (Principal Engineer, Hydro Aluminium) and Richard Haverkamp (Professor, Massey University). Part of the experimental work was carried out by visiting synchrotron facilities; the SXRMB (06B1-1) beamline at the Canadian Light Source (CLS) located in Saskatoon, Saskatchewan, Canada, and the XAS beamline at the Australian Synchrotron, one of the facilities of the Australian Nuclear Science and Technology Organization (ANSTO), located in Clayton, Victoria, Australia.

The work was mainly funded by the Norwegian Research Council and the partners Hydro Aluminium, Alcoa, Elkem Carbon, and Skamol through the project "Reactivity of Carbon and Refractory Materials used in Metal Production Technology" (CaRMa). Work on CLS was supported by the Canadian Foundation for Innovation, Natural Sciences and Engineering Research Council of Canada, the University of Saskatchewan, the Government of Saskatchewan, Western Economic Diversification Canada, the National Research Council Canada, and the Canadian Institutes of Health Research. Work on the Australian Synchrotron was funded by ANSTO. ANSTO also assisted with travel funding and accommodations for two of the participants. The accommodations for a visit at the University of Massey, New Zealand, was funded by Massey University.

All experimental work presented in this thesis has been conducted by the author, except the following:

Chapter 4: Rain Carbon did the CO_2 reactivity test. Hydro Årdalstangen did the XRF analysis of the cokes. The work on the optical texture analysis was performed by Stein Rørvik (SINTEF). The synchrotron data from CLS was obtained by working in shifts. The team consisted of Svensson, Haverkamp, Hanna Wells

(Massey) and the author, supervised by beamline scientist Yongfeng Hu. The processing and analysis of the synchrotron data was all performed by the author.

Chapter 5: Hg porosimetry was performed by Jannicke Kvello (SINTEF), and initial analysis of these results done by Rørvik.

Chapter 6: The air reactivity test was performed at Hydro Årdalstangen. The synchrotron data from the Australian Synchrotron was obtained by working in shifts. The team consisted of Haverkamp, Wells, Katie Sizeland (ANSTO), Camilla Sommerseth (SINTEF) and the author, supervised by beamline scientist Peter Kappen. The processing and analysis of the synchrotron data was performed by the author, with guidance from Haverkamp, and initial fitting by Haverkamp and Wells. Haverkamp did the literature search for the discussion in 6.3.8.

Chapter 7: The pilot anodes were made and physically characterised, as described in 7.2.2 and presented in 7.3.1, at Hydro Årdalstangen. Aksel Alstad (NTNU) assisted in preparing the test pieces used for the electrochemical tests.

All co-authors listed for each paper contributed to the corresponding discussions.

<div style="text-align: right">

Gøril Jahrsengene
Trondheim
September 6th, 2019

</div>

Acknowledgements

First, I would like to thank my main supervisor, Professor Ann Mari Svensson. I have really enjoyed our time together working on this project, and you have always been patient with me when I needed it. Your knowledge on, especially, electrochemistry, which I had little experience with before starting with this work, and carbon materials, have been a fundamental part of our discussions. I also appreciate the opportunity you allowed within this project to try methods not familiar to our department. This resulted in work I found extremely interesting, as well as exciting travels which you also were a part of. Thank you for all your guidance and support!

I also want to thank my co-supervisor Professor Richard Haverkamp from the School of Engineering and Advanced Technology, Massey University. You had many exciting ideas on characterising elements, and within the first half-year of my PhD our first proposal was sent in. You always got back to me and prioritised me when I needed you to do so. Thank you so much for the opportunity to work with you, and for welcoming me to New Zealand!

My two other co-supervisors, Dr. Arne Petter Ratvik from SINTEF and Dr. Lorentz Petter Lossius from Hydro Aluminium, you have both been a large part of this work and helped me on discussions on my papers. Thank you both so much.

This work was a part of the CaRMa project, and I want to thank the participants of this project, both from our industrial partners Hydro, Alcoa, Elkem, and Skamol, and the group from NTNU and SINTEF. I am very happy with the opportunities I had as part of this project to travel to conferences and present my work, which you always encouraged. I have also appreciated the close collaboration between NTNU and SINTEF this project facilitated. Tor Grande and Zhaohui Wang, all your feedback has been important. Stein Rørvik, we have collaborated a lot on this project, and besides help with imaging of the samples, you were a big part of the initial discussions on coke quality and properties. Henrik Gudbrandsen, thank you for all your help in the lab, and Egil Skybakmoen, thank you for all your encouragement and insisting that I apply for a job in your group. I am looking forward to working more with all of you!

Working with anodes, one very important person has always been around. Camilla Sommerseth, the knowledge you transferred to me over these years, the help you gave me in the lab, and the pep-talks you gave me when things weren't going as I

iv

hoped, are some of the reasons I am able to finish this work today. Thank you so much for all your help, I really enjoyed working with you.

To Les Edwards from Rain Carbon, thank you for showing interest in my work, helping me with my coke characterisation, and all discussions on my result both on email, on the phone and in person. I look forward to meeting up again!

I appreciate the help of all engineers and equipment responsible personnel I have encountered over the years. A special thanks goes to Anne Støre, Elin Albertsen, and the engineers from the electrochemistry group, Magnus Følstad and Anita Storsve. Aksel Alstad, from the workshop, the anodes I worked with would never have been made if it was not for you. Our talks when I joined you in your lab made me realise how much work is behind just making the anodes. Thank you for insisting that I listen!

These last years in the department have of course included a lot of people, who made the life as a PhD a lot easier. Everyone in K1, we had many great lunches together. The electrochemistry group, thank you for all seminars and social gatherings. To all that showed up for the DoktorandØl gatherings at one time or another, we had a lot of fun. I especially want to thank the PhD students working on other parts of the aluminium production process as part of CaRMa. Trond and Raymond, it has been great to have you both in the neighbouring office. Samuel, my office mate, ever since you started your work a little after the rest of us, we have had many discussions, both scientific and non-scientific, and you always made me smile when you sang and danced behind your screen when you forgot I was there. I hope we will be colleagues for many years to come!

To my friends outside of work, you know who you are, you have made life in Trondheim so wonderful.

Last, but not least, I must thank my family. Everyone has always showed a lot of interest in my work, without really having a lot of background to do so. A special thanks goes to Sondre, my brother, it was wonderful to have you here in Trondheim for four years, and my parents Mari and Geir. You guys always helped me when I needed it, if it was computer problems, moving, or just talk about life. This thesis would not have been if not for your support and encouragement. Thank you all so much.

Summary

The aluminium production process uses consumable carbon anodes made from calcined petroleum cokes, recycled anode butts and coal tar pitch. The main ingredient is the coke, a side product from the petroleum refining industry. Declining coke quality of the cokes available for aluminium production is a consequence of changes in the petroleum industry and the high demand from the still growing aluminium industry. In the future, regular anode grade cokes, or sponge cokes, with more impurities, mainly sulfur, phosphorous and metals, as well as isotropic cokes, will have to be used to produce anodes.

Based on the crude oil composition, metals in cokes have previously been assumed to be present as organic complexes, but the nature of the metal compounds has previously not been determined for the petroleum cokes. X-ray absorption near edge structure (XANES) and extended X-ray absorption fine structure (EXAFS) on the metals V, Ni, and Fe, in industrially produced petroleum cokes, revealed that these metals are actually present as hexagonal metal sulfide compounds. The metal sulfides are likely highly dispersed in the coke and not present as inclusions, and the metal chemistry was the same in all cokes investigated.

Sulfur was discovered by XANES to be present in the cokes as two distinguishable chemical compounds. Sulfur bound organically as polycyclic thiophene and thiazines as a part of the carbon sheets was expected, and was confirmed to be the main sulfur compounds in all cokes. However, in some cokes, independent of total sulfur level, a large fraction of the sulfur was clearly a different compound, which has not previously been observed in these quantities in cokes. This sulfur compound was identified as a S-S bound type of sulfide, but the exact type of compound could not be determined. The metal sulfides found by metal speciation could not account for all the S-S sulfide discovered in some of the cokes upon investigation of the sulfur speciation. The amounts of S-S bound sulfur was found to correlate to both CO_2 reactivity and quantity of small pores in the coke.

Electrochemical characterisation on pilot anodes made from the well-characterised cokes showed that reaction overpotential was of similar magnitude for all anisotropic anodes. The isotropic anode, high in metal impurities, had higher double layer capacitance, a measure of the electrochemically active surface area, than all the anisotropic anodes in the 0.1-0.35 A/cm^2 region, improved

kinetics and a slightly lower reaction overpotential compared to the anisotropic anodes. A significant reduction, around 0.15 V, in potential amplitude associated with the formation of CO_2 bubbles on the anode surface, was observed for the isotropic anode, but also for the low-sulfur anisotropic anode. The last observation was attributed to the higher permeability of these anodes rather than the lower impurity content. The presence of pores, which are nucleation points for gas bubbles, and the pore sizes, is probably important for the effect observed; the larger pores observed for anodes with a high permeability is likely to facilitate slower growth of bubbles that screen the surface less. The positive effects observed for the kinetics of the isotropic anodes are therefore attributed to a combined effect of coke and anode properties; the isotropic anode also had high permeability. No significant differences in overpotential or bubble behaviour was observed for anodes varying in impurity content with similar physical properties. The impurities, both sulfur and metals, did in this case not affect the electrochemical processes, which is a positive outlook regarding the use of more impure cokes in the future.

Contents

Chapter 1 Introduction

1.1 Motivation

The aluminium industry faces challenges concerning the availability of the primary raw material used to produce pre-baked carbon anodes, *i.e.* the calcined petroleum coke (CPC). Increased production of aluminium on a world-wide basis, much driven by the growth of the Chinese market [1], has led to higher demand of anode grade CPC. Although higher quantities of coke are produced from petroleum refining, the petroleum industry is shifting its production to heavier oils, which produces lower quality coke. Production of regular anode grade coke do not follow the demand from the aluminium industry, implying that lower quality coke will have to be introduced in the blends for carbon anodes [2]. This include using cokes with similar structure as the regular anode grade coke, where the most significant change is the impurity (*e.g.* sulfur and metal) content, but also accepting the use of isotropic cokes, which have a very different structure [3, 4]. The aluminium industry recognises this problem and is working towards utilising different types of coke in the best possible way.

While regular anode grade cokes have an anisotropic structure, the fuel grade cokes have an isotropic structure, and the introduction as anode raw material is not straightforward. Based on the risk of anode cracking due to the high thermal expansion of these types of cokes, a level around 20-30 % is proposed [3-5]. However, the effect of the increased impurity content associated with these cokes also needs to be evaluated. The isotropic cokes usually have a significantly higher metal impurity content, accompanied by a sulfur level much higher than used in the regular anode grade cokes. This is also the case for some cokes with anisotropic structure, which can be more easily incorporated in anode blends without the risk of cracking.

For the mixing of coke blends for anode production, certain requirements need to be met with respect to the overall content of impurities. First, several metallic impurities will end up in the metal, and specifications with respect to these must be followed. Second, some metallic impurities have previously been suggested to catalyse airburn and CO_2 reactivity, although there is still a lack of understanding. Regarding sulfur, a certain amount of sulfur is desirable in anodes, as it appears to reduce the CO_2 reactivity [6]. On the other hand, allowable emission levels of SO_2 into the work environment and off-plant are set by the government. Smelters have specifications on the coke sulfur level to uphold to make sure the emissions

are kept within the regulations [2, 7]. Many smelters are already operating close to their SO_2 limits and will need to make significant investments to be able to treat the produced gases when incorporating higher sulfur cokes in the anodes (*i.e.* by introducing scrubbers).

The knowledge of impurity compounds and effects of impurities on anode properties is still very limited, particularly with regards to possible effects on the electrolysis. A better understanding of how the lower quality cokes will affect the aluminium production process is clearly necessary, and of high interest for the aluminium industry.

1.2 Aim of Work

The overall aim of the work is to improve the understanding of effects of sulfur and metallic impurities in cokes on properties of the anodes for aluminium production, with a particular emphasis on the effects of sulfur. Knowledge on the sulfur and metal chemistry in the cokes is believed to be a stepping stone for several important evaluations concerning the decreasing quality of cokes. Five industrial cokes varying in sulfur content (1.4-5.5 wt%) have been investigated, of which four were anisotropic, and one isotropic in texture. There was also a large span in the level of metallic impurities in these cokes (760-2000 ppm total metal). Information on properties associated with sulfur was the initial focus, and the knowledge on how sulfur was bound chemically in the coke structure was believed to be a good foundation for these evaluations. X-ray absorption spectroscopy (XAS) utilise powerful synchrotron radiation to give information on *e.g.* sulfur speciation, but cannot be used on a regular basis as a control of coke quality. Possible correlations related to the sulfur compounds and other properties like reactivity and presence of micropores were also sought. Similarly to the sulfur speciation, the composition of three major metallic (V, Fe, Ni) impurities in the cokes were investigated by XAS techniques as well.

Pilot anodes made from these cokes were evaluated with respect to electrochemical reactivity. In order distinguish contributions from the various irreversible losses, different electrode configurations were used. This allows for assessment of the magnitude of voltage oscillations related to bubble screening, the overvoltage measured with practically no bubbles present, as well as recording of electrochemical impedance spectra in order to distinguish between reaction steps.

1.3 Structure of Thesis

The thesis is a collection of four individual papers, presented in Chapters 4-7. The papers have been re-formatted to fit with the format of the thesis. A technical introduction on aluminium production, with emphasis of the carbon anode, is presented in Chapter 2. All experimental procedures are summarised in Chapter 3, as well as some background and literature on the methods assumed known in the main papers.

Chapter 4: XANES was used to investigate the sulfur speciation in industrial cokes. The results were evaluated with respect to the CO_2 reactivity, which is believed to be reduced by sulfur. *Published in Metallurgical and Materials Transactions B, presented at TMS 2018.*

Chapter 5: The CO_2 reactivity and sulfur speciation was evaluated with respect to microstructural properties. This included accessible surface area, pore size distribution and surface chemistry. *Written as TMS conference proceedings, published in Light Metals 2019, presented at TMS 2019.*

Chapter 6: XAS techniques was used to investigate the metal speciation in industrial cokes. Metal sulfides could not be detected investigating the sulfur using the same technique because most sulfur is not being bound this way, but investigating the individual metals could reveal possible metal sulfides. Ni, V and Fe was investigated. Evaluations of the air reactivity is included. *Published in Metallurgical and Materials Transactions B, will be presented at TMS 2020.*

Chapter 7: The chapter focuses on electrochemical characterisation of anodes made from different industrial cokes, including the effect of bubble formation at the surface, reaction overpotential and double layer capacitance. Significant differences caused by coke properties and anode properties was sought, and the results discussed in relation to the previous coke characterisation results.

Chapter 8 summarises the conclusions from the main chapters. Chapter 9 evaluates possibilities for further work.

References

[1]   World Aluminium. *Primary Aluminium Production*, http://www.world-aluminium.org/statistics/ [Date of Issue: 22 July 2019]

[2]   L. Edwards. The History and Future Challenges of Calcined Petroleum Coke Production and Use in Aluminum Smelting. *JOM* (2015), **67**(2), pp. 308-321.

[3]   L. Edwards, N. Backhouse, H. Darmstadt and M.-J. Dion. Evolution of Anode Grade Coke Quality. *Light Metals* (2012), pp. 1204-1212.

[4]   L. Edwards, F. Vogt, M. Robinette, R. Love, A. Ross, M. McClung, R.J. Roush and W. Morgan. Use of Shot Coke as an Anode Raw Material. *Light Metals* (2009), pp. 985-990.

[5]   C. Sommerseth. *The Effect of Production Parameters on the Performance of Carbon Anodes for Aluminium Production.* PhD thesis. Norwegian University of Science and Technology, 2016.

[6]   G.J. Houston and H.A. Øye. Consumption of anode carbon during aluminium electrolysis. I-III. *Aluminium* (1985), **61**, pp. 251-254, 346-349, 426,428.

[7]   M.F. Vogt, J.H. Waller and R.D. Zabreznik. The Problem of Sulfur Content in Calcined Petroleum Coke. *JOM* (1990), **42**(7), pp. 33-35.

Chapter 2 Introduction to Aluminium Production and the Role of Carbon Anodes

2.1 The Hall-Héroult Electrolysis Process

Electrochemical production of aluminium, known as the Hall-Héroult process, is the only large scale industrially used method to produce primary aluminium metal [1]. The process was discovered by two individual scientists and patented by both, separately, in 1886; Charles Martin Hall in America and Paul Héroult in France. The basis of the method is reduction of aluminium oxide (Al_2O_3), dissolved in a molten electrolyte (mainly cryolite, Na_3AlF_6). Al^{3+} is electrochemically reduced to Al at the cathode, and the oxygen-containing compound in the melt oxidise the carbon anode to CO_2. The general reaction is given in Equation 2.1, while the reactions occurring on each electrode are more complex.

$$2Al_2O_3(diss) + 3C(s) \rightarrow 4Al(l) + 3CO_2(g) \qquad (2.1)$$
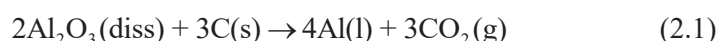
Today the most common way to produce aluminium is using an array of smaller (1000 kg) prebaked anodes. Previously the Søderberg one-anode-per cell configuration was more common. The transversal cross-section of a modern cell with prebaked anode technology can be examined in Figure 2.1. The cell has a steel casing lined with refractory bricks and insulation in the bottom. The carbon cathode has steel current collector bars slotted into the blocks, and the side wall is protected against wear by the circulating metal and bath by a sideledge of frozen cryolite. The top of the bath and top of the anodes are covered by a crust-like layer to avoid unwanted reactions with air. The alumina is usually point fed into the electrolyte at given intervals in an opening of the crust. The formed aluminium acts as the cathode, and the carbon anodes are lowered into the melt to keep an approximate constant distance between anode and cathode. Anodes are changed when approximately 75 % of the anode is consumed (depending on current density and size this occurs every 2-4 weeks); the butts are cleaned and reused in new anodes.

Other methods of producing aluminium has been under investigation since the discovery of the Hall-Héroult process. Disadvantages to the Hall-Héroult process include production of environmentally unfriendly gases, the excess consumption of anode carbon due to side reactions, and the high energy demand (including

significant amount of waste heat). Alternative methods studied include carbothermic reduction of alumina, which is a non-electrochemical process at much higher temperatures, and the use of an inert anode producing O_2 during electrolysis [2]. Currently, the company "Elysis" is developing a production method, envisioned to be available for commercialisation in 2024, that will eliminate the use of carbon anodes and produce oxygen [3]. Although the Elysis method is much anticipated by the industry, the Hall-Héroult process will be the main way to produce aluminium in many years to come.
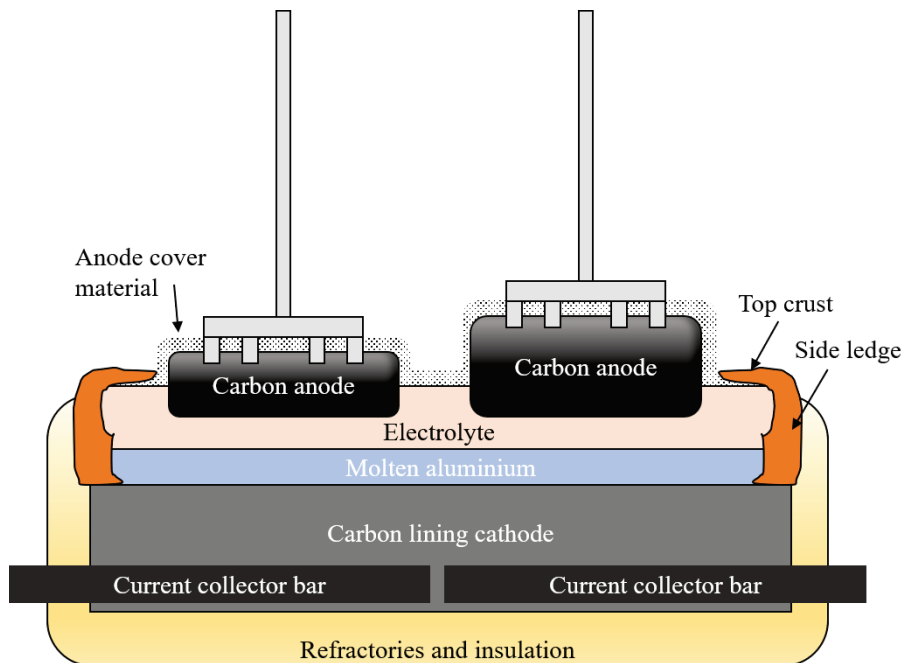
Figure 2.1: Sketch of Hall-Héroult cell transversal cross-section. Dimension is 3-4 meter across.

2.2 Carbon Anodes used in Aluminium Electrolysis

The consumption of carbon during Hall-Héroult electrolysis is high (typically 400-450 kg per tonne Al produced); a potline typically consists of hundreds of cells and each cell has arrays of 20-40 anodes. Carbon anodes are made of a mixture of calcined petroleum coke (CPC) (ca. 60-70 %), recycled anode butts

(ca. 15-20 %) and a coal tar pitch binder (ca. 12-18 %) and can be made onsite in a separate anode production plant, or produced elsewhere and brought to the aluminium smelter. The cokes used are usually a blend of different qualities, and a desired aggregate grain size distribution is achieved by fractioning and sieving, including the recycled anode butts. The materials are mixed with the pitch at a temperature about 50 °C higher than the pitch (Mettler) softening point. The mixture is formed to a solid block, the so-called green anode, by vibroforming or pressing. The green anodes are stacked within a pit furnace with 30 ton to 200 ton of anode per pit, and exposed to a two-to-three-week heat treatment with a maximum temperature of 1200-1250 °C [1]. The purpose is to carbonise the pitch binder into solid pitch coke and the product is the baked anode.

The balanced half-reaction on the anode during aluminium production is considered to be Equation 2.2, and is believed to consist of two electrochemical steps. Several versions have been proposed, for example Equations 2.3 and 2.4 [4]. The exact oxyfluoride compound is disputed, but the overall electrochemical oxidation reaction is assumed to proceed via an intermediate adsorbed specie CO_{ads}.

$$2O^{2-} + C \rightarrow CO_2 + 4e^- \tag{2.2}$$

$$Al_2O_2F_6^{4-} + C \rightarrow CO_{ads} + Al_2OF_6^{2-} + 2e^- \tag{2.3}$$

$$Al_2O_2F_6^{4-} + CO_{ads} \rightarrow CO_2 + Al_2OF_6^{2-} + 2e^- \tag{2.4}$$

Excess anode consumption in the potroom can be caused by chemical reactions between the carbon, air and the produced CO_2, *i.e.* Equations 2.5-2.7. The air reactivity is mainly controlled by covering the anodes (like in Figure 2.1), while the reaction with CO_2, the Boudouard reaction (Equation 2.7), may occur on any internal and external carbon surface on the anode, and also block the carbon-electrolyte interface. The coke quality, especially metal impurities, influence these reactions negatively, possibly as catalysts. This includes vanadium for the air reactivity, and iron for the carboxy reactivity, and nickel for both [5-7]. Sulfur is however believed to reduce the reaction with CO_2. Other effects on the reactions includes the degree of baking, and the electrolysis process itself through bath temperature, covering, and air intrusion. Cracking and dusting can also give higher consumption, as can the back-reaction (where CO is formed).

$$C(s) + O_2(g) \rightarrow CO_2(g) \tag{2.5}$$

$$2C(s) + O_2(g) \rightarrow 2CO(g) \tag{2.6}$$

$$C(s) + CO_2(g) \rightarrow 2CO(g) \tag{2.7}$$
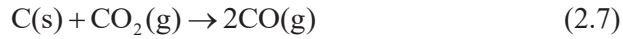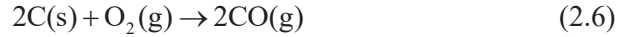
The electric potential used in industrial scale Al metal production is around 4 V, of which 1.5-1.8 V is the potential associated with the anode (w.r.t. Al potential) [8]. Given the reaction mechanism, Equation 2.2, there will inevitably be gas bubbles formed at the anode surface. The measured anode potential can be expressed as Equation 2.8 [9], where the bubbles formed on the surface will affect the irreversible losses.

$$E_{\text{anode measured}} = E^{\text{rev}} + \eta_c + \eta_r{}' + \eta_h + I(R_s{}' + \delta R_s) \tag{2.8}$$

Here, E^{rev} is the reversible potential, and η_c the concentration potential, which is small and might be neglected in alumina-saturated melts. η_r' and R_s' denotes the reaction overpotential and the ohmic resistance without bubbles. The term η_h, the hyperpolarisation, represent the change in overpotential due to reduction of surface area, and δR_s is the increased ohmic resistance due to the reduced surface area caused by bubble blockage. I is the current.

2.3 Petroleum Cokes

Petroleum coke is the main raw material used in carbon anodes for the aluminium electrolysis process. Understanding coke properties and identifying whether differences between cokes will affect the electrolysis process is of high importance to the industry. Coke is a carbonaceous material, or solid carbon, produced by the oil refining industry in the step called cracking (or other processes where similar steps are included) [10]. Heavy residual oil from the petroleum refining is converted into several high-end products and petroleum coke. Petroleum coke is therefore a speciality product from the petroleum refining industry. It should be noted that the entire refining process is optimised with respect to for the high-value products like diesel fuel and gasoline rather than coke. The resulting coke material is not optimised with respect to the needs of the aluminium industry and might be high in impurities and possesses non-ideal structures.

As many carbon materials, cokes can be classified with reference to the ideal graphite structure [11]. Graphite is a layered structure of carbon bonded in rings of six, and the layers are placed in a hexagonal lattice with an interlayer spacing of 0.335 nm. Graphite is anisotropic with regards to properties, *i.e.* the in-plane

and inter-plane properties are significantly different due to the sp^2-bonding. Higher electrical and thermal conductivity are observed in-plane, but both are low across the layers. Graphite is easily cleaved between layers, and chemical attacks can occur between layers or along the edges of the planes [10, 12].

During the coking process, the transformation from liquid phase to a solid phase occurs by dehydrogenation, ring closure, formation of C-C bonds, polymerisation and condensation (carbonisation). These reactions occur up to 600-800 °C, and the result is termed green coke (unprocessed coke). The conversion includes the formation of an intermediate liquid crystal phase, or a carbonaceous mesophase, and the resulting coke structure is partly dependent on how this mesophase develops [10]. Liquid phase crystallisation of the mesophase is for example critical for the development of highly anisotropic cokes. Other factors important to the structure are the coker operation and the feed composition.

Some carbon materials can, by high temperature treatment, transform from a structure with little order to one very close to pure graphite (graphitisation). These types of carbons are called graphitisable carbons, and usually must be heated to temperatures above 2400 °C to reach the ideal graphite structure. If a large variation in orientation is observed in the original crystallites (*i.e.* turbostratic groups) in the material, perfect graphite structure is not possible even with high temperature treatment [11]. Green cokes used in aluminium industry are calcined at temperatures no higher than 1350 °C. The structure of calcined petroleum cokes (CPCs) are thus far from an ideal graphite structure.

Green coke contains significant amounts of volatile matter and moisture. This is removed from the material by calcination, but only about ¼ of all green coke is calcined and subsequently used as anode material [1, 13]. Most of the calcined coke is used in anodes for aluminium production by the Hall-Héroult process. When the green coke has too high impurity content (*e.g.* metals and sulfur), typically found for cokes with an isotropic structure (see next paragraph), the coke is usually not calcined and is used as fuel.

2.3.1 Coke Classification
Cokes are frequently referred to as needle coke, anode grade coke or fuel coke, and a brief description of these is provided below.

Needle Coke: A graphitisable coke originating from highly aromatic crude oils with very low impurity content, and the resulting coke material is called needle coke. Because of the benzene rings already present in the crude, anisotropic coke is easily formed. Anisotropic cokes can be recognised by large sized optical flow

domains when examining them with polarised light (example in Figure 2.2a). The highly anisotropic nature of needle coke makes it very suitable for graphitisation. Needle coke is also referred to as premium-grade coke, is very expensive, and is most commonly used for electrodes in electric arc furnaces [13].

Anode Grade Coke: The type of coke most commonly used in the aluminium industry have many names, *e.g.* regular grade coke, calcineable coke, anode grade coke and sponge coke. The term sponge coke originates from the shape the coke grains; *i.e.* it usually appears like bubbles with significant porosity allowing pitch penetration. These cokes are less anisotropic than the needle coke, but by illuminating with polarised light, similar flow domains can be recognised in many grains. Although the sponge coke is usually classified as anisotropic, the structure can vary greatly, and some grains have a dominating isotropic structure similar to that of fuel coke [13].

Fuel Grade Coke: The previously mentioned fuel grade coke is highly isotropic and composed of small, hard and round particles resembling lead shots (giving the name shot coke). Shot coke is unfavourable in anodes because of the high thermal expansion and is high in impurities that can end up in the products. The isotropic grains are easily recognizable using light microscopy and polarized light because the fineness of the texture, normally referred to as a mosaic texture (Figure 2.2b).

(a)   (b)
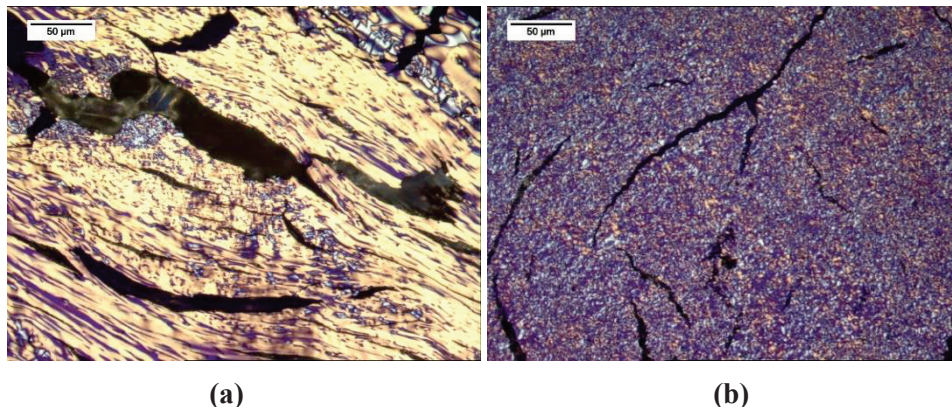
Figure 2.2: Examples of **(a)** anisotropic fibre fibrous texture typical of needle coke and **(b)** isotropic mosaic texture typical of fuel grade coke.

The definition of high, normal and low sulfur cokes are not definite and are subjected to change. An example is the definition by CII Carbon LLC, now Rain Carbon, which used to have normal sulfur cokes in the 2-3 wt% S range in 2008

[14]. Today, a common range of normal sulfur cokes are 2.5-3.5 wt% S, but arguments can be made to include even higher sulfur cokes in this range (*e.g.* aluminium smelters in India have maximum total specification for CPC at 3.5 wt% S and are likely to consider cokes up to 4 wt% S as normal). Some suppliers also use an additional term, ultra-low sulfur coke, for the cokes with less than 1 wt% S, as the low sulfur cokes now span a quite large range [15].

2.3.2 Sulfur and Metal Impurities in Petroleum Cokes

The aluminium industry is facing challenges concerning the availability of regular anode grade coke; the demand of sponge type coke material for the still growing primary aluminium industry is larger than what is produced as by-product from the oil refining industry. This does not mean there is a lack of carbon material, but the production of the previously considered anode grade coke is not increasing as fast as the demand from the aluminium industry. The petroleum refining industry are favouring sour crude oils over sweet oils, which contains more sulfur, metal impurities and have a higher specific gravity, because of availability and lower production cost. Consequently, the aluminium industry is incorporating lower quality cokes in their anodes. This is done by blending; sponge cokes with higher sulfur and metal content is mixed with the regular coke, as well as small portions of isotropic fuel cokes [13, 16, 17].

Sulfur in the anode is believed to have a positive effect on the chemical reaction that can occur between CO_2 and C (the Boudouard reaction), and for this reason it is considered beneficial to increase the total sulfur level of the anode by blending in high sulfur cokes [6]. However, sulfur will also end up as COS gas, which will increase the carbon consumption [18]. COS is further oxidised by air, and the result is that almost all sulfur containing potroom gas is SO_2. Sulfur desulfurization during baking is another concern of high importance, which will both produce sulfur gases and negatively impact anode properties (*i.e.* density and reactivity) [14, 19]. Understanding and considering these reactions with sulfur, as well as the role of the metal impurities which catalyse the chemical reactions between the anode, air and CO_2, when the total amount of impurities in the aluminium electrolysis process are increasing, are as important as the treatment of the SO_2 product.

References

[1]   J. Thonstad, P. Fellner, G.M. Haarberg, J. Híveš, H. Kvande and Å. Sterten. *Aluminium Electrolysis: Fundamentals of the Hall-Héroult Process.* 3rd ed. Aluminium-Verlag: Düsseldorf, 2001.

[2]   H. Kvande and P.A. Drabløs. The Aluminum Smelting Process and Innovative Alternative Technologies. *JOEM* (2014), **56**(5S), pp. S23-S32.

[3]   Elysis. *Carbon-free Aluminum, A New Era for the Aluminum Industry*, https://www.elysis.com/ [Date of Access: August 19th 2019]

[4]   A. Kisza, J. Thonstad and T. Eidet. An Impedance Study of the Kinetics and Mechanism of the Anodic Reaction on Graphite Anodes in Saturated Cryolite-Alumina Melts. *J. Electrochem. Soc.* (1996), **143**(6), pp. 1840-1847.

[5]   T. Eidet and J. Thonstad. Effects of Sulphur, Nickel and Vanadium on the Air and CO_2 Reactivity of Cokes. *Light Metals* (1997), pp. 436-437.

[6]   G.J. Houston and H.A. Øye. Consumption of anode carbon during aluminium electrolysis. I-III. *Aluminium* (1985), **61**, pp. 251-254, 346-349, 426,428.

[7]   T. Eidet, J. Thonstad and M. Sørlie. Effects of Iron and Sulphur on the Air and CO_2 Reactivity of Cokes. *Light Metals* (1997), pp. 511-517.

[8]   H. Kvande and W. Haupin. Cell Voltage in Aluminum Electrolysis: A Practical Approach. *JOM* (2000), **52**(2), pp. 31-37.

[9]   R.J. Thorne, C. Sommerseth, A.M. Svensson, E. Sandnes, L.P. Lossius, H. Linga and A.P. Ratvik. Understanding Anode Overpotential. *Light Metals* (2014), pp. 1213-1217.

[10]   Z. Bourrat. Structure in Carbons and Carbon Artifacts, in: *Sciences of Carbon Materials* H. Marsh, F. Rodríguez-Reinoso (Eds.). 1997.

[11]   I.A.S. Edwards and H. Marsh. *Introduction to Carbon Science.* Butterworths: London, 1989.

[12]   T. Foosnæs and T. Naterstad. Carbon: Basics and Principles, in: *Introduction to Aluminium Electrolysis, Understanding the Hall-Héroult Process.* K. Grjotheim, H. Kvande (Eds.). 1993.

[13]   L. Edwards. The History and Future Challenges of Calcined Petroleum Coke Production and Use in Aluminum Smelting. *JOM* (2015), **67**(2), pp. 308-321.

[14]   L.P. Lossius, K.J. Neyrey and L.C. Edwards. Coke and Anode Desulfurization Studies. *Light Metals* (2008), pp. 881-886.

[15]   L. Edwards.Communication on *Definitions on Sulfur in Cokes*. August 19th, 2019

[16]   L. Edwards, N. Backhouse, H. Darmstadt and M.-J. Dion. Evolution of Anode Grade Coke Quality. *Light Metals* (2012), pp. 1204-1212.

[17] L. Edwards, F. Vogt, M. Robinette, R. Love, A. Ross, M. McClung, R.J. Roush and W. Morgan. Use of Shot Coke as an Anode Raw Material. *Light Metals* (2009), pp. 985-990.

[18] S.J. Hay, J. Metson and M.M. Hyland. Sulfur Speciation in Aluminum Smelting Anodes. *Ind. Eng. Chem. Res.* (2004), **43**(7), pp. 1690-1700.

[19] L.C. Edwards, K.J. Neyrey and L.P. Lossius. A Review of Coke and Anode Desulfurization. *Light Metals* (2013), pp. 130-135.

Chapter 3 Experimental

This chapter gives an overview of the characterisation methods covered in chapters 4-7.

3.1 Coke Characterisation

3.1.1 General Coke Characterisation

Coke impurity quantities were determined by X-ray fluorescence (XRF) according to ISO 12980:2000 on the bulk coke.

Coke texture, used to confirm anisotropy and isotropy, was investigated using polarised light on a large selection on grains. A macro recognising singular pixels and continuous flow domains in the image was used to obtain two indexes; the mosaic index indicated isotropy (fineness of domain) and fiber index (alignment in domain) [1]. The variation between grains of the same coke could be evaluated based on the standard deviation.

A standard mass loss test (RDC equipment using ISO-12981-1 Standard RDC-1141) was used to determine the coke CO_2 reactivity (the Boudouard reaction). The CO_2 reactivity is routinely measured for cokes as well as anodes, however, air reactivity characterisation is usually reserved for the anodes only.

Pore size distribution was investigated by Hg intrusion porosimetry according to ASTM D4404-10. The method measures the volume of mercury, a non-wetting liquid that will not enter the pores by capillary actions, forced into pores by changing the external pressure. The pressure corresponds to the bottleneck, or entrance, of the pore, correlating this to pore diameter using the Washburn equation [2]. Assuming cylindrical pores, the pore area can be extracted, but in reality, it offers no information on the pore size inside the opening of the pore, and the method only include open pores. Thus, the data needs to be treated carefully; a small pore entrance but large interior pore (like an ink-bottle shape) will incorrectly register the entire pore as having the small diameter of the entrance. Other short-comings of the method include intrusion between the coke grains in the beginning of the experiment, and possible destruction of grains at high pressures. The sample size in this test is also very small.

Gas adsorption is a well-established way to characterise surface area and porosity of porous solids and powders. Advanced analysation of complex, porous, structures is possible, including procedures based on density functional theory

(DFT), and other simulation methods, using high resolution physisorption data. Nitrogen adsorption and desorption was performed on crushed coke particles, resulting in adsorption-desorption isotherms (*i.e.* the quantity adsorbed gas *vs* the relative pressure). Methods described by IUPAC [3] could be used to analyse the isotherms and hysteresis (*i.e.* when the adsorption and desorption graphs don't coincide), and compare to already known information about carbonaceous and porous materials. Standard pore classification in context of physisorption is macropores (> 50 nm), mesopores (2-50 nm) and micropores (< 2 nm). To investigate the smallest pores (*i.e.* for pores too small for the Hg porosimetry analysis) the Barret-Joyner-Halenda (BJH) pore size distribution and area [4] were extracted from the software of the instrument.

A temperature ramping program (using an oxygen-nitrogen-hydrogen analyser from LECO) with approximately 250 °C/min heating rate up to 3000 °C was used to determine the oxygen content of the cokes. Surface oxides and bulk oxide might be identified provided that they are desorbed at different temperatures. Oxides corresponding to possible metal oxides can also be identified by looking at the high temperature range and compare with graphite [5]. It should be noted that the heating rate is very high compared to conventional temperature programmed desorption methods (TPD) typically used to distinguished CO and CO_2 desorption from surfaces [6].

3.1.2 X-ray Absorption Spectroscopy

A powerful tool to do investigations on material properties is to use synchrotron radiation. By accelerating electrons at high energies one can obtain continuous spectra much more intense than using regular X-ray methods, and it is easy to tune the experiments and achieve high resolution results. X-ray Absorption Spectroscopy (XAS) can be used on samples in gas phase, liquids and solids [7-9].

The XAS measurements are done by sending X-rays to hit the sample with enough energy to eject an electron from an atom. Specific elements in the sample can be targeted by choosing the correct energy/wavelength, and a photoelectron from a specific electronic shell will be emitted. Three detection methods are possible. X-ray absorption is most common, where the absorption is extracted directly by measuring the intensity of incoming and transmitted X-ray beam [7, 10], but the two methods used in this study is X-ray fluorescence and electron yield (Figure 3.1). Fluorescence mode is good for highly diluted samples; "self-absorption" must be considered for concentrated samples [10, 11]. Electron yield mode avoids

this effect because of the short mean free path for the electrons, resulting in a surface sensitive method [7, 10].
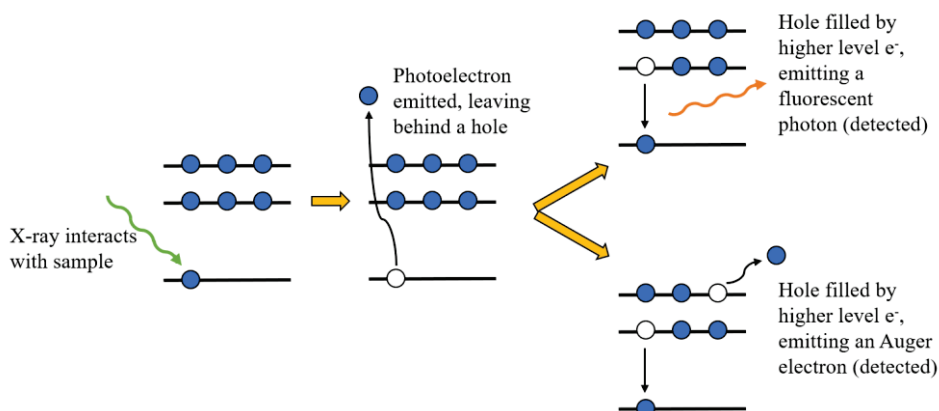
Figure 3.1: The XAS analysis methods considered in this study. Detection of fluorescent photon (upper) or Auger electron (lower).

When measuring over a selected incident X-ray energy range, the onset of photoelectron emission leads to a very rapid increase in the detected signal and resulting spectrum. This is called the edge and is usually followed by several peaks at energies close to the edge, and oscillations for a longer range after [9]. This is presented in Figure 3.2, where the main regions used for characterisation are marked: X-ray absorption near-edge structure (XANES) and extended X-ray absorption fine structure (EXAFS) respectively. The edge is named by which core electrons are excited; the *K*-edge corresponds to emission of 1s electrons, *L*-edge of 2s and 2p electrons, and so forth.
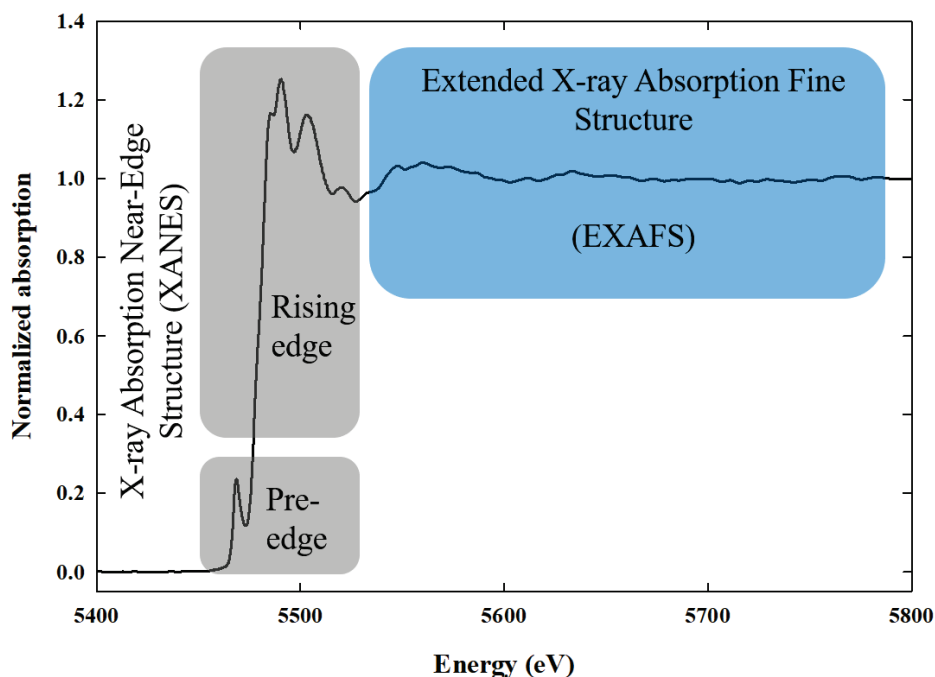
Figure 3.2: Example of XAS spectra. Adapted from [12] with permission.

The two regions are analysed separately. The XANES region, mainly the pre-edge feature, the edge position, and the peaks in the 30-50 eV range after the edge, is used to find information on oxidation state, geometry and band structure. This is accomplished by fingerprinting, *i.e.* by comparing the unknown XANES spectra with spectra for known compounds. Some quantitative information can also be extracted from mixed samples by fitting the reference compounds by linear combination fitting (LCF). The oscillations in the EXAFS region is a result of scattering of the photoelectron by the neighbouring atoms, and the signal is for this reason highly dependent on both its own wavelength and distance to the scattering atoms. The EXAFS region can therefore be used in combination with knowledge on known structures, and the nearest atoms as well as space group and crystal system can be identified (local structure). Large databases for crystallographic data exists for EXAFS analysis, like the crystallographic open database (COD) [13]. EXAFS does not require long-range order [7-10].

In this work, cokes were investigated for sulfur speciation using *K*-edge XANES at the Canadian Light Source (CLS) in Saskatoon, Saskatchewan, Canada.

Although shape and peak positions relative to the edge should always be the same, it is important to run the reference samples at the same time, with the same settings, as the unknown samples (in our case the coke samples), to be able to use the fingerprinting and LCF techniques to analyse the data. Several organic and inorganic sulfur reference compounds were run at the same time for comparison. This synchrotron measured both fluorescence and Auger electrons simultaneously, but only the electron yield was used due to non-diluted reference samples. The cokes were also investigated for Ni, V and Fe speciation using the *K*-edge (both XANES and EXAFS regions were analysed) at the Australian Synchrotron in Clayton, Victoria, Australia. Several references were run at the same time. This beamline used fluorescence mode only, and the references were diluted to avoid self-absorption.

3.2 Anode Characterisation

3.2.1 Anodes Routine Measurements

Pilot scale anodes were produced in-house by Hydro Aluminium [14]. The aggregate size was 0-2 mm, where the small size was chosen to ensure a homogenous surface to be investigated at small scale laboratory experiments. Some routine measurements were performed on anodes with an aggregate size of 0-6 mm, as denoted below. This is assumed not to have affected the results.

The pilot anodes were characterised using International Organization for Standardization (ISO) methods or similar by Hydro. All the mentioned tests are routine measurements done by Hydro Aluminium.

- Density (ISO-12985-1:2000), specific electrical resistivity (SER) (ISO 11713:2000) and permeability (in-house Hydro method similar to ISO 15906:2007) was measured for *all anodes*.
- *A single anode with 0-6 mm particles* were analysed by X-ray fluorescence (XRF) (ISO 12980:2000) to determine the levels of sulfur (and metal) impurities, and analysed for coefficient of thermal expansion (similar to ISO 14420:2005).
- CO_2 and air reactivity were measured on test pieces of *three 0-6 mm anodes* using in-house thermogravimetric analysis methods developed by Hydro, similar to ISO 12988-1 and ISO 12989-1 respectively.

3.2.2 Surface Characterisation

The surface of several anodes was investigated with a confocal microscope from Alicona. The microscope scans the entire surface as a grid, with a vertical

resolution of 100 nm. The vertical scan height corresponds to all pits and topography being in focus, and the software automatically finds the focus for all parts of each image, and combines all images to display a 3D map of the surface. The software reports the ratio between true and projected area (TA/PA), which is defined as the surface roughness of the sample. Depending on the depth of surface pores, these can be displayed as voids as no focus can be found within the chosen vertical scan height (or it is simply "too dark").

3.2.3 Electrochemical Measurements

All electrochemical experiments used the same closed furnace set up, in an argon atmosphere at 1000 °C. An aluminium reference electrode produced in-house (details on the reference can be found in the Appendix in the thesis of Sommerseth [15]) to measure the potential between anode test electrode and the reference; the graphite crucible acted as the counter electrode. Three different anode assemblies were used. A sketch of each of these, and the position in the bath, is presented in Figure 3.3. Because of the small variation in the reference electrode between runs, as well as possible variations in the electrolyte through one experimental run, graphite electrodes were regularly included in the sequence of electrolysed samples for comparison.

(a)   **(b)**   **(c)**
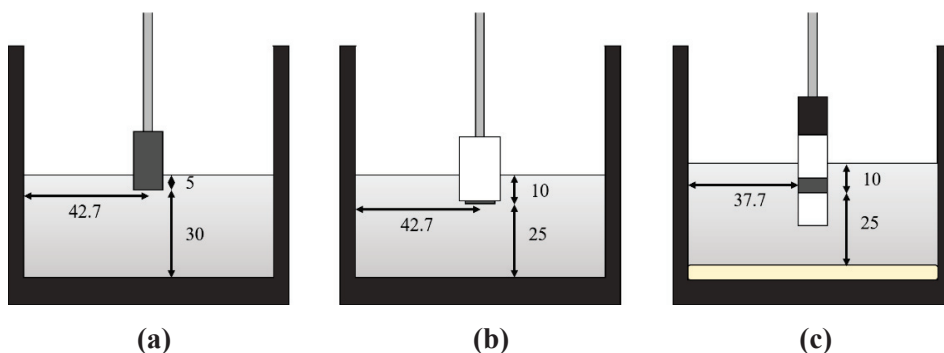
Figure 3.3: The positions of the different anode assemblies. **(a)** Unshielded anode, **(b)** horizontal anode [16, 17] and **(c)** vertical anode assembly (including a shield in the bottom) [5, 18, 19]. The numbers are in mm.

Electrochemical techniques include chronopotentiometry, chronoamperometry, cyclic voltammetry (CV) and electrochemical impedance spectroscopy (EIS)

References

[1]   S. Rørvik, M. Aanvik, M. Sørlie and H.A. Øye. Characterization of Optical Texture in Cokes by Image Analysis. *Light Metals* (2000), pp. 549-554.

[2]   E.W. Washburn. Note on a Method of Determining the Distribution of Pore Sizes in a Porous Material. *Proc. Natl. Acad. Sci. U. S. A.* (1921), **7**(4), pp. 115-116.

[3]   M. Thommes, K. Kaneko, A. V. Neimark, J. Olivier, F. Rodriguez-Reinoso, J. Rouquerol and K. Sing. Physisorption of gases, with special reference to the evaluation of surface area and pore size distribution (IUPAC Technical Report). *Pure Appl. Chem.* (2015), **87**(9-10), pp. 1051-1069.

[4]   E.P. Barrett, L.G. Joyner and P.P. Halenda. The Determination of Pore Volume and Area Distributions in Porous Substances. I. Computations from Nitrogen Isotherms. *J. Am. Chem. Soc.* (1951), **73**(1), pp. 373-380.

[5]   R.J. Thorne, C. Sommerseth, A.M. Svensson, A.P. Ratvik, S. Rørvik, E. Sandnes, L.P. Lossius and H. Linga. Correlation between Coke Type, Microstructure and Anodic Reaction Overpotential in Aluminium Electrolysis. *J. Electrochem. Soc.* (2015), **162**(12), pp. E296-E307.

[6]   J.L. Figueiredo, M.F.R. Pereira, M.M.A. Freitas and J.J.M. Órfão. Modification of the surface chemistry of activated carbons. *Carbon* (1999), **37**(9), pp. 1379-1389.

[7]   G. Bunker. *Introduction to XAFS: A Practical Guide to X-ray Absorption Fine Structure Spectroscopy.* Cambridge University Press: Cambridge, 2010.

[8]   S. Calvin. *XAFS for Everyone.* CRC Press: Florida, 2013.

[9]   D.C. Koningsberger and R. Prins. *X-ray absorption: principles, applications, techniques of EXAFS, SEXAFS, and XANES.* John Wiley and Sons: New York, 1988.

[10]   S. Kelly, D. Hesterberg, B. Ravel, A. Ulery and L. Richard Drees. Analysis of Soils and Minerals Using X-ray Absorption Spectroscopy, in: *Methods of Soil Analysis—Part 5: Mineralogical Methods.* Soil Science Society of America Book Series No. 5, Madison, 2008.

[11]   C.H. Booth and F. Bridges. Improved Self-Absorption Correction for Fluorescence Measurements of Extended X-Ray Absorption Fine-Structure. *Phys. Scr.* (2005), pp. 202.

[12]   G. Jahrsengene, H.C. Wells, C. Sommerseth, A.P. Ratvik, L.P. Lossius, R.G. Haverkamp and A.M. Svensson. Vanadium Speciation in Petroleum Cokes for Anodes used in Aluminium Electrolysis. *TRAVAUX - Proceedings for the ICSOBA Conference* (2017), **46**, pp. 617-624.

[13]   S. Gražulis, D. Chateigner, R.T. Downs, A.F.T. Yokochi, M. Quirós, L. Lutterotti, E. Manakova, J. Butkus, P. Moeck and A. Le Bail. Crystallography Open Database - an open-access collection of crystal structures. *J. Appl. Crystallogr.* (2009), **42**(4), pp. 726-729.

[14]   L.P. Lossius, J. Chmelar, I. Holden, H. Linga and M. Tkac. Pilot Scale Anodes for Raw Material Evaluation and Process Improvement. *Light Metals* (2016), pp. 1177-1182.

[15]   C. Sommerseth. *The Effect of Production Parameters on the Performance of Carbon Anodes for Aluminium Production.* PhD thesis. Norwegian University of Science and Technology, 2016.

[16]   R.J. Thorne, C. Sommerseth, A.M. Svensson, A.P. Ratvik, S. Rørvik, E. Sandnes, L.P. Lossius and H. Linga. Bubble Evolution and Anode Surface Properties in Aluminium Electrolysis. *J. Electrochem. Soc.* (2015), **162**(8), pp. E104-E114.

[17]   W. Gebarowski, A.P. Ratvik, S. Rørvik, L.P. Lossius, H. Linga and A.M. Svensson. Effect of Coke Properties on the Bubble Formation at the Anodes During Aluminium Electrolysis in Laboratory Scale. *Light Metals* (2017), pp. 1203-1211.

[18]   W. Gebarowski, C. Sommerseth, A.P. Ratvik, E. Sandnes, L.P. Lossius, H. Linga and A.M. Svensson. Interfacial Boundary between Carbon Anodes and Molten Salt Electrolyte. *Light Metals* (2016), pp. 883-888.

[19]   R.J. Thorne, C. Sommerseth, A.M. Svensson, E. Sandnes, L.P. Lossius, H. Linga and A.P. Ratvik. Understanding Anode Overpotential. *Light Metals* (2014), pp. 1213-1217.

Chapter 4 A XANES Study of Sulfur Speciation and Reactivity in Cokes for Anodes used in Aluminum Production

Gøril Jahrsengene[1], Hannah C. Wells[2], Stein Rørvik[3], Arne Petter Ratvik[3], Richard G. Haverkamp[2], Ann Mari Svensson[1]

[1]NTNU Norwegian University of Science and Technology, Trondheim, Norway
[2]Massey University, Palmerston North, New Zealand
[3]SINTEF Industry, Trondheim, Norway

Abstract

Availability of anode raw materials in the growing aluminum industry results in a wider range of petroleum cokes being used to produce carbon anodes. The boundary between anode grade cokes and what previously was considered non-anode grades are no longer as distinct as before, leading to introduction of cokes with higher sulfur and higher trace metal impurity content in anode manufacturing. In this work, the chemical nature of sulfur in five industrial cokes, ranging from 1.42 to 5.54 wt% S, was investigated with *K*-edge XANES, while the reactivity of manufactured anodes towards CO_2 was measured by thermogravimetric analysis. XANES identified most of the sulfur as organic sulfur compounds. In addition, a significant amount is identified (16-53 %) as S-S bonded sulfur. A strong inverse correlation is observed between CO_2-reactivity and S-S bound sulfur in the cokes, indicating that the reduction in reactivity is more dependent on the amount of this type of sulfur compound rather than the total amount of sulfur or the amount of organic sulfur.

4.1 Introduction

High-quality carbon anodes are critical to the economy of aluminum production. Anode carbon, which is consumed during electrolysis, makes up around 11 to 13 % of the cost of aluminum production [1]. Anodes are produced by mixing calcined petroleum coke, recycled anode butts and coal tar pitch before being subject to a baking cycle up to 1200 °C. Smelters require anodes with high-density, low-impurity levels (*e.g.* V, Ni, Fe, Si, Na, Ca, Mg and Al) and low thermal expansion to achieve predictable performance in the cells, usually achieved by blending different cokes. Sulfur is usually specified around 1.5 to 2 wt% based on operational experience, and in some cases restricted due to limitations on SO_2 to the atmosphere for smelters without SO_2 scrubbing.

The availability of high-quality anode grade calcined petroleum cokes for use in anodes is declining, resulting in challenges for the aluminum industry. One reason for the reduction in coke quality is that sour crude oils, with high sulfur and other impurity content and higher specific gravity, are now favored by many refineries because they are more available and of lower cost than the lightweight, low sulfur, sweet oils [2]. Petroleum coke is produced from the heavy residual fractions of crude oil, the fraction that tends to be highly concentrated in impurities (including sulfur), and with improved techniques for extracting the volatile fractions the quality of the coke decreases. This results in cokes with higher sulfur content, usually accompanied by an increase in metal trace impurities. An almost linear relationship between sulfur and vanadium content is observed in most cokes [3], although the relationships tend to be more scattered for cokes very high in vanadium or sulfur. Vanadium promote carbon reactivity with air, resulting in an increase in anode consumption if the anode cover material is not completely sealing the top and sides of the anode [4].

It is important to understand that there is not a shortage of coke, it is only the availability of good anode-grade cokes that are not covering the demand of the aluminum industry. Hence, the smelters have to learn to cope with this gradual decline in availability of high-quality raw materials. Because of the limited availability of high-quality cokes, the use of shot coke, previously described as fuel grade, has been investigated as one alternative [2, 5].

Sulfur is present in cokes in a variety of forms. In crude oil, more than 1500 sulfur compounds have been identified [6]. During calcination of green coke and baking of the anode, thermal processes may change the chemical form of sulfur. Sulfur can be present as a part of the carbon lattice, attached to side chains, between

aromatic sheets, on the surface of clustered molecules or on surfaces and pores bound by capillary condensation, adsorption, or chemisorption [7].

XANES (X-ray absorption near-edge structure) spectroscopy is a powerful technique when analyzing sulfur chemistry in solids. It has been used to investigate organic and inorganic sulfur bonding in coals [8, 9], various petroleum and petroleum source rocks oil [10], materials for electrodes in batteries [11], as well as in different earth materials and sediments [12-14]. In a selection of industrial anode cokes and baked anodes, XANES revealed the sulfur speciation to be organic sulfur rings, primarily as thiophene-containing polycyclic aromatic hydrocarbons [15]. Thiophenes have also been detected in cokes by a combination of X-ray photoelectron spectroscopy (XPS), Fourier-transform infrared spectroscopy (FTIR), and simulations [16]. How these sulfur-containing hydrocarbons transform during electrolysis, mainly by producing COS and SO_2 gases, has also been investigated [15, 17].

For non-electrochemical (secondary) reactions such as air burn, CO_2 burn, and carbon dusting, cell temperature, anode manufacturing parameters, and raw material properties (coke and pitch) are important. Specific metal impurities in the coke, *e.g.*, vanadium, are known to catalyze reactions between carbon and oxygen, and carbon and produced CO_2, increasing the carbon consumption [18]. The reaction between carbon and air is not believed to be significantly affected by sulfur [19], and the increase usually observed with higher sulfur cokes is believed to be caused by the parallel increase in metal catalyst content, while sulfur is believed to have a positive effect on the reaction between carbon and produced CO_2 [20-24]. Sulfur may have a negative effect on the total carbon consumption due to electrochemically produced COS [25]. Increasing sulfur while holding metal content constant revealed an increase for both air and CO_2 reactivity [26]. The actual effect should be investigated in combination with metal impurities, as it is believed that the decrease in CO_2 reactivity may be due to the formation of inactive metal-sulfur complexes during carbonization [27]. Sulfur also depress the catalytic effect of sodium, which enters the anodes through butts, perhaps as a Na-S-O complex [28]. Most investigations have, however, been done through doping, for example, for vanadium, nickel, iron, and sulfur [29, 30], and does not necessarily reflect the actual coke conditions if the impurities are not in the same chemical state or form as in the industrially produced coke.

In this study, the CO_2 reactivity and sulfur speciation of industrial cokes with varying levels of sulfur, metallic impurities, and isotropy, are measured. By choosing industrial cokes with varied composition, rather than chemically doped

cokes, a realistic assessment of chemical speciation and the relationships between composition and reactivity is sought.

4.2 Experimental Section

4.2.1 Coke

Five calcined petroleum cokes (designated A-E) originating from different crude oils produced by different industrial manufacturers were selected from a larger group of cokes based on vanadium and sulfur content. The cokes are calcined at 1200 to 1250 °E, where °E is an equivalent temperature representing the baking level, a method frequently used by the industry [31]. This method is based on assessment of changes in crystallinity, *i.e.*, L_c, of a calibrated reference coke sample inserted in the furnace.

4.2.2 Elemental Analysis and CO₂ Reactivity

Coke impurities were determined by X-ray fluorescence (XRF) according to ISO 12980:2000 on the bulk coke materials (single source coke), from which the contents of both metallic impurities and sulfur were identified. The CO_2 reactivity was determined using a standard mass loss test (RDC Equipment) for coke CO_2 reactivity according to ISO-12981-1 Standard RDC-1141, where the mass loss of 5 g coke with grain size 1 to 1.4 mm is determined after being exposed to a CO_2 gas flow rate of 50 l/h for 100 minutes at 1000 °C.

4.2.3 Isotropy
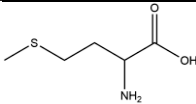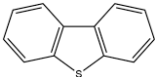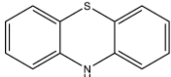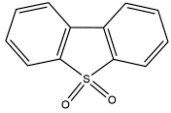
Optical texture was characterized by studying epoxy-mounted and polished coke samples under polarized light using a Leica/Reichert MeF3A metallurgical optical reflected light microscope. For each coke, 144 grains of ~0.75 mm size were captured at ×250 optical magnification. A macro running within NIH Image Software was employed to determine the fiber and mosaic indexes of the cokes [32]. The degree of isotropy is determined by the mosaic index, a parameter describing the fineness of the optical domains, while the degree of anisotropy is determined by the fiber index which describes the degree of alignment of the optical domains.

4.2.4 XANES

Sulfur *K*-edge XANES was performed at the Canadian Light Source (CLS) in Saskatoon, Canada on the soft X-ray microcharacterization beamline (SXRMB) 06B1-1. This provides a resolution ($\Delta E/E$) of 1×104 and a flux of around 1×1011 photons·s^{-1}. Coke and reference samples were analyzed as ground

powder. The reference compounds were chosen based on previous work [15] to represent a range of aromatic organic sulfur compounds containing different functional groups that could approximate the functionalized amorphous and graphitic carbon of the cokes, and inorganic compounds that represent a range of oxidation states of sulfur associated with known impurity elements in cokes (Table 4.1). XAS was recorded from 2452 eV to 2532 eV with a step size of 2 eV pre-edge, 0.10 eV over the edge region, and 0.75 eV post edge, all with a dwell time of 1 second. Spectra were collected in both fluorescence yield mode (FLY) and total electron yield mode (TEY). Three scans of each sample were collected and afterwards combined.

Table 4.1: Reference compounds used in S K-edge XANES.

Name	Composition/Structure
Inorganic S	
Elemental sulfur/graphite	25%S
Sodium sulfate	Na_2SO_4
Sodium metabisulfite	$Na_2S_2O_5$
Sodium sulfite	Na_2SO_3
Potassium sulfate	K_2SO_4
Potassium thiosulfate	$K_2S_2O_3$
Potassium thiocyanate	KSCN
Iron(II)sulfide	FeS
Organic S	
L-methionine	$CH_3SCH_2CH_2CH(NH_2)CO_2H$
Dibenzothiophene	$C_{12}H_8S$
Phenothiazine	$C_{12}H_9NS$
Dibenzothiophene sulfone	$C_{12}H_8O_2S$

The S XANES spectra of the cokes were fitted using Athena software [33] with linear combinations of normalized $\mu(E)$ spectra of reference compounds with E_0 constrained for each component to the fitted value for that component (LCF). Athena uses non-linear least squares minimization for fitting. A 50 eV energy range was used for the fit (20 eV below E_0 to 30 eV above E_0). Initially a combinatorial fit was performed using a wide range of standards, then this was refined to promising candidates for the final fit. Linear combination fits were also tested with derivative $\mu(E)$ and $\chi(k)$ and these gave very similar best fit combinations. The accuracy of this technique depends on a sensible selection of standards, based on some knowledge of the possible chemistry, and the extent of the differences between the spectra of the standards used. In the compounds investigated here, the standards had spectra of substantially different shapes and this increases the confidence of the validity of the fit.

4.3 Results

4.3.1 Elemental Composition

The composition of the cokes as measured by XRF varied in sulfur content in the range 1.42 to 5.54 wt%, and vanadium between 116 and 714 ppm (Table 4.2). The relationship between sulfur and vanadium concentration in the cokes is shown in Figure 4.1a.

Table 4.2: Composition of the five cokes measured by XRF.

	S (wt.%)	V (ppm)	M (ppm)
Coke A	1.42	116	761
Coke B	3.56	402	1323
Coke C	5.54	432	1356
Coke D	3.82	714	1668
Coke E	4.42	624	2009

M includes Na, Mg, Al, Si, Ca, V, Fe and Ni.

4.3.2 Isotropy

The four cokes A-D have similar mosaic and fiber indices and all are categorized as anisotropic (Figure 4.1b). Coke A is the most anisotropic of these. Coke E has a higher mosaic index and a lower fiber index than the other cokes indicating a more isotropic coke. In each of the cokes A-D, there was a relatively large

variation in isotropy among the 144 grains investigated for each coke. This is reflected in the relatively high standard deviations of the mosaic and fiber indices. A typical anisotropic structure identified within cokes A-D is shown in Figure 4.2a. In Figure 4.2b, a typical highly isotropic structure identified in all the grains of coke E is shown. In comparison, relatively few isotropic grains were identified in cokes A-D. The high standard deviations observed in the anisotropic cokes are due to the heterogeneous nature of coke as a material; by experience these cokes are similar to other commercially available cokes.
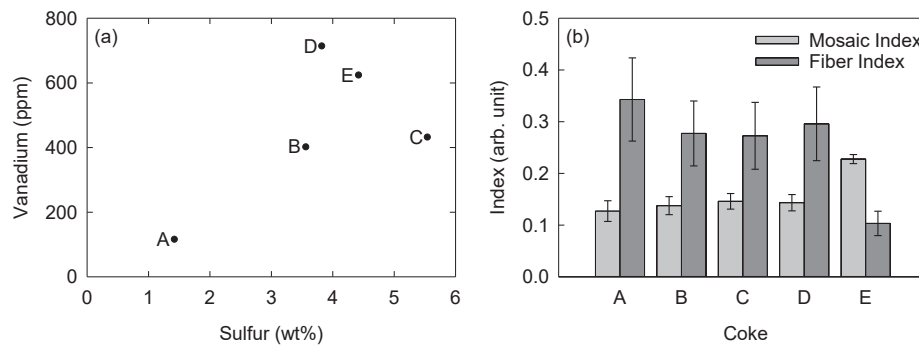
Figure 4.1: (a) Level of vanadium *vs* level of sulfur for cokes A-E; **(b)** Mosaic and fiber index for cokes A-E.
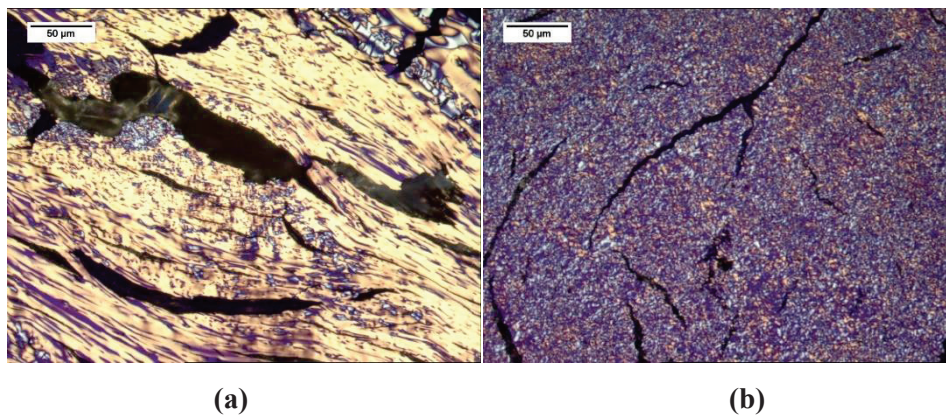
Figure 4.2: Optical microscopy images of coke grains under polarized light. **(a)** Anisotropic structure of coke A; **(b)** isotropic structure of coke E.

4.3.3 XANES

Although both TEY and FLY sulfur K-edge spectra were recorded, self-absorption was a problem at the edge in many of the FLY spectra so only TEY spectra have been used in the analysis. Figure 4.3a and Figure 4.4 show the resulting S XANES spectra for the reference compounds. The vertical line is the position of the main peak in the coke spectrum, presented in Figure 4.3b. All the reference standards and the cokes were stable under the X-ray beam with the exception of dibenzothiophene which displayed significant changes to the spectra after each scan. Therefore, multiple scans were merged for all samples and standards except for dibenzothiophene. It was noted that phenothiazine gave a purple fluorescence under X-ray irradiation.
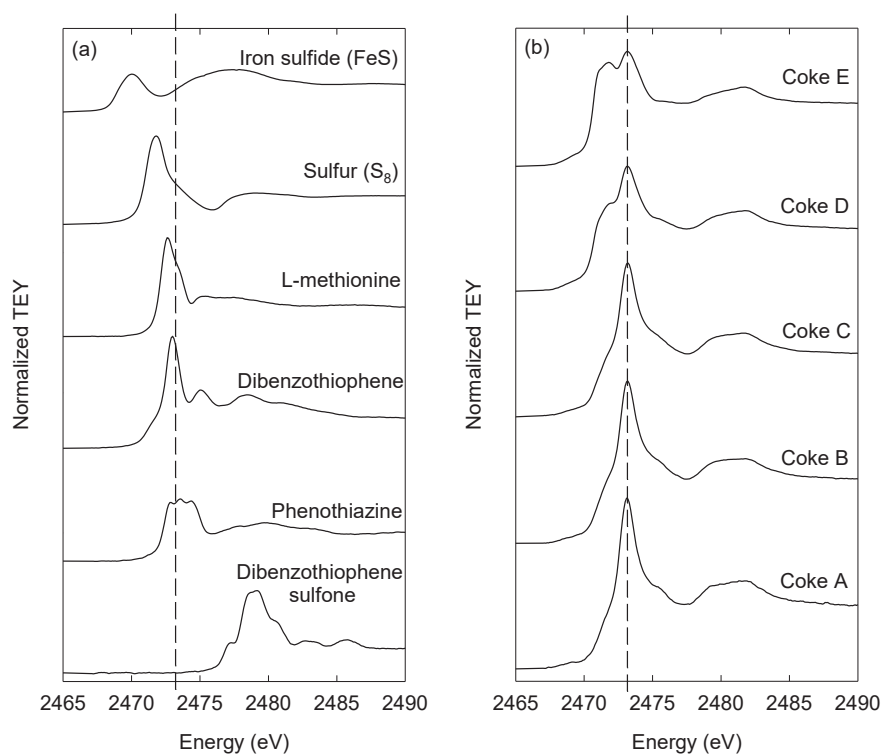
Figure 4.3: Normalized (to step edge = 1) sulfur K-edge XANES for the **(a)** reference organic standards, sulfur (S_8) and iron(II)sulfide; **(b)** industrial cokes A-E. The vertical lines in both figures mark the main peak position in the coke spectra.
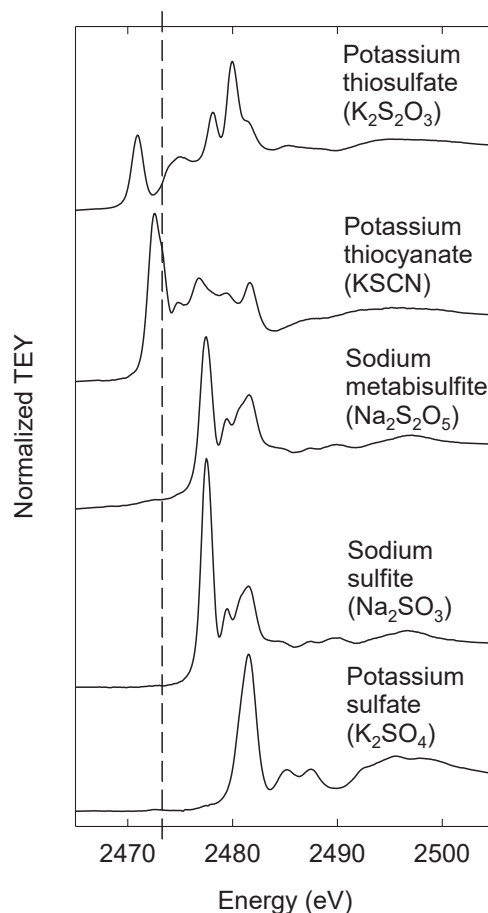
Figure 4.4: Normalized (to step edge = 1) sulfur *K*-edge XANES for potassium thiosulfate, potassium thiocyanate, sodium metabisulfite, sodium sulfite and potassium sulfate. The sodium sulfite and potassium sulfate are shrunk to 70 % compared to the remaining spectra. The vertical line marks the main peak position in the coke spectra (Figure 4.3b).

Some major differences were evident in the S *K*-edge XANES spectra of the cokes (Figure 4.3b). Cokes A, B, and C are very similar to each other. A slight broadening to the left of the main peak is observed in these cokes, and a small contribution of a sulfur species with a lower energy edge is evident. Coke D has a low-energy shoulder to the left of the main peak, evolving to a visible peak in

coke E, indicating a much higher contribution of an additional sulfur compound with a low-energy peak in these two cokes than the other three.

An identification of the main components of the coke spectra was achieved by linear combination fitting (LCF) with the reference spectra. A good fit was obtained for cokes A-C using two aromatic sulfur compounds, phenothiazine and dibenzothiophene, with a contribution of S_8 (Figure 4.5a). The main edge for S_8 is at lower energy than for most of the other standards (of higher nominal oxidation state) which provides some certainty in the fitting of this component to the cokes. Other options for this component are considered in the discussion. In cokes D and E, it is apparent that this low-energy component is present in a higher proportion, and the LCF fitting supports this by eliminating the main organic specie by using coke C as a component in the LCF (Figure 4.5b). The portion of identified S_8 ranges from 16 % of the S in coke A to 53 % of the S of coke E (Table 4.3).
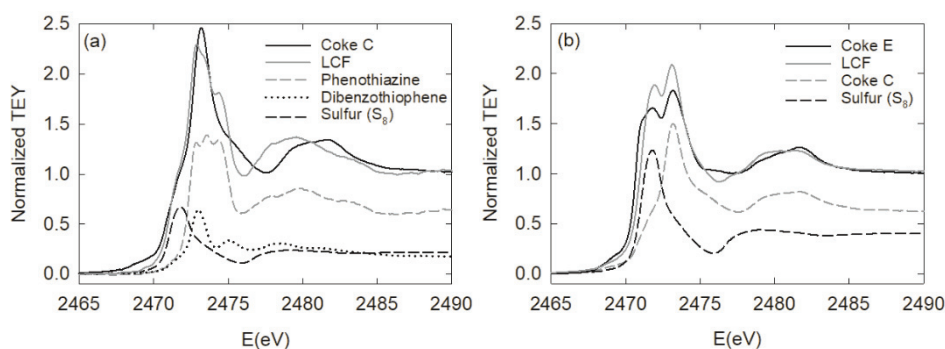
Figure 4.5: *K*-edge XANES spectra of **(a)** coke C fitted with two organic references and sulfur (S_8); **(b)** coke E fitted with coke C and sulfur (S_8).

Table 4.3: Relative amounts of sulfur contained in different compounds estimated from the linear combination fitting (LCF) of the five cokes.

	Phenothiazine	Dibenzothiophene	Sulfur
Coke A	0.604	0.235	0.161
Coke B	0.596	0.203	0.201
Coke C	0.628	0.161	0.212
Coke D	0.535	0.060	0.405
Coke E	0.444	0.027	0.529

The fits corresponding to Table 4.3 are presented in Figure 4.6 for cokes A, B, D and E. The edge position is best for cokes A and B, which are very similar to coke C in Figure 4.5a, while the additional edge present in coke D and E gives a poorer edge position for the LCF.
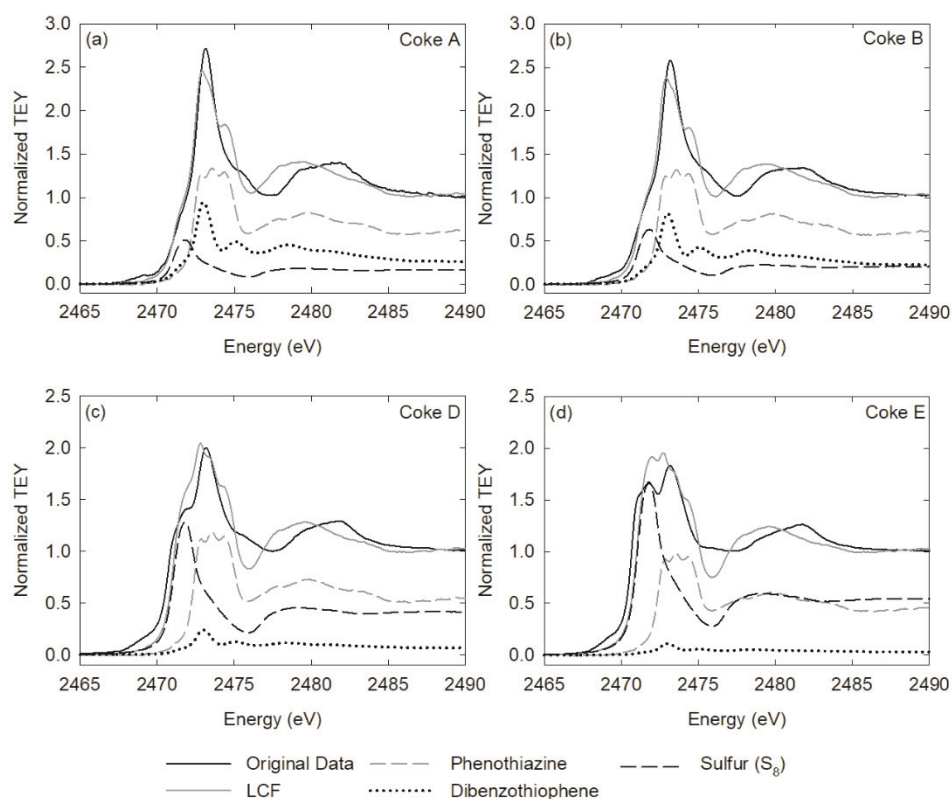
Figure 4.6: Sulfur *K*-edge XANES spectra of the cokes fitted with two organic references and sulfur (S_8) of coke **(a)** A; **(b)** B; **(c)** D; **(d)** E. Note that the y-scales are different.

4.3.4 CO_2 Reactivity and Sulfur

The relationship between CO_2 reactivity and total sulfur content is given in Figure 4.7a, showing an overall trend that low-sulfur cokes are more reactive than high-sulfur cokes, while among the high-sulfur cokes there is no direct relationship between reactivity and total sulfur content. Evaluating only the organic sulfur in Figure 4.7b, cokes D and E have very low reactivity and low organic sulfur content, indicating something other than this type of sulfur is lowering the

reactivity. A stronger relationship is observed, however, when the CO_2 reactivity is plotted against the amount of sulfur identified as S_8 by LCF present in the cokes (Figure 4.7c). Last, the CO_2 reactivity *vs* ratio of sulfur/metal in Figure 4.7d indicates a difference between cokes D and E from the remaining cokes due to its very low reactivity compared to the ratio.
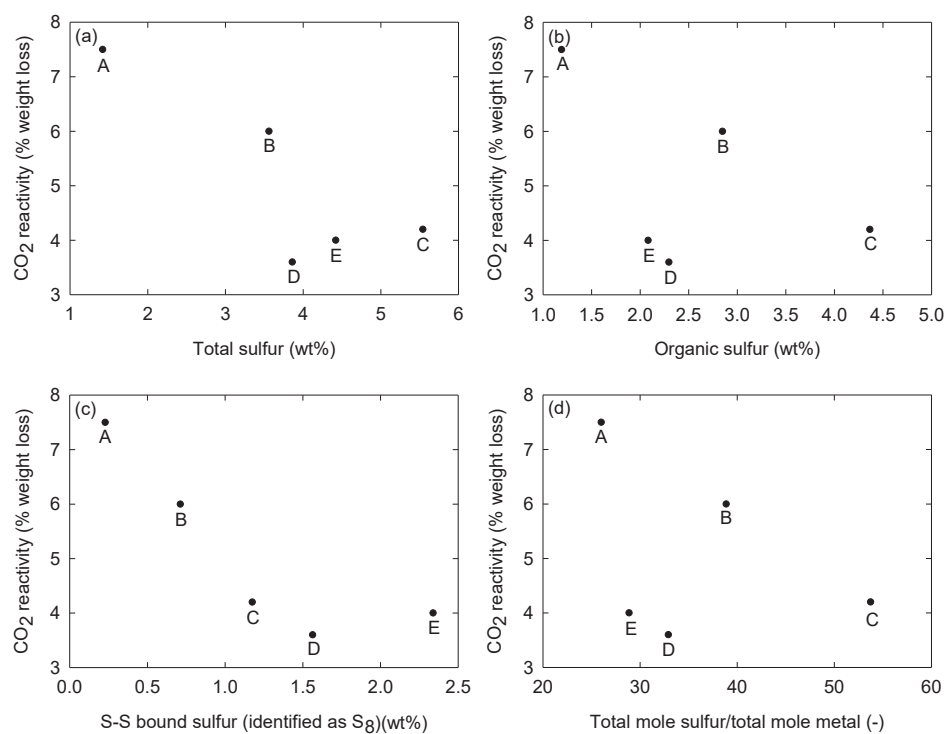
Figure 4.7: The CO_2 reactivity of the cokes *vs* **(a)** total sulfur content; **(b)** organic sulfur content; **(c)** S-S bound sulfur content (identified as S_8); **(d)** sulfur/metal ratio.

4.4 Discussion

The XANES analysis of the cokes has shown that sulfur is present as both organic sulfur and, apparently, as sulfur not bound in the aromatic structure (S_8). The LCFs in Figure 4.5 and Figure 4.6 indicate that the low-energy peak of S_8 is causing the left shoulder in the coke spectra. However, this is not the only option; not included in this study is pyritic sulfur (oxidation state -1, MeS_2 where Me indicates a metal) [15] and disulfides (oxidation state 0, R-S-S-R bonding) [34, 35] which both have the K-edge peak in the same area as S_8. These low-energy peaks are known to be caused by S-S bonding, and other compounds with S-S bonding all exhibit this feature (*e.g.*, observed for potassium thiosulfate in Figure 4.4). Compounds with S-S bonding are therefore difficult to distinguish from each other using K-edge fingerprinting, and sulfur identified as S_8 will be referred to as S-S bound sulfur.

The presence of S-S bound sulfur was not observed in large quantities in a previous XANES study of cokes [15, 36], but has previously been suggested based on XPS measurements [16]. The proportions of S-S bound sulfur (identified from S_8 in the LCF) vary between the different cokes from 16 to 53 % of the total S giving 0.3 to 2.3 wt% of this kind of sulfur in the cokes. The exact kind of compound is unknown, but large amounts of sulfides with sulfur in the oxidation state -1 (*e.g.*, FeS_2) are unlikely due to the much higher quantity of sulfur *vs* metals (Figure 4.7d). Metal sulfides with a lower oxidation number of -2 (*e.g.*, FeS) are not observed. If all metal impurities in coke E (2009 ppm, 0.06 mole%) is bound as MeS_2, only 0.12 mole% of the total 1.7 mole% S would be bound this way. This is only 7 % of the total sulfur in the coke, and much less than the S_8 fitted contribution of 53 %, indicating that the contribution from metal sulfides can only be small. In addition, considering that this would be made up of several different metal sulfides, each with their own XANES spectrum, this is below the fitting capabilities in these samples. The detection limit for any particular component varies, and depends in particular on how different the spectrum of that component is to the other components present. In order to understand the contribution of the metal impurities to the sulfur speciation, the best method would be to measure XANES at the X-ray absorption edge for each metal.

The organic sulfur is present in complex aromatic compounds with the sulfur in a nominal oxidation state of 0. Combined with the observations concerning S-S bound sulfur, the results presented here indicate that sulfur is present in the cokes in a fairly uniform oxidation state of 0, perhaps approaching a redox equilibrium during calcination. The XANES analysis for coke A, B, and C match very well with previous investigations on cokes [15, 36], but the high amount of observed

S-S bound sulfur (identified from S_8) as seen in cokes D and E has not been observed previously.

Sulfur in coke is usually described as organic aromatic compounds, but this may be based mostly on feedstock properties rather than a direct analysis of the coke. The XANES results give a possibility of presence of S_8 in the coke, but the mechanism for the formation of this specie in the cokes is not well understood. A possibility is that S_8, or S_x ($x = 2, 4, 6$), is formed during high-temperature calcination in closed pores, which then is unable to leave the structure and is condensed after cooling to room temperature. Some possibilities for the mechanism at high temperature of the organic sulfur transformation to S_x have been proposed [17, 26], but have not been verified experimentally (although significant amounts of sulfur were detected with SEM and EDS analysis in pores). The LCFs (Table 4.3, Figure 4.5 and Figure 4.6) give good fits to the edge for cokes A-C using S_8 as a component, while the small displacement of the edge in cokes D and E can be explained by an unidentified S species with a small displacement compared to S_8. This can be caused by the presence of condensed S_x, or other forms of S-S bonding (*e.g.*, to carbon disulfides as C-S-S-C bonding and a small contribution of MeS_2).

The five cokes are from different producers, using crude oils with different composition, but all contain sulfur as a mixture of organic aromatic sulfur and S-S bound sulfur. The varying production and calcination processes therefore lead to similar sulfur chemistries. The results from the linear combination fit (Table 4.3, Figure 4.5 and Figure 4.6) support previous work showing that thiophene-containing polycyclic aromatic hydrocarbons are the most stable after heat treatment [16]. These may also contain some thiazines. Limited information can be obtained on the organic sulfur standards using the *K*-edge. For this differentiation between organic S species, the *L*-edge may be a better choice.

The organic compounds that were selected as standards are approximations for the chemical states that may be found within the cokes: sulfur contained in five and six member ring compounds with different levels of electron acceptor or donor strengths. However, it is not expected that the exact complex structure of S within the aromatic framework in cokes will be fully represented using pure reference compounds. The LCF indicates a larger portion of thiazines than anticipated, however, comparing the peak position and shape of the coke spectra in Figure 4.3b with the thiophene standard in Figure 4.3a it looks like a better correlation. More organic compounds were investigated in a previous study [34] showing the diversity of the spectrum. It is difficult to confirm or deny if any one

of these is the correct organic compound in this study. For the low-energy S-S components, the only possibilities are the carbon disulfides (R-S-S-R). The precision regarding the division of S-S bonding and aromatic sulfur bonding achieved in this study seems to be very good.

The decreasing CO_2 reactivity with increasing S-S bound sulfur content for the five cokes observed in Figure 4.7c suggests that this kind of sulfur is involved in inhibiting the reaction of CO_2 with the coke. The much poorer relationship between CO_2 reactivity and organic S (Figure 4.7b) suggests that the organic sulfur does not play a large role in this inhibition. The effect of decreasing reactivity with increasing sulfur content is best understood in relation to the metal catalysts, which seems to be de-activated or passivated by the sulfur. As shown in Figure 4.7d, the relationship between CO_2 reactivity, sulfur, and catalytic metals is complex. Cokes D and E have a higher total S content but lower sulfur/metal ratio than coke B caused by the high content of metals, as well as significantly lower CO_2 reactivity. This indicates that the sulfur in cokes D and E is more efficiently de-activating the metals than in coke B. A possibility is that condensed solid sulfur is present at pore walls, and that the pressure in the pores in combination with the high temperature results in the film being intact and hinders the accessibility of metal catalysts. The exact mechanism for the inhibition was outside the scope of this study, but the S-S bound sulfur (identified from S_8) is the effective component and results in conditions in coke that hinder reactivity with CO_2. Provided that simpler methods can be developed for the identification of S-S bound sulfur, the results demonstrate the potential for significant reduction of the carbon consumption for the industry.

There are other considerations than CO_2 reactivity in selecting suitable coke blends for anode production. These include coke structure, total metal impurity content, specific metal impurity content, homogeneity, density, and porosity. As an example, using coke E in a mix with *e.g.*, coke A to reduce the CO_2 reactivity will lead to a high metal impurity content in the anode. This is undesirable because several of the metals will end up in the produced aluminum metal. The structure of coke E is also undesirable in anode blends because it may give a higher probability of the anode cracking due to a higher thermal expansion coefficient of isotropic cokes compared to anisotropic cokes. When comparing cokes B and D, with similar sulfur content and anisotropy, coke D might be preferred in industrial applications due to the much lower reactivity, at least if the vanadium level is low enough. Coke D may also be preferable to coke C, as the higher sulfur content does not give any decrease in the reactivity.

4.5 Conclusions

Industrial cokes varying with respect to levels of sulfur, metallic impurities, and isotropy were characterized by S K-edge XANES. Sulfur was found to be present as S-S bound sulfur, contrary to expectations, and complex organic (polycyclic thiophene and thiazines) compounds. The CO_2 reactivity of the cokes showed a strong correlation between S-S bound sulfur content and CO_2 reactivity, showing that the presence of these sulfur species, rather than the total amount of sulfur, reduces the CO_2 reactivity. Identification of the components of sulfur that are important for reduction of reactivity is valuable for the optimization of coke blends for anodes for aluminum production, and will contribute to improved anode performance and a strategy to minimize SO_2 emissions, as well as CO_2 emissions.

Acknowledgements

References

[1]   G. Djukanovic. Analysis of production costs in the aluminium smelting industry. *Aluminium Journal* (2012), pp.

[2]   L. Edwards, N. Backhouse, H. Darmstadt and M.-J. Dion. Evolution of Anode Grade Coke Quality. *Light Metals* (2012), pp. 1204-1212.

[3]   L. Edwards. The History and Future Challenges of Calcined Petroleum Coke Production and Use in Aluminum Smelting. *JOM* (2015), **67**(2), pp. 308-321.

[4]   A. Gomez and R. Heilgendorff. Carbon Plant Performance with Blended Coke. *Light Metals* (2005), pp. 535-538.

[5]   L. Edwards, F. Vogt, M. Robinette, R. Love, A. Ross, M. McClung, R.J. Roush and W. Morgan. Use of Shot Coke as an Anode Raw Material. *Light Metals* (2009), pp. 985-990.

[6]   J.M. Hunt. *Petroleum geochemistry and geology.* 2nd ed. W. H. Freeman: New York, 1996.

[7]   T. Reis. To coke, desulfurize and calcine, Part 2: Coke quality and its control. *Hydrocarbon Process.* (1975), **54**(6), pp. 97-104.

[8]   M. Kasrai, J.R. Brown, G.M. Bancroft, Z. Yin and K.H. Tan. Sulphur characterization in coal from X-ray absorption near edge spectroscopy. *Int. J. Coal Geol.* (1996), **32**(1), pp. 107-135.

[9]   M. Wang, L. Liu, J. Wang, L. Chang, H. Wang and Y. Hu. Sulfur K-edge XANES study of sulfur transformation during pyrolysis of four coals with different ranks. *Fuel Process. Technol.* (2015), **131**, pp. 262-269.

[10]   G.S. Waldo, R.M.K. Carlson, J.M. Moldowan, K.E. Peters and J.E. Penner-hahn. Sulfur speciation in heavy petroleums: Information from X-ray absorption near-edge structure. *Geochimica et Cosmochimica Acta* (1991), **55**(3), pp. 801-814.

[11]   S. Britto, M. Leskes, X. Hua, C.-A. Hébert, H.S. Shin, S. Clarke, O. Borkiewicz, K.W. Chapman, R. Seshadri, J. Cho and C.P. Grey. Multiple Redox Modes in the Reversible Lithiation of High-Capacity, Peierls-Distorted Vanadium Sulfide. *J. Am. Chem. Soc.* (2015), **137**(26), pp. 8499.

[12]   M.E. Fleet. XANES spectroscopy of sulfur in Earth materials. *Can. Mineral.* (2005), **43**, pp. 1811-1838.

[13]   I.J. Pickering, R.C. Prince, T. Divers and G.N. George. Sulfur K-edge X-ray absorption spectroscopy for determining the chemical speciation of sulfur in biological systems. *FEBS Lett.* (1998), **441**(1), pp. 11-14.

[14]   D. Solomon, J. Lehmann and C.E. Martínez. Sulfur K-edge XANES Spectroscopy as a Tool for Understanding Sulfur Dynamics in Soil Organic Matter. *Soil Sci. Soc. Am. J.* (2003), **67**(6), pp. 1721-1731.

[15] S.J. Hay, J. Metson and M.M. Hyland. Sulfur Speciation in Aluminum Smelting Anodes. *Ind. Eng. Chem. Res.* (2004), **43**(7), pp. 1690-1700.

[16] J. Xiao, Q. Zhong, F. Li, J. Huang, Y. Zhang and B. Wang. Modeling the Change of Green Coke to Calcined Coke using Qingdao High-Sulfur Petroleum Coke. *Energy Fuels* (2015), **29**(5), pp. 3345-3352.

[17] Q. Zhong, J. Xiao, H. Du and Z. Yao. Thiophenic Sulfur Transformation in a Carbon Anode during the Aluminum Electrolysis Process. *Energy Fuels* (2017), **31**(4), pp. 4539-4547.

[18] G.J. Houston and H.A. Øye. Consumption of anode carbon during aluminium electrolysis. I-III. *Aluminium* (1985), **61**, pp. 251-254, 346-349, 426,428.

[19] M. Sørlie. Effect of Sulphur on Anode Reactivity and Rlectrolytic Consumption. *Light Metals* (1994), pp. 659−665.

[20] G.P. Gilmore and V.L. Bullough. A Study on the Effecs of Anode Coke Sulfur Content on the Operation of Side Pin Søderberg Cells. *Light Metals* (1982), pp. 741-752.

[21] P.J. Rhedey. Carbon Reactivity and Aluminum Reduction Cell Anodes. *Light Metals* (1982), pp. 713-725.

[22] S.S. Jones and R.D. Hildebrandt. Influence of High-Sulfur Cokes on Anode Performance. *Light Metals* (1979), pp. 553-574.

[23] K.N. Tran, S.K. Bhatia, A.J. Berkovich and A. Tomsett. Influence of Sulfur and Metal Microconstituents on the Reactivity of Carbon Anodes. *Energy Fuels* (2009), **23**(4), pp. 1909-1924.

[24] E.H. Hardin and C.L. Beilharz. Correlations of laboratory and commercially calcined petroleum cokes. *Light Metals* (1991), pp. 565-574.

[25] S. Pietrzyk and J. Thonstad. Influence of the Sulphur Content in the Carbon Anodes in Aluminium Electrolysis – a Laboratory Study. *Light Metals* (2012), pp. 657-664.

[26] J. Xiao, S.-y. Deng, Q.-f. Zhong and S.-l. Ye. Effect of sulfur impurity on coke reactivity and its mechanism. *Trans. Nonferrous. Met. Soc. China* (2014), **24**(11), pp. 3702-3709.

[27] Y.D. Bensah and T. Foosnaes. The Nature and Effect of Sulphur Compounds on CO_2 and Air Reactivity of Petrol Coke. *ARPN J. Eng. Appl. Sci.* (2010), **5**(6), pp. 35-43.

[28] S.M. Hume, W.K. Fischer, R.C. Perruchoud, J.B. Metson and J.B. Baker. Influence of Petroleum Coke Sulphur Content on the Sodium Sensitivity of Carbon Anodes. *Light Metals* (1993), pp. 535-541.

[29] T. Eidet and J. Thonstad. Effects of Sulphur, Nickel and Vanadium on the Air and CO_2 Reactivity of Cokes. *Light Metals* (1997), pp. 436-437.

[30] T. Eidet, J. Thonstad and M. Sørlie. Effects of Iron and Sulphur on the Air and CO_2 Reactivity of Cokes. *Light Metals* (1997), pp. 511-517.

[31]   L.P. Lossius, I. Holden and H. Linga. The Equivalent Temperature Method for Measuring the Baking Level of Anodes. *Light Metals* (2006), pp. 609-613.

[32]   S. Rørvik, M. Aanvik, M. Sørlie and H.A. Øye. Characterization of Optical Texture in Cokes by Image Analysis. *Light Metals* (2000), pp. 549-554.

[33]   B. Ravel and M. Newville. Athena, Artemis, Hephaestus: Data Analysis for X-ray Absorption Spectroscopy using IFEFFIT. *J. Synchrotron Rad.* (2005), **12**(4), pp. 537-541.

[34]   G.N. George and M.L. Gorbaty. Sulfur K-edge X-ray absorption spectroscopy of petroleum asphaltenes and model compounds. *J. Am. Chem. Soc.* (1989), **111**(9), pp. 3182-3186.

[35]   G. Sarret, J. Connan, M. Kasrai, G.M. Bancroft, A. Charrié-Duhaut, S. Lemoine, P. Adam, P. Albrecht and L. Eybert-Bérard. Chemical forms of sulfur in geological and archeological asphaltenes from Middle East, France, and Spain determined by sulfur K- and L-edge X-ray absorption near-edge structure spectroscopy. *Geochim. Cosmochim. Acta* (1999), **63**(22), pp. 3767-3779.

[36]   S.J. Hay. *The Formation and Fate of Carbonyl Sulfude (COS) Gas in Aluminium Smelting.* PhD thesis. The University of Auckland, 2002.

Chapter 5 Reactivity of Coke in Relation to Sulfur Level and Microstructure

Gøril Jahrsengene[1], Stein Rørvik[2], Arne Petter Ratvik[2], Lorentz Petter Lossius[3], Richard G. Haverkamp[4], Ann Mari Svensson[1]

[1]Department of Materials Science and Engineering, NTNU Norwegian University of Science and Technology, Trondheim, Norway
[2]SINTEF Industry, Trondheim, Norway
[3]Hydro Aluminium AS, Primary Metal Technology, Årdal, Norway
[4]School of Engineering and Advanced Technology, Massey University, Palmerston North, New Zealand

Abstract

The quality of coke materials available for anodes for the aluminium industry is changing and industrial cokes with higher impurity levels are now introduced. The cokes in the anodes must meet specifications with respect to impurity levels to ensure proper operation in the electrolysis cells, and a desired quality of the aluminium metal. The presence of sulfur has been observed to reduce the CO_2 reactivity and a certain level of sulfur is therefore targeted in the anodes. In this work, the significance of varying sulfur and metal impurity content in industrial cokes were evaluated with respect to CO_2 reactivity, accessible surface area, pore size distribution, surface oxide groups and crystallite reactive edge planes. While relatively similar cokes are observed to give a lower reactivity with increasing sulfur content, cokes that have distinct differences in surface properties can have dissimilar reactivity despite identical sulfur content. Correlations between pore size distribution and presence of S-S bound sulfur, possibly condensed S_x, was also observed.

5.1 Introduction

In electrolytic production of aluminium, carbon is oxidized to CO_2 during the reduction of alumina (Al_2O_3). Prebaked anodes made of calcined petroleum coke, coal tar pitch and recycled anode butts provide the carbon for the reaction. The theoretical amount of carbon is 0.33 kg to produce 1 kg of Al, while in practice it is higher. This is caused by the back reaction, where produced Al is oxidized by CO_2 forming Al_2O_3 and CO. The anode may also react with CO_2 or air. The air reactivity can be reduced by limiting the exposure to air by good covering of the anodes, which is well incorporated in modern cells. The reaction between produced CO_2 and carbon is assumed to be reduced by the presence of sulfur in the anodes.

In addition to the less dense coke materials produced by the refining industry, the cokes also have an increasing amount of sulfur and other metal impurities compared to previously used cokes [1, 2]. The changes in the quality of the petroleum coke will affect the performance of the anode in the pot room. An anode with more open porosity will be more susceptible to air and CO_2 reactivity, and many of the metals catalyse these reactions. A good overview of the effect of impurities can be found elsewhere [3]. Beside the possible increase in reactivity due to metals present in the coke, most metals end up in the finished aluminium product. Thus, the metal specifications for vanadium, nickel, iron and silicon in the anodes is usually decided by the tolerance level of these in the primary aluminium rather than the increase in carbon oxidation. Sulfur is believed to have a positive effect on the carboxy reactivity, as high sulfur anodes has been shown to have a lower reactivity. The inhibiting effect caused by more sulfur comes at the expense of more SO_2 produced, and for plants without SO_2 scrubbing the sulfur content may be limited by SO_2 emission permission.

Sulfur and its effect on reactivity has been subject to many investigations, and it is assumed that the positive effect sulfur has on the CO_2 reactivity comes in combination with the metal impurities, as the effect of sulfur alone is possibly negative for both air and CO_2 reactivity when evaluating sulfur without other impurity interference [4]. The observed positive effect may be caused by the formation of inactive metal-sulfur complexes during carbonization [5, 6], however, most of the conclusions are based on adding impurity elements during the production of anodes. This will not necessary represent industrially produced anodes, as doped anodes may not have the same chemical state properly incorporated within the coke structure, which may give misleading results compared to the industrial cokes.

Sulfur speciation of selected cokes was previously performed by the authors by the X-ray absorption near-edge structure (XANES) technique [7]. Five cokes were investigated, which varied significantly with respect to content of sulfur (1.4 to 5.5 wt%) and content of metal impurities. Furthermore, there was a poor correlation between the sulfur content and CO_2 reactivity of some of these cokes. The ratio between S-S bound sulfur (which can result from elemental sulfur, pyritic sulfur and R-S-S-R sulfur) and other aromatically bound sulfur (*e.g.* thiophenes) varied significantly. The amount of S-S bound sulfur was found to inversely correlate with the CO_2 reactivity.

The aim of this work has been to gain an improved understanding of a wider range of factors that might affect the CO_2 reactivity of the cokes, like variations in reactive surface area of cokes of similar particle size, as well as variations in surface structure (*i.e.* ratio of edge to basal planes) or surface chemistry. Reactive surface area was estimated based on Hg intrusion porosimetry and N_2 adsorption experiments. The latter was also used for analysis of surface structure (ratio of edge, basal and defect sites). Possible differences in surface chemistry were also studied by monitoring the release of CO_2 and CO during heating.

5.2 Materials and Method

Previously reported data and properties [7] of the five industrial cokes are summarized in Table 5.1. Impurity content (sulfur and metals) was measured by X-Ray Fluorescence (XRF), the optical texture evaluated by mosaic and fiber index found by light microscopy, and CO_2 reactivity reported as mass loss during a standard mass loss test (ISO-12981-1 Standard RDC-1141). The S-S bound sulfur found by XANES is reported as fraction of total sulfur content and wt%.

Table 5.1: Composition of the five cokes. "Total metals" include V, Fe, Ni, Na, Mg, Al, Si and Ca.

	Sulfur (wt%)	S-S bound sulfur (fraction/wt%)	CO_2 reactivity (% mass loss)	Total metals (ppm)	Optical structure
Coke A	1.42	0.16 / 0.23	7.5	761	Anisotropic
Coke B	3.56	0.20 / 0.71	6.0	1323	Anisotropic
Coke C	5.54	0.21 / 1.18	4.2	1356	Anisotropic
Coke D	3.86	0.41 / 1.56	3.6	1668	Anisotropic
Coke E	4.42	0.53 / 2.34	4.0	2009	Isotropic

The same cokes were investigated for varying surface properties. An evaluation of the pore size distributions was done by two parallels of Hg intrusion porosimetry using AutoPore IV 9520 (from Micromeritics) on 1-2 mm coke particles (ASTM D4404-10). Hg is forced into pores where the force/pressure used will be equivalent to a pore size, the intrusion volume is measured and the Washburn equation is used to generate volume and size distributions (cylindrical pores are assumed) [8].

Nitrogen adsorption at -198.5 °C was performed on the full relative pressure range (up to $P/P_0 = 0.98$) on crushed coke particles < 25 μm from the 1-2 mm fraction using a 3Flex 3500 Chemisorption Analyser (Micromeritics). Graphite powder (SLP30 from IMERYS) was used as a reference. The samples were degassed at 300 °C for 10 hours before analysis. The Barret-Joyner-Halenda (BJH) pore size distribution and area [9] were extracted from the software of the instrument. The adsorption data was used to find the relative contribution of edge:basal:defect sites based on a model established by Olivier [10] using density functional theory (DFT). Different adsorption potentials, expressed in kelvin (K), are used to account for the heterogeneity of the surface. For graphitic materials it is assumed that prismatic/edge sites are in the 20-49 K range, basal planes in the 50-60 K range, and the higher energy region of 61-100 K is used for defects [11]. Surface defects can be small, slit-like pores (< 1 nm diameter), surface steps as well as attributed to surface groups. Two or three parallels were done on freshly crushed samples.

Surface oxides, assumed to be attached to edge sites, will decompose to CO and CO_2 during heat treatment. A rapid temperature ramping program with an analyser (ONH386 Series) from LECO was used. The CO and CO_2 is first detected by separate IR cells, to see what gases goes off when (and indirectly at which temperatures), while the total oxygen is found after the gas pass through heated copper oxide to convert CO to CO_2 and then to a separate IR detector. By comparing to graphite, oxygen assumed to be related to metal impurities, can be excluded from the surface oxides. Samples of 0.1 g crushed coke particles (particle size < 25 μm) from the 1-2 mm fraction were packed in tin capsules and the measurements were done by ramping of power linearly in the temperature range from 500 to 3000 °C within 600 s. Two parallels of each coke and one from graphite powder were obtained.

The data obtained from Hg porosimetry, nitrogen adsorption and desorption and LECO oxygen analysis were combined and evaluated together with the previously obtained data presented in Table 5.1

5.3 Results and Discussion

5.3.1 Hg Intrusion Porosimetry

The (smoothed) pore size distribution in the cokes (1-2 mm fraction) found by Hg intrusion is presented in Figure 5.1. The measurements above 60 μm are excluded in the analysis of intrusion volume, surface area and average pore size in Table 5.2 as it is likely a result of intrusion between grains, while data below 0.1 μm is assumed affected by destruction of the grains at high pressures and is also excluded.
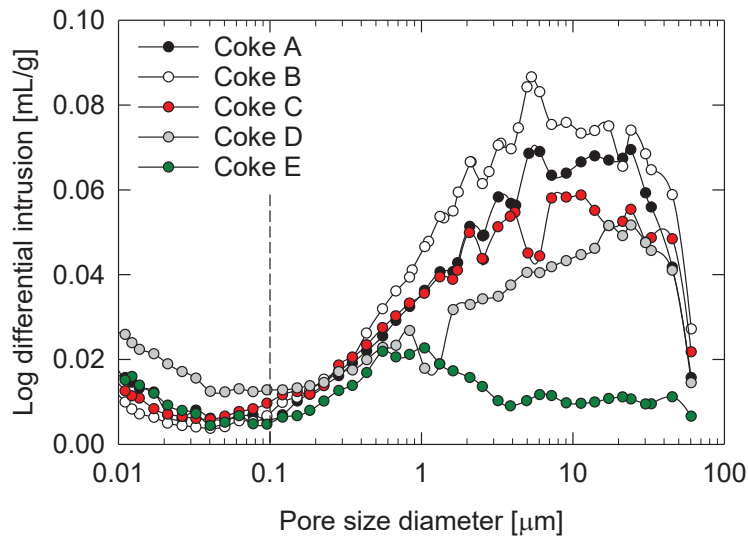
Figure 5.1: Pore size distribution as a function of intrusion volume.

There are significant differences between the cokes. Coke E has the lowest intrusion volume and a centre around 1 μm, resulting in a low total surface area. Coke D has a wider distribution and lower intrusion volumes than cokes A-C, resulting in low surface area compared to the other anisotropic cokes. Considering the region of pore diameters from 0.1 to 60 μm the average pore size is decreasing steadily from A to E (Table 5.2) while the total pore area is highest for coke B.

Table 5.2: The measured intrusion volume, estimated pore diameter and area for pores above 0.1 μm and below 60 μm, reference to Figure 5.1.

	Intrusion volume	Area	Average pore diameter (d=4V/A)
	(mL/g)	(m²/g)	(μm)
Coke A	0.1222	0.268	1.83
Coke B	0.1363	0.311	1.75
Coke C	0.1091	0.289	1.51
Coke D	0.0899	0.257	1.39
Coke E	0.0039	0.174	0.90

The high increase in measured intrusion volume at high pressures, observed to be increasing nearing 0.01 μm in Figure 5.1 (and in fact increasing a lot in the range not presented), can be assumed to be affected by failure of the coke microstructure; at 10 nm the pressure is equivalent to 1.4 tons/cm². The method is insufficient at these pressures because the result reflects the integrity of the grains rather than the porosity. To investigate micro- and mesoporosity in cokes, Hg intrusion porosimetry is clearly not the best option. This range needs to be evaluated further with other methods, for example pore size distributions obtained by N_2 adsorption.

5.3.2 Nitrogen Adsorption

Nitrogen adsorption and desorption isotherms are shown in Figure 5.2a for a selection of the cokes and the graphite. The isotherms resemble the type II isotherms defined by IUPAC [12], usually observed for non-porous and macroporous materials. The change to the linear middle section corresponds to the change from monolayer to multilayer adsorption, and the graphs increase without limit close to P/P_0=1. There is a small hysteresis observed and the sharp step-down of the desorption branch is observed approximately at P/P_0~0.4-0.5. This is defined as a H4 hysteresis loop, often observed for carbons with pore structures including several different pore sizes in the network (micro- mesoporous carbons). H4 can also be related to slit-shaped pores and microporosity. This behaviour is expected for petroleum cokes. All the cokes and the graphite have this hysteresis, but for coke E the relative difference between adsorption and desorption in the linear hysteresis area was larger than the other cokes. Cokes B and C had the smallest hysteresis.
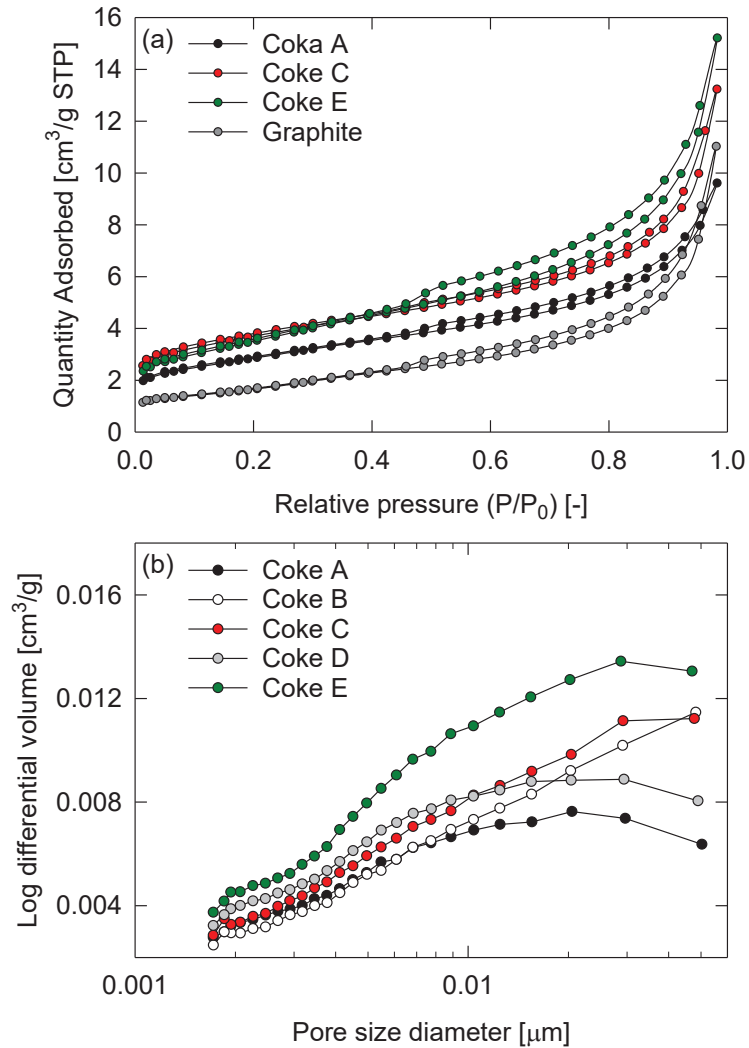
Figure 5.2: (a) Isotherms for cokes A, C, E and graphite, showing the quantity of N_2 adsorbed at varying relative pressures (P/P_0), **(b)** BJH pore size distribution.

The BJH adsorption pore size distribution in the mesopore area, with pore sizes between ~2 nm and 50 nm, is presented in Figure 5.2b. According to the results, coke A has the least amount of small pores, and coke E has more small pores than the other cokes. At the lowest pore size range, cokes A, B and C are quite similar, but variations are observed from ~4 nm. N_2 adsorption is a non-destructive method, and the behaviour of the cokes of pore sizes below 0.1 µm do not reflect

the observations from mercury intrusion, which was clearly affected by cracking of grains at high pressures. The isotropic coke has more pores in the entire range below 0.1 μm than the other cokes, as seen from Figure 5.2b, which confirm this theory. The BJH method use the Kelvin equation in combination with the t-curve (carbon black defined solid) and are known to under-estimate contribution from narrow mesopores, indicating that the method is not suited for determining specific differences for pore sizes below 5-10 nm.

The complete picture of the porosity of the cokes are still not established combining Hg porosimetry and N_2 adsorption. It is expected that the Hg porosimetry gives reliable data above 0.1 um, and significant differences between the cokes are observed, while the isotropic coke E has a significantly smaller average pore size than the rest of the cokes. N_2 adsorption also shows this coke has a larger contribution of pores down to 0.01 μm. A better analysis of the even smaller pores may be investigated using molecular simulations or DFT given a good model system supported by sufficient experimental data, but was beyond the scope of this study.

The surface coverage of edge, basal and defect area were determined by nitrogen adsorption combined with a DFT model in the software. A typical plot of the distribution of incremental surface area *vs* energy is presented for graphite in Figure 5.3a, where both the typical edge site energy (42 K) and basal plane energy (58 K) can be observed. The summarized result of the areas assumed to be edge, basal and defect sites for graphite and cokes are presented in Figure 5.3b. All cokes have a high portion of edge sites compared to graphite. For cokes A to C the portion of edge sites are increasing with increasing sulfur content (which increase from A to C), while cokes D and E have a significantly lower portion of edge sites. Both defect sites and edge planes indicate insufficiencies in the carbon material and less ordered structure. Coke D and E appear to have more of the non-reactive basal planes.
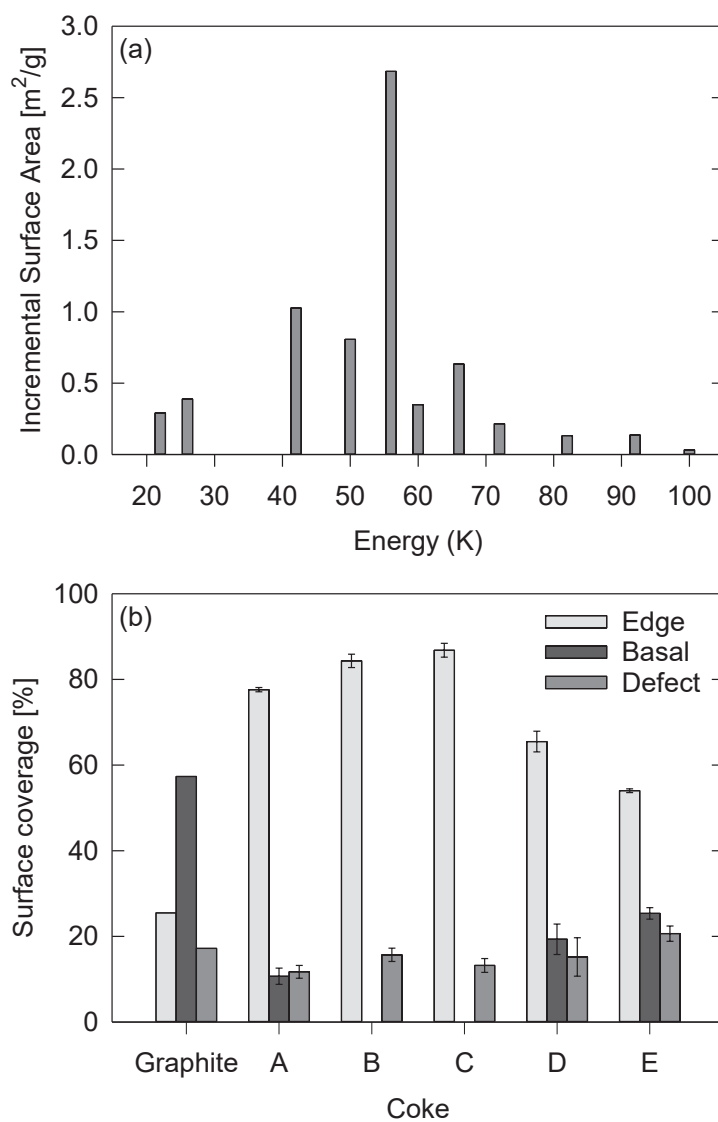
Figure 5.3: (a) Typical plot of incremental surface area *vs* energy for graphite, and **(b)** edge site, basal planes and defect sites surface coverage of graphite and industrial cokes A-E. Error bars for the cokes show one standard deviation where n=3 for cokes A-D and n=2 for coke E.

5.3.3 Surface and Metal Oxides

Information about the content of oxides in the cokes, obtained by combustion coke to CO and CO_2 measured by a LECO oxygen analyser, is presented in Figure 5.4 and Table 5.3. The total amount of oxygen varies from 0.128 wt% in coke A, to 1.07 wt% in coke C. Comparing release of CO_2 for graphite and cokes in Figure 5.4a it is clear that all but coke A have one or several additional peaks above 1450 °C. A similar limit is found in the release of CO in Figure 5.4b. By separately integrating the CO_2 and CO graphs, one can find the oxygen related to surface oxide groups assumed to be present below 1450 °C, and oxide related to metal oxides as the higher temperature peaks. Release of CO_2 from coke is an indication of carboxylic, anhydride and lactone groups, while phenol, carbonyl, anhydride, ether and quinone groups give rise to CO gas [13]. Below 1450 °C both CO_2 and CO peaks appear to be similar but with different intensities (the intensity do not reflect the actual amount of oxygen). Based on these results, no significant differences in the surface chemistry of the cokes could be detected, although the ramping of power (temperature) is far too high for detection of specific surface compounds. The technique is mostly used to find the total amount of oxygen in materials.

Table 5.3: The oxygen content in the cokes. The evaluation of surface oxides originates from data obtained below 1450 °C.

	Total oxygen	Oxygen as CO_2	Oxygen as CO	$CO:CO_2$ for surface
	(wt%)	(wt%)	(wt%)	groups
Graphite	0.132	0.057	0.075	1.1
Coke A	0.128	0.040	0.088	1.2
Coke B	0.578	0.060	0.518	5.1
Coke C	1.07	0.081	0.989	6.2
Coke D	0.652	0.053	0.599	5.3
Coke E	0.877	0.074	0.803	2.9
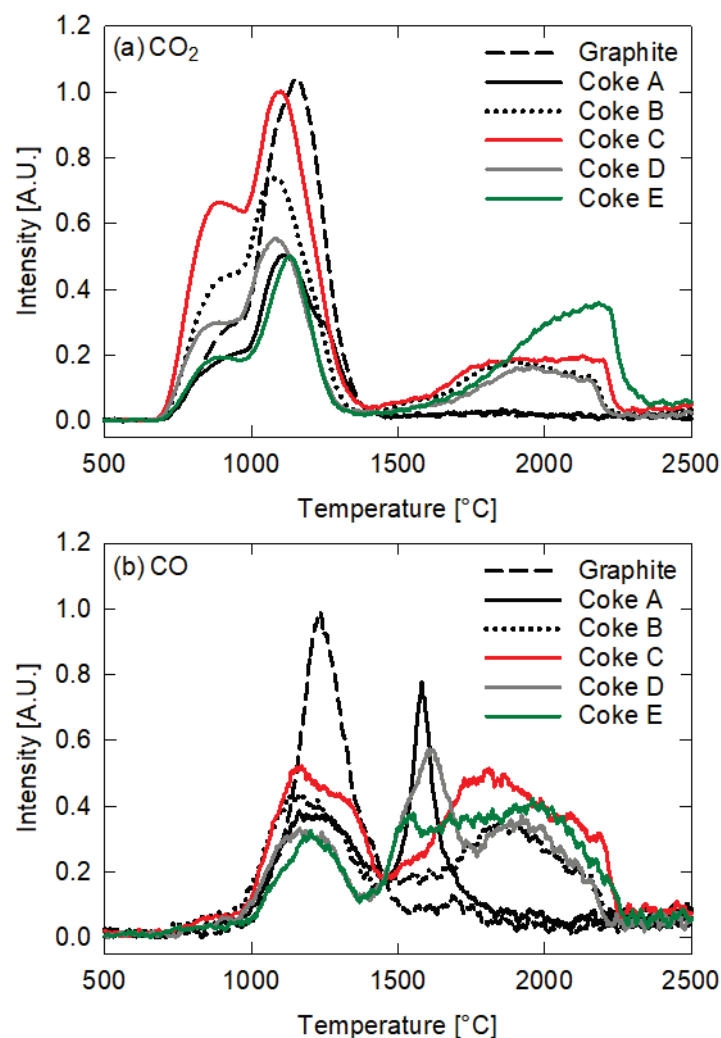
Figure 5.4: Evolved **(a)** CO_2 and **(b)** CO from combusted oxides in cokes and graphite.

Cokes B, C and D all have more than 5 times more CO than CO_2 and coke E has 3 times as much. This indicates that phenol, carbonyl, anhydride, ether and quinone surface groups are dominating in the cokes. From the $CO:CO_2$ ratio we observe that the cokes A and E, which also have relatively high reactivities when the active area is accounted for (see Figure 5.5), also have very low $CO:CO_2$ ratios, while the cokes B, C and D have similar $CO:CO_2$ ratios and also lower, and

relatively similar CO_2 reactivity. It is however, beyond the scope of this work to verify and gain a better understanding of these apparent correlations, and more experiments, preferably with a slower heating rate and a wider choice of cokes would be needed.

5.3.4 Evaluations of CO_2 Reactivity

The CO_2 reactivity will depend on the surface area accessible for the reaction between CO_2 and C, where diffusion of the CO_2 into the pores is of high importance. Although the small pores contribute to a larger surface area, transport of CO_2 gas is limited and the pore walls are thus not accessible for the reaction to a significant extent. In large pores, the mass transport can be described by the conventional binary diffusion coefficient, but when the pore size approach the mean free path of the CO_2 molecules, the slow Knudsen diffusion quickly starts to dominate [14]. The test was done at 1000 °C and 0.2 MPa, giving a mean free path (λ) of 365 nm for CO_2. Knudsen diffusion is said to be dominant when $K_n>10$ and negligible when $K_n<0.1$, where the so-called Knudsen number is defined as $K_n=\lambda/d_p$, where d_p is the pore diameter. This means that pores below approximately 40 nm does not contribute to the reactive area as the total diffusion here is very low. The total diffusion constant is a function of both the (constant) mass diffusion constant D_{ab}, approximately 1.1 cm^2/s for a CO_2-CO binary system at the given conditions using the Slattery-Bird correlation [15], and Knudsen diffusion constant D_K, proportional to d_p, by

$$\frac{1}{D_{tot}} = \frac{1}{D_{ab}} + \frac{1}{D_K} \tag{5.1}$$

Assuming pore diameters larger than 0.1 µm (*i.e.* corresponding to the region where we have reliable Hg intrusion data), D_{tot} decrease with more than 80 % compared to a situation where D_{ab} dominates (*i.e.* no or large pores). The calculated surface area, excluding pore sizes <0.1 µm, was used to normalize the CO_2 reactivity data in Figure 5.5, however, moving the included range to higher pore sizes do not result in a significant difference in the observed trends. All but coke E have a relatively similar pore size distribution above 0.1 um, and thus the reactivity of coke E is the only one that will change notably compared to cokes A to D. Figure 5.5 shows the reactivity with respect to total sulfur content, S-S bound sulfur and organic sulfur, and cokes A, D and E is also normalized to subtract the coverage of basal planes found by DFT evaluations (no basal planes were found for B and C).
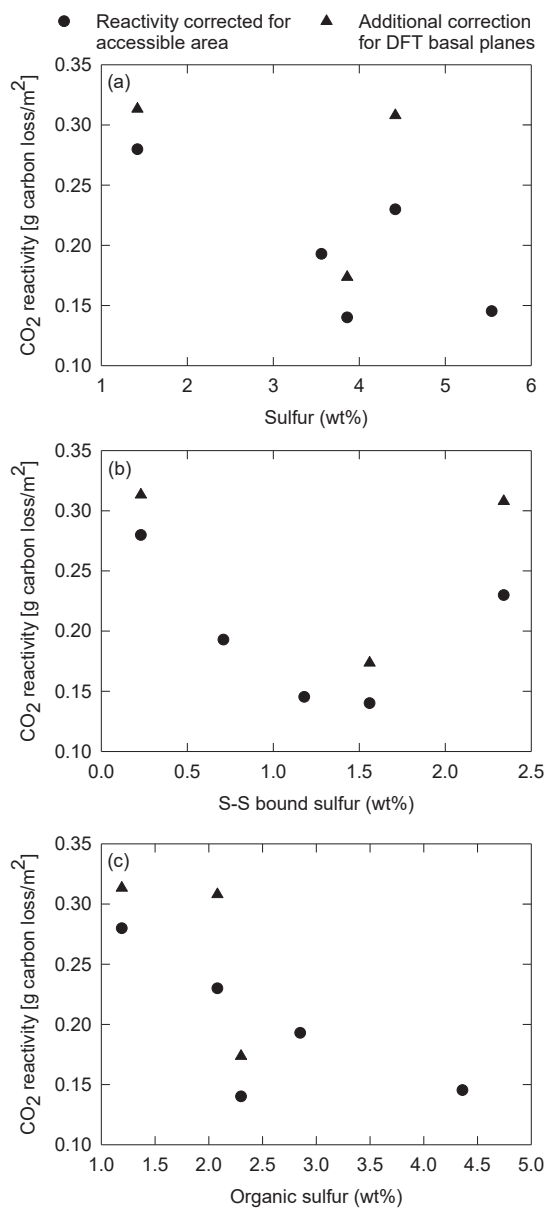
Figure 5.5: The normalized reactivity, with area corresponding to pore size > 0.1 μm and possible exclusion of basal planes, plotted with respect to **(a)** total sulfur, **(b)** S-S bound sulfur and **(c)** organic sulfur. Note that the y-value of each coke is identical in all figures, only the sulfur amounts vary (Table 5.1).

Based on Figure 5.5, the differences originally observed in mass loss during the reactivity test is likely due to differences in the available area for the reaction to occur. With the exception of coke E, decreasing reactivity with more sulfur, S-S bound sulfur and organic sulfur was observed. Comparing Figure 5.5a to Figure 5.5c, it appears that the correlation of lower reactivity and S-S bound sulfur previously observed may be indirect. Figure 5.6 show that the amount of S-S bound sulfur follow the area for pores < 50 nm (found by BJH adsorption data), which may also explain the presence of S-S bound sulfur, as many compounds containing S-S bonds (elemental sulfur for example), is not expected to be stable at the typical calcination temperatures. If S-S bound sulfur is present in the smaller pores, and these are not accessible for the CO_2 reaction, the S-S bound will not contribute to the inhibiting reaction. The proper chemistry of this S-S compound is still unknown, but S_x ($x = 2, 4, 6$ and 8), formed from organic sulfur in pores, trapped in small pores during heat treatment and subsequently condensed, have previously been discussed as an option [4].
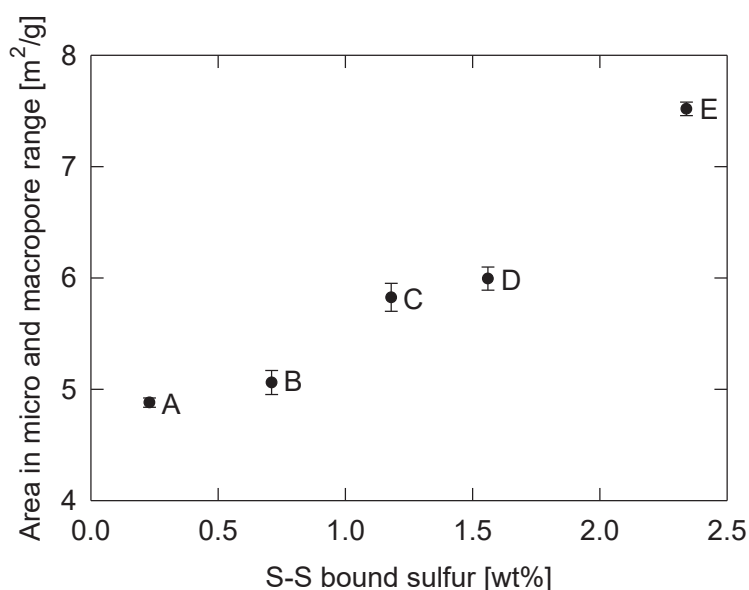
Figure 5.6: The relationship between area in the BJH evaluations (2-50 nm) and the S-S bound sulfur.

Regarding the cokes A, B and C, these cokes have similar surface areas and pore size distribution, the N_2 adsorption isotherms are similar and the DFT analysis gave almost complete surface coverage of reactive sites. The largest observed

difference was coke A on the BJH pore size distribution and the oxygen surface groups. The intermediate step of CO_{ads} formation in the Boudouard reaction may also be affected by the differences in the oxygen surface groups between the cokes, but these were observed to be similar in all cokes. Coke D and E were also shown to have a different pore size distribution explaining the low reactivity, as narrow pores are inaccessible for the reacting gases compared to the outer surface area/wide pores. A higher portion of the non-reactive basal planes was also observed in these cokes. The sulfur content, in practice the organic sulfur content, seems to be correlated to the lowering of reactivity in high-sulfur cokes, as S-S bound sulfur, possibly condensed S_x, is most likely trapped in narrow pores.

5.4 Conclusions

Selected cokes were investigated with respect to porosity, pore size distribution, surface chemistry and surface structure, and the investigations gave a better insight in different factors affecting CO_2 reactivity in cokes. Poor correlations between the reactivity and the amount of sulfur present in the cokes could be explained by the accessible surface area. The isotropic coke also has a much lower average pore size and a large amount of pores in the micro and macroporous range than the rest of the cokes, which can result in low structural integrity of the grains. Higher amount of S-S bound sulfur is observed in the cokes with smaller average pore size, indicating that any correlating relationship between S-S bound sulfur and CO_2 reactivity might be indirect.

Acknowledgements

References

[1]   L. Edwards. The History and Future Challenges of Calcined Petroleum Coke Production and Use in Aluminum Smelting. *JOM* (2015), **67**(2), pp. 308-321.

[2]   L. Edwards, N. Backhouse, H. Darmstadt and M.-J. Dion. Evolution of Anode Grade Coke Quality. *Light Metals* (2012), pp. 1204-1212.

[3]   G.J. Houston and H.A. Øye. Consumption of anode carbon during aluminium electrolysis. I-III. *Aluminium* (1985), **61**, pp. 251-254, 346-349, 426,428.

[4]   J. Xiao, S.-y. Deng, Q.-f. Zhong and S.-l. Ye. Effect of sulfur impurity on coke reactivity and its mechanism. *Trans. Nonferrous. Met. Soc. China* (2014), **24**(11), pp. 3702-3709.

[5]   Y.D. Bensah and T. Foosnaes. The Nature and Effect of Sulphur Compounds on CO_2 and Air Reactivity of Petrol Coke. *ARPN J. Eng. Appl. Sci.* (2010), **5**(6), pp. 35-43.

[6]   S.M. Hume, W.K. Fischer, R.C. Perruchoud, J.B. Metson and J.B. Baker. Influence of Petroleum Coke Sulphur Content on the Sodium Sensitivity of Carbon Anodes. *Light Metals* (1993), pp. 535-541.

[7]   G. Jahrsengene, H.C. Wells, S. Rørvik, A.P. Ratvik, R.G. Haverkamp and A.M. Svensson. A XANES Study of Sulfur Speciation and Reactivity in Cokes for Anodes Used in Aluminum Production. *Metall. Mater. Trans. B* (2018), **49**(3), pp. 1434-1443.

[8]   E.W. Washburn. Note on a Method of Determining the Distribution of Pore Sizes in a Porous Material. *Proc. Natl. Acad. Sci. U. S. A.* (1921), **7**(4), pp. 115-116.

[9]   E.P. Barrett, L.G. Joyner and P.P. Halenda. The Determination of Pore Volume and Area Distributions in Porous Substances. I. Computations from Nitrogen Isotherms. *J. Am. Chem. Soc.* (1951), **73**(1), pp. 373-380.

[10]   J.P. Olivier. The Surface Heterogeneity of Carbon and Its Assessment, in: *Adsorption by Carbons.* J. Tascón, E. Bottani (Eds.).   Elsevier, Amsterdam, 2008, pp. 147-166.

[11]   J.P. Olivier and M. Winter. Determination of the absolute and relative extents of basal plane surface area and "non-basal plane surface" area of graphites and their impact on anode performance in lithium ion batteries. *J. Power Sources* (2001), **97-98**, pp. 151-155.

[12]   M. Thommes, K. Kaneko, A. V. Neimark, J. Olivier, F. Rodriguez-Reinoso, J. Rouquerol and K. Sing. Physisorption of gases, with special reference to the evaluation of surface area and pore size distribution (IUPAC Technical Report). *Pure Appl. Chem.* (2015), **87**(9-10), pp. 1051-1069.

[13]   J.L. Figueiredo, M.F.R. Pereira, M.M.A. Freitas and J.J.M. Órfão. Modification of the surface chemistry of activated carbons. *Carbon* (1999), **37**(9), pp. 1379-1389.

[14]   Z. Tan. Basic Properties of Gases, in: *Air Pollution and Greenhouse Gases.* Springer, Singapore, 2014, pp. 27-58.

[15]   J.C. Slattery and R.B. Bird. Calculation of the diffusion coefficient of dilute gases and of the self-diffusion coefficient of dense gases. *AIChE Journal* (1958), **4**(2), pp. 137-142.

Errata

Corrected data for $CO:CO_2$ ratio for surface groups for cokes D and E are presented in Table 5.3 below. The changed result will contradict some of the statements in the paragraph following the original table. A suggested change in this paragraph is presented below.

Corrected Table 5.3: The oxygen content in the cokes. The evaluation of surface oxides originates from data obtained below 1450 °C.

	$CO:CO_2$ for surface groups *Original*	$CO:CO_2$ for surface groups *Corrected*
Graphite	1.1	1.1
Coke A	1.2	1.2
Coke B	5.1	5.1
Coke C	6.2	6.2
Coke D	*5.3*	*4.9*
Coke E	*2.9*	*6.6*

Original paragraph: Cokes B, C and D all have more than 5 times more CO than CO_2 and coke E has 3 times as much. This indicates that phenol, carbonyl, anhydride, ether and quinone surface groups are dominating in the cokes. From the $CO:CO_2$ ratio we observe that the cokes A and E, which also have relatively high reactivities when the active area is accounted for (see Figure 5.5), also have very low $CO:CO_2$ ratios, while the cokes B, C and D have similar $CO:CO_2$ ratios and also lower, and relatively similar CO_2 reactivity. It is however, beyond the scope of this work to verify and gain a better understanding of these apparent correlations, and more experiments, preferably with a slower heating rate and a wider choice of cokes would be needed.

Corrected paragraph: Cokes B, C, D *and E* all have more than 5 times more surface CO than CO_2. This indicates that phenol, carbonyl, anhydride, ether and quinone surface groups are dominating in the cokes. *Some correlating trends between total sulfur content, CO_2 reactivity (mass loss evaluated) in Table 5.1 and the $CO:CO_2$ ratio can be observed.* It is however, beyond the scope of this work to verify and gain a better understanding of these apparent correlations, and more experiments, preferably with a slower heating rate and a wider choice of cokes would be needed.

Chapter 6 An EXAFS and XANES Study of V, Ni, and Fe Speciation in Cokes for Anodes Used in Aluminum Production

Gøril Jahrsengene[1], Hannah C. Wells[2], Camilla Sommerseth[3], Arne Petter Ratvik[3], Lorentz Petter Lossius[4], Katie H. Sizeland[5], Peter Kappen[6], Ann Mari Svensson[1] and Richard G. Haverkamp[2]

[1]Department of Materials Science and Engineering, NTNU Norwegian University of Science and Technology, Trondheim, Norway
[2]School of Engineering and Advanced Technology, Massey University, Palmerston North, New Zealand
[3]SINTEF Industry, Trondheim, Norway
[4]Hydro Aluminum AS, Primary Metal Technology, Årdal, Norway
[5]ANSTO, Lucas Heights, New South Wales, Australia
[6]Australian Synchrotron, ANSTO, Clayton, Victoria, Australia

Abstract

Lower-quality petroleum coke with higher levels of sulfur and metal impurities will have to be used for the manufacturing of anodes for aluminum production in the future. The sulfur and metallic impurities affect the anode properties in the aluminum production process, but the chemical identity of the metal species in the coke is not known. In this study, industrial petroleum cokes with high sulfur levels were analyzed by X-ray absorption near edge structure (XANES) and extended X-ray absorption fine structure (EXAFS) in order to determine the identity of the V, Ni, and Fe impurities. The XANES spectra were compared with pure-phase standards. EXAFS was used to compare the impurity metal structures with known crystal structures. It was found that V is present mainly as hexagonal V_3S_4. Ni is present mainly as hexagonal NiS, and Fe is present as hexagonal FeS. This knowledge of the chemical states of the metal elements in coke, which are known to affect anode performance, is the first step in understanding the mechanism of the action of these elements on anode reactivity.

6.1 Introduction

The Hall-Héroult process of producing aluminum by electrolysis of aluminum oxide using carbon anodes in a cryolite melt is the only commercial method to produce aluminum [1]. The global growth in the production of aluminum results in higher demands for of raw materials. The consumable carbon anodes are made from calcined petroleum coke (ca. 65 mass%), recycled anode butts (ca. 20 mass%) and coal tar pitch (ca. 15 mass%). The formed anodes are stacked and baked in an anode-baking furnace. To achieve a predictable and effective behavior in the cell, there are strict requirements on the calcined petroleum coke (CPC) quality. However, because of the increase in demand, combined with changes in the petroleum industry from which coke is a byproduct, the availability of high-quality coke is not keeping up with the demand [2]. The aluminum industry now needs to determine the impact on the smelting process of using lower quality cokes with higher metal and sulfur contents, which are closer to the quality of fuel grade coke.

Higher levels of impurities in the coke may affect the smelter operations due to changes in anode performance, cell performance (current efficiency), and changes in primary metal purity [3]. An important aspect of anode performance is the unwanted carbon reactions with air (airburn) and the produced CO_2 (carboxy reactivity). Both of these reactions increase carbon consumption. More noble metals than aluminum, such as V, Ni, and Fe, will be electrochemically reduced before aluminum, which results in reduction of the primary aluminum quality because the impurities end up in the tapped hot metal. The impurities will also affect the electrochemical performance, but the knowledge of such effects is still limited for realistic materials and operating conditions.

Some metal impurities have been shown to catalyze airburn or the CO_2 reactivity [3]. Vanadium is always present in crude oil and becomes concentrated in the heavier fractions, and therefore in the petroleum cokes, typically at a level of several hundred ppm in the coke. Vanadium has been shown to be an active catalyst for the CO_2 reaction of anodes at elevated temperatures [4]. Nickel is another impurity normally present in coke, and in higher concentration in poor-quality coke, which has been shown to have a negative effect on both air and carboxy reactivity [4, 5]. A third metal, iron is also present in coke, and may be derived from the crude oil or introduced unintentionally during processing [6]. Iron is an active catalyst for airburn and the CO_2 reaction [7]. Sodium is not very abundant in the coke but can enter the anodes from the use of butts [8, 9]. Other metals that occur in coke in lesser amounts can also affect these reactions. To avoid airburn, the anode is covered with anode cover material, usually a mix of

frozen bath and alumina. In modern cell operation, the airburn is limited due to good covering practice, but is still not insignificant. The reaction with CO_2 is more difficult to control, as it occurs between the electrochemically produced CO_2 and the anode carbon.

Sulfur levels also tend to increase in poorer-quality petroleum coke. Sulfur is believed to have a desirable inhibiting effect on the carboxy reactivity [10, 11], so portions of high sulfur coke are often blended in to reduce this reactivity. The nature of the inhibiting reaction is not known. Despite sulfur's positive effect on the carboxy reactivity, too high levels of S are unwanted because they leave the cell as SO_2 that contributes to acid rain if not scrubbed. Sulfur has been observed as thiophene-containing polycyclic aromatic hydrocarbons [12-15] in a variety of CPCs. In the high sulfur cokes studied here for metal impurities, a previous study showed that some sulfur is present in oxidation states close to zero, possibly as S-S bonds or elemental sulfur [16]. These cokes had a significantly lower CO_2 reactivity compared to total sulfur content and those with low levels of these sulfur compounds. A close-to linear relationship between sulfur and vanadium contents is observed in most cokes [2], although for the highest levels, there is a relatively large variation in the ratios of vanadium to sulfur.

X-ray absorption spectroscopy (XAS), consisting of X-ray absorption near edge structure (XANES) and extended X-ray absorption fine structure (EXAFS or XAFS), is a very powerful technique for identifying chemical speciation in solid state materials. XANES is normally used as a fingerprint method to compare the shape of the absorption edge region of standards to samples with unknown chemical structure. EXAFS is essentially a structure refinement technique where an atomic short-range (few Å) structure model is refined to determine nearest next neighbor distances and coordination numbers. It has a substantial advantage over X-ray diffraction techniques for crystal structures in that the structure of interest may be very dilute and highly dispersed or even amorphous and still be detected by EXAFS. The metals V and Ni are present in crude oil in large part as soluble organometallic complexes such as porphyrins where the metal is coordinated to N [17-19] and also non-porphyrin organic complexes where the metal is coordinated to S or O [20, 21]. The metals concentrate in the heavy fractions and thus in the coke rather than the light fractions. Less interest has been given to the nature of Fe in crude oil.

In this study, XANES and EXAFS are used to investigate the chemical speciation of the vanadium, nickel, and iron compounds in industrially produced petroleum cokes with varying levels of these metals and sulfur, also differing with respect to

structure, air, and CO_2 reactivity. These cokes have naturally occurring impurity levels (not obtained by doping), for which reactivity data are available and major sulfur speciation is known [16]. The cokes differ significantly in the overall levels of metallic impurities and sulfur, ranging from a relatively pure, anisotropic coke, to impure cokes, of which one is isotropic. The cokes also differ significantly with respect to the ratio of vanadium and sulfur. The aim here is to determine the chemical speciation of V, Ni, and Fe for the different cokes, and to identify possible correlations to the impurity levels, the ratio of vanadium and sulfur, and to the anode performance. This provides the basic knowledge for developing strategies on how to manage the impure anode cokes in the future, and the basic knowledge for improving the understanding of the effect of these elements on anode reactivity.

6.2 Experimental Section

6.2.1 Coke Selection

A large number of industrial calcined petroleum cokes originating from different crude oils and produced by different manufacturers were analyzed by X-ray fluorescence spectroscopy (XRF) according to ISO 12980:2000 for metal and sulfur contents. From the available cokes, a selection of six coke samples were chosen based on sulfur and vanadium contents to give a range of S and V contents. Cokes A-E are the same as those used in a recent XANES study by the same authors for the sulfur speciation [16], where sulfur speciation using XANES were reported and evaluated with respect to CO_2 reactivity and structure. Cokes A-D, and the additional F, are anisotropic in nature similar to regular anode coke, while coke E is isotropic. The S, V, Ni, and Fe composition for each of the six selected petroleum cokes samples is detailed in Table 6.1.

Table 6.1: Composition the six cokes.

	S (mass%)	V (ppm)	Ni (ppm)	Fe (ppm)
Coke A	1.42	116	192	178
Coke B	3.56	402	210	264
Coke C	5.54	432	192	316
Coke D	3.86	714	426	156
Coke E	4.42	624	323	464
Coke F	4.76	541	234	724

Sulfur (S) and metal content were measured on coke materials using XRF.

6.2.2 XAS Measurement and Analysis

The cokes were ground to < 45 μm with a mortar and pestle, without dilution, before mounting for XAS as packed powders in standard 1 mm thick poly(methyl methacrylate) sample holders.

X-ray absorption spectra were recorded on the wiggler XAS beamline ID12 at the Australian Synchrotron, Victoria, Australia (Figure 6.1). The energy was controlled using a fixed exit Si(111) double crystal monochromator. The beam was conditioned using a collimating mirror (Si) and a toroidal focusing mirror (Rh coated). Higher harmonics were rejected using these two mirrors and a flat harmonic rejection mirror (SiO_2). Spectra were recorded in fluorescence mode using a 100-element Ge pixel array fluorescence detector (*Canberra*). An ion chamber (*Oken*) was used to monitor incoming beam intensity. The X-ray beamsize on the sample was approximately 1 x 1.5 mm. The energy scale was calibrated by simultaneously measuring a metal foil (V, Ni, or Fe) placed between two downstream ion chambers (*Oken*). XAS spectra were recorded around the *K*-edges of Fe, Ni and V, respectively, at room temperature.
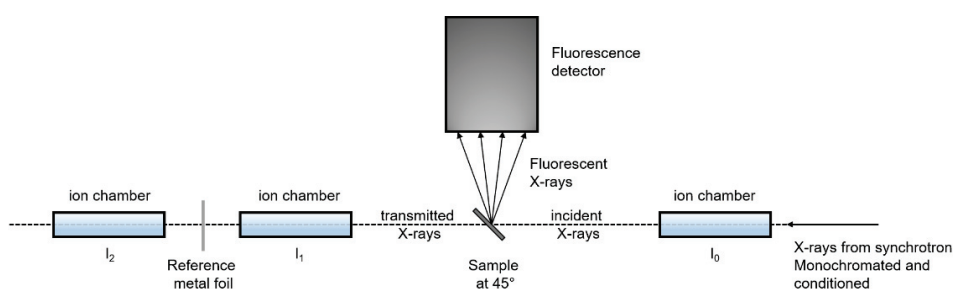
Figure 6.1: Experimental setup for XAS analysis.

A number of reference standards for each element were also run with the intention to use these for XANES analysis and to enable an experimental value of the amplitude reduction factor, S_0^2, from similar chemical structures for fitting of samples to EXAFS models. To avoid self-absorption effects, reference materials were diluted with cellulose powder to suitable concentrations of the element and finely ground (Table 6.2). Data were collected with variable energy steps and constant dwell time best suited for XANES (use of data for EXAFS was of secondary importance). Pre-edge data was collected at 3 eV energy intervals, around the edge at 0.25 eV intervals, above the XANES region at steps of $k = 0.07$ Å^{-1} up to $k = 10$ Å^{-1} above the edge with a dwell time of 1.0 s at each step.

Table 6.2: Concentration of V, Ni and Fe reference standards obtained by mixing with cellulose.

Material	Concentration (ppm)	Producer
Vanadium		
Vanadium foil	-	
V_2O_3	5000	Sigma Aldrich
VO_2	5000	Sigma Aldrich
V_2O_5	5000	Sigma Aldrich
V_2S_3	5000	American Elements
VC	3333	Sigma Aldrich
2,3,7,8,12,13,17,18-Octaethyl-21H,23H-porphine vanadium(IV) oxide	2000	Sigma Aldrich
$VOSO_4$	5000	Sigma Aldrich
Nickel		
Nickel foil	-	
NiO	1000	Sigma Aldrich
Ni_3S_2	1000	Sigma Aldrich
2,3,7,8,12,13,17,18-Octaethyl-21H,23H-porphine nickel(II)	1000	Sigma Aldrich
Iron		
Iron foil	-	
FeO	10000	Sigma Aldrich
Fe_2O_3	1000	Sigma Aldrich
Fe_3O_4	1000	Sigma Aldrich
$FeSO_4 \cdot 7H_2O$	1000	Chemi-Teknik AS
FeS	10000	Sigma Aldrich
FeS_2	10000	The Crystal People, Christchurch, New Zealand
Fe_3C	15000	American Elements
5,10,15,20-Tetraphenyl-21H,23H-porphine iron(III) chloride	1000	Sigma Aldrich

The multichannel fluorescence data were pre-processed by averaging and normalizing the individual channels after dead-time correction; this step was performed using the software tool Sakura [22].

Processing of XANES used the Athena software [23]. Analysis was performed with the averaged spectra of three scans for V, two or three for Fe, while only a single scan was obtained for the Ni measurements.

For the Ni and Fe XANES spectra of the cokes, linear combination fitting (LCF) of normalized $\mu(E)$ spectra of reference compounds was performed with Athena software. The X-ray edge position, E_0, was held to be the same for all components. Nonlinear least squares minimization was used for fitting and was carried out over an energy range 20 eV below E_0 to 50 eV above E_0. After initial screening of the reference spectra with the coke spectra the final LCF's used a combination of the most promising reference compounds. Linear combination fits were also tested with the derivative $\mu(E)$ spectra.

The EXAFS region for V, Ni, and Fe were processed using Artemis software [23] and fitted to crystal data from the crystallography open database (COD) [24] after removal of a glitch in the V K-edge at 5727 eV. A glitch was also present for the Ni K-edge at 8650-8660 eV but this region of the EXAFS spectrum ($k > 9$ Å^{-1}) was not used in the fitting as it had poor signal-to-noise ratio.

EXAFS fitting was carried out in each of k, k^2, k^3 and R space, with similar results obtained in all of these. The results reported here are fitting in R (with k^2). The XAS data were recorded to $k = 10$ Å^{-1} but the higher energy data were not of sufficient quality for useful fitting (as judged by visual inspection), so fitting was terminated at lower k, typically around 8.0-8.5 Å^{-1}. The goodness of fit was determined by the EXAFS R-factor and by a visual inspection of the matching of the shape of the fit compared with the data. Importantly, the value of S_0^2 obtained from an unconstrained fit was required to be in a realistic range, and similar to that for the fit to a standard of a similar composition. The crystallographic structures for a variety of possible compounds were tested against the data for the cokes.

6.2.3 Air Reactivity
Air reactivity was measured on anodes prepared from the cokes using thermogravimetric analysis similar to ISO 12989-1.

6.3 Results and Discussion

6.3.1 Nickel XANES

The reference compounds for Ni XANES display very significant differences in both the edge energy and the shape (Figure 6.2).
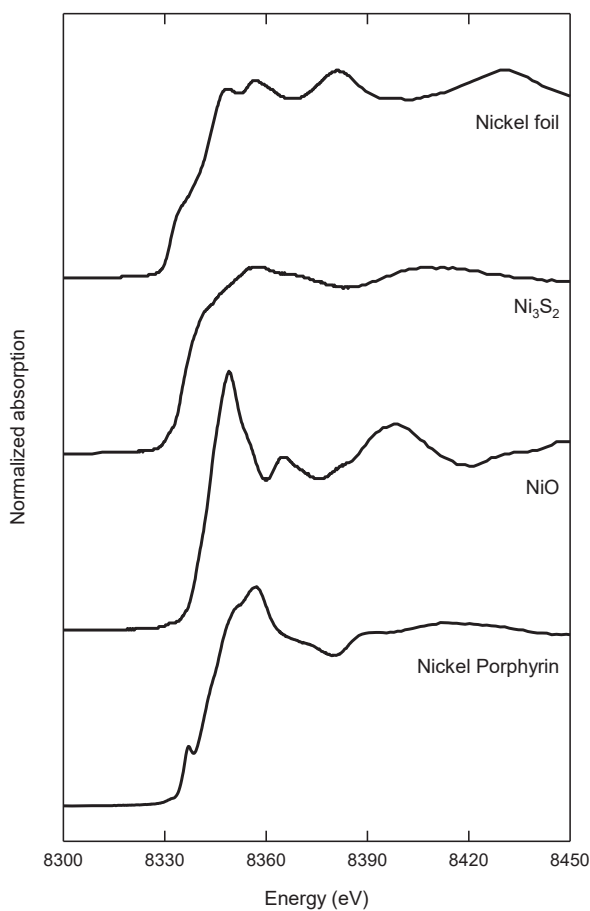
Figure 6.2: The normalized absorption nickel *K*-edge XANES spectra for the reference compounds.

The Ni *K*-edge XANES of all the five cokes appear similar. The coke D spectrum is presented here because it has the highest level of Ni in these cokes and therefore the best signal to noise ratio (refer to Electronic Supplementary Material, Fig. S-1).

Comparing the spectrum of coke D to the reference spectra measured, a moderately good match above the absorption edge was found for Ni_3S_2 (Figure 6.3). However, the absorption edge of the coke spectrum is shifted to higher energies. The fit is improved if a linear combination fit of Ni_3S_2 with nickel porphyrin is used (Figure 6.4a). Nickel porphyrin is used as an approximate representation a range of possible nickel organic complexes. All the cokes were similar, and any subtle differences between the different cokes can be accommodated by varying the proportions of Ni_3S_2 and nickel porphyrin, particularly the fit at the main edge (Supplemental Material File, Table S-I). Other combinations of reference spectra gave poorer fits.
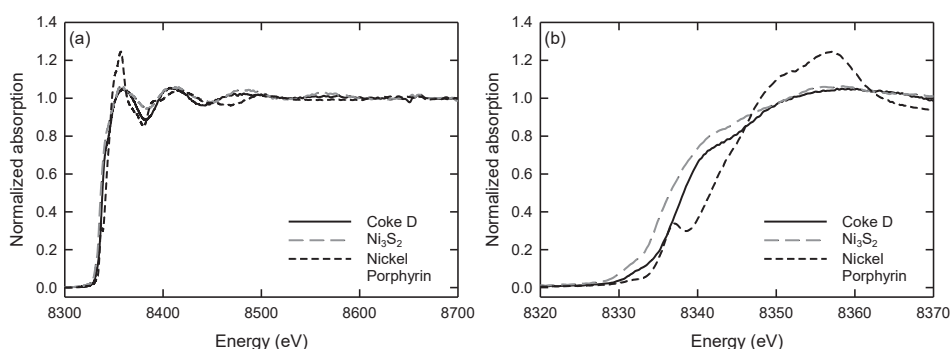
Figure 6.3: The normalized absorption nickel *K*-edge XANES spectra for industrial coke D with reference spectra nickel porphyrin and Ni_3S_2. **(a)** Whole energy region; **(b)** edge region.

The limitation of XANES must be recognized, however. Comparisons of the sample spectra are possible only to the reference spectra available. These reference spectra may not include compounds that are identical to those in the sample, and therefore a perfect match may not always be obtained. However, it would normally be expected that compounds with similar chemistry, and particularly oxidation state, may have similar XANES spectra, specifically at the edge, and this gives some confidence that the form of Ni present is similar to a nickel sulfide.
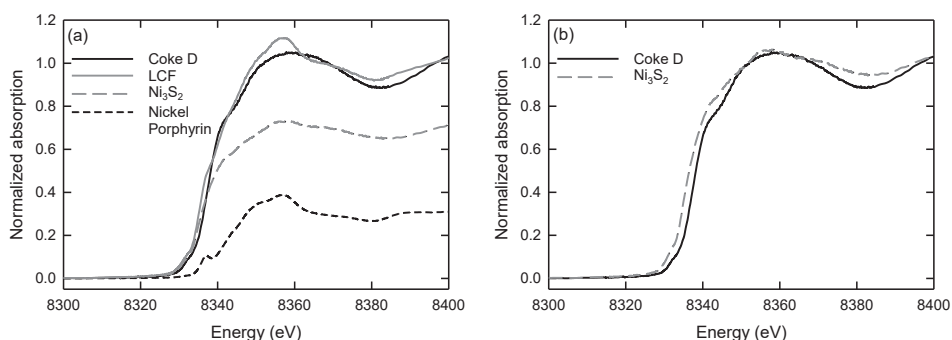
Figure 6.4: (a) The linear combination fitting of the normalized absorption nickel K-edge XANES spectra with Ni_3S_2 (0.688) and nickel porphyrin (0.312) to coke D. R-factor 0.009. **(b)** Coke D with only Ni_3S_2 gives R-factor 0.019.

The XANES analysis for Ni therefore suggests that nickel may be present as a sulfide or a complex organic sulfur compound or a mixture of the two. While there is some variation in the proportion of each of these between the cokes, the best fit for all of the cokes is with only these two components.

6.3.2 Nickel EXAFS

The Ni K-edge EXAFS data from the cokes were tested against a range of possible structures (Table 6.3). Two stoichiometries, NiS and NiS_2, gave satisfactory fits. Ni_3S_2 did not fit well to the experimental data. The best fit was obtained using a hexagonal form of NiS (Figure 6.5), and the fit improved by assuming that there is only short-range order (shorter electron scattering paths). This suggests that nickel is highly dispersed and does not form crystals with long-range order in the coke. However, the data were recorded only up to $k = 9$ and therefore the resolution is limited. While it appears that only short-range order is present, EXAFS amplitudes become weak above $k = 8$ and some caution should be applied regarding the validity of this interpretation.

Table 6.3: Crystal structures tested for fit to the EXAFS of the cokes.

Compound	COD ID	Space group	Crystal system
NiS	1010435	P 6_3 / m m c	Hexagonal
NiS	1011038	R 3 m	Trigonal
Ni_3S_2	1011250	R 3 2	Trigonal
NiS_2	1544738	P a -3	Cubic
NiO	1010093	F m -3 m	Cubic
Ni_3C	1528750	R -3 c	Trigonal
Ni	9013024	F m -3 m	Cubic

The EXAFS analysis indicates a sulfide in the cokes with bond lengths similar to primitive hexagonal NiS. Other plausible possibilities considered in petroleum coke, including NiO, Ni_3C, and Ni, did not give good fits, with either unrealistic S_0^2 values (which should be close to 1), large ΔE_0 (> 5) or poor (high) R-factors (refer to Supplemental Material File).
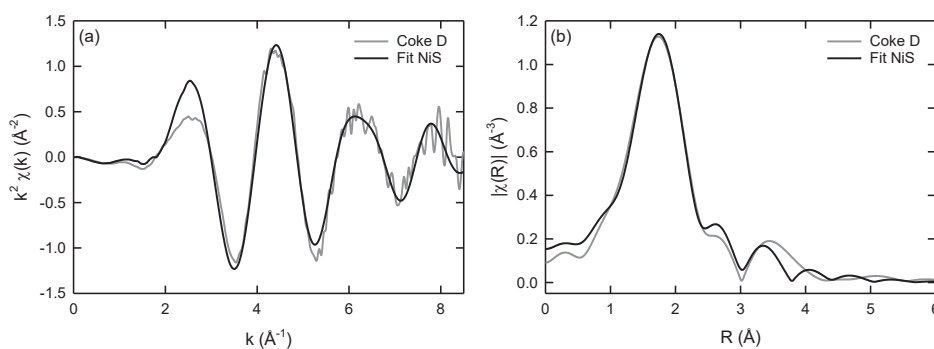
Figure 6.5: The experimental EXAFS spectrum for coke D and the FEFF model fit for hexagonal (P 6_3 / m m c) NiS fitted for k from 3 to 8 Å^{-1} in **(a)** k^2-space and **(b)** R-space. R-factor = 0.014, S_0^2 = 1.08, ΔE_0 = 0.08 for all paths < 4.10 Å.

In summary, the Ni XANES suggested a nickel sulfide with possibly some admixture of porphyrin, while the EXAFS analysis indicates that the cokes contain a sulfide with a structure similar to NiS primitive hexagonal P 6_3 / m m c, likely with only short-range order.

6.3.3 Vanadium XAS

The reference compounds for V XANES display significant differences in the shapes and pre-edge features, although not displaying a large change in the edge position (Figure 6.6).

Figure 6.6: The normalized absorption vanadium K-edge XANES spectra for the reference compounds **(a)** sulfide, carbide, porphyrin and sulfate; **(b)** metal and oxides. Adapted from [25] with permission.

The V K-edge XANES of all five cokes appeared similar [25]. The Coke D spectrum is presented here (Figure 6.7) because it has the highest level of V of these cokes and therefore the best signal-to-noise ratio (other data are available in Supplemental Material File, Fig. S-2). A pre-edge peak is observed in the spectra of all cokes at 5466.6 eV, while in the reference compounds, this pre-edge occurs at 2 to 3 eV higher energy. The main edge, located at 5471.1 to 5471.9 eV in the cokes, occurs 6 to 11 eV higher in the reference compounds (except V metal). The edge energy is characteristic of the oxidation state of V [26]. Comparison of the observed pre-edge and edge position of the vanadium K-edge spectra for cokes

with the spectra for the reference standards (Table 6.1) showed that none of the investigated references gave a good fit, as exemplified in Figure 6.7b. However, from the XANES data, it is evident that the vanadium speciation is the same in all the cokes.
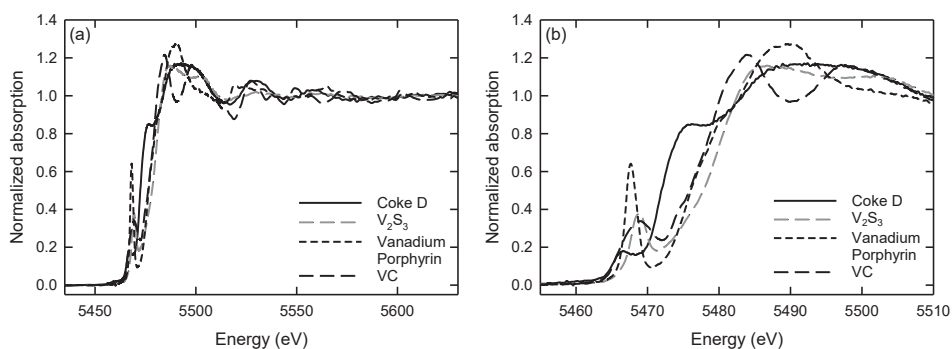
Figure 6.7: The normalized absorption vanadium K-edge XAS spectra for industrial coke D with reference spectra of VC, vanadium porphyrin, and V_2S_3. **(a)** Whole energy region; **(b)** edge region.

6.3.4 Vanadium EXAFS

The EXAFS region for the V K-edge of each coke was modeled for a variety of vanadium structures (Table 6.4).

Table 6.4: Crystal structures tested for fit to the EXAFS of the cokes.

Compound	COD ID	Space group	Crystal system
V_3S_4	2001606	P 6_3 / m	Hexagonal
V_3S_4	1537894	C 1 2 / m 1	Monoclinic
VS	1010579	P 6_3 / m m c	Hexagonal
V_2O_3	1537656	R -3 c	Trigonal
VC	1011321	F m -3 m	Cubic
V	9012770	I m -3 m	Cubic

The best fits of the coke data to structural models were obtained for hexagonal (P 6_3 / m) V_3S_4 (see Figure 6.8 and Supplemental Material File Tables S-III and S-IV). In Figure 6.8 we display the fit with S_0^2 constrained to 0.75; however, if left unconstrained, S_0^2 settled at 0.51 with a slightly improved fit but little change to the other parameters.

No other possibilities considered for V in coke, including two other forms of sulfide, trigonal V_2O_3, and cubic VC, gave good fits.

The crystallographic structure for V_2S_3 is not available as a CIF file which raises the possibility that despite this named compound being sold by commercial chemical suppliers and chosen here as a reference standard for XANES, the structure may not exist (although the alternative is simply that the structure has not been deposited in the databases). However, in view of the very good fit for the EXAFS with V_3S_4 and the poor fit of the XANES with "V_2S_3", it does not appear necessary to evaluate V_2S_3 in EXAFS.
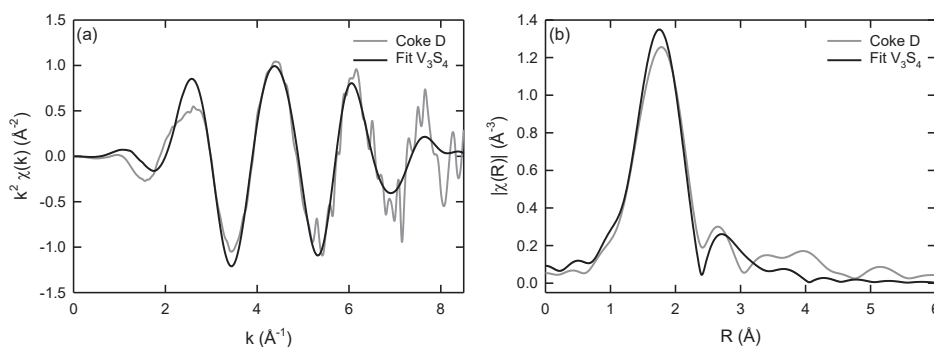
Figure 6.8: The experimental EXAFS spectrum for coke D and the FEFF theoretical fit for V_3S_4 hexagonal (P 6_3 / m) fitted for k from 2 to 8.5 Å^{-1} in **(a)** k^2-space and **(b)** R-space. R-factor = 0.068, S_0^2 = constrained to 0.75, ΔE_0 = -3.80 all paths < 4.11 Å.

The EXAFS analysis indicates that the vanadium is bound as a sulfide in the form of hexagonal P 6_3 / m V_3S_4 for all the cokes evaluated.

6.3.5 Iron XANES

The reference compounds for Fe XANES display significant differences in the shape, although not displaying a large change in the edge position (Figure 6.9).

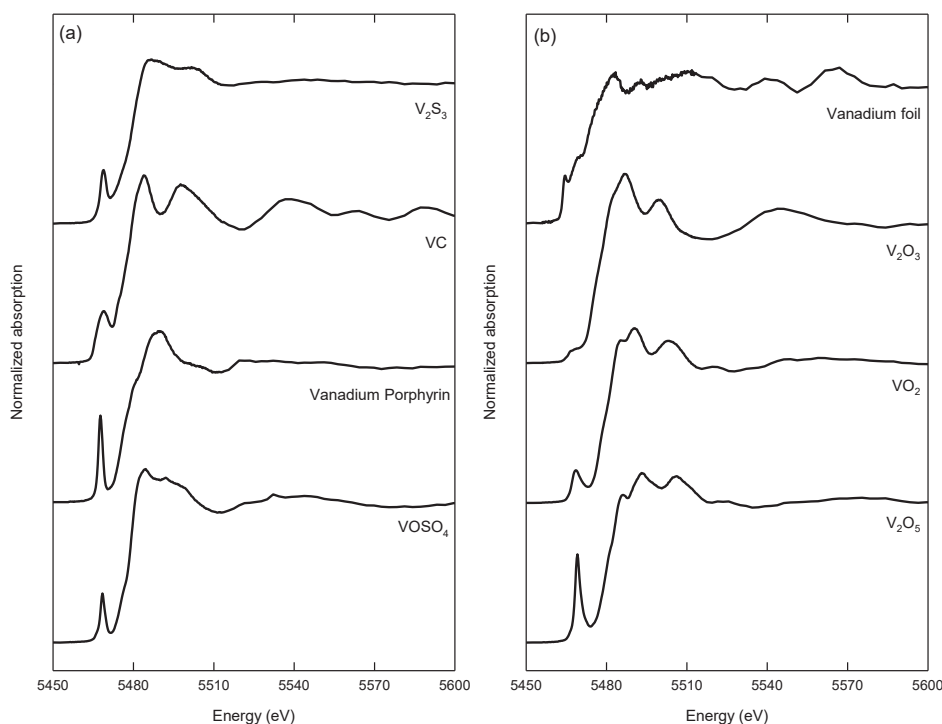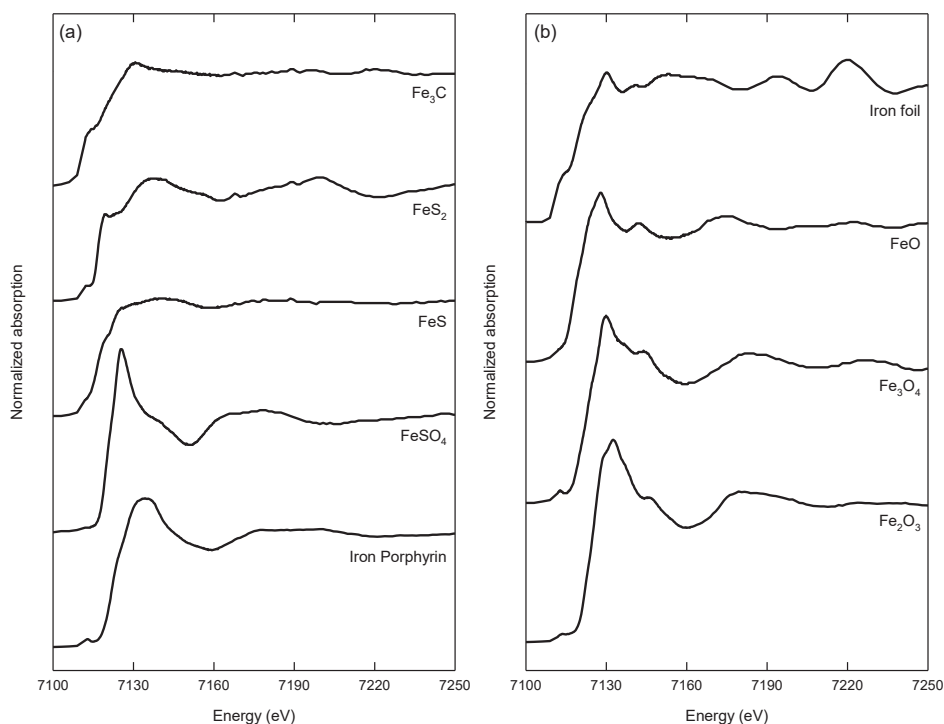**Figure 6.9:** The normalized absorption F K-edge XANES spectra for the reference compounds **(a)** carbide, sulfides, sulfate, and porphyrin; **(b)** metal and oxides.

All the cokes show similar Fe K-edge XANES spectra (Supplemental Material File, Fig. S-6). The sulfides, FeS, and FeS_2, are relatively good matches to the coke (Figure 6.10). Iron porphyrin has a small pre-edge and then a higher-energy edge than the coke spectra, so it does not match the coke Fe K-edge spectra well. However, a small portion of iron porphyrin could shift the edge slightly and perhaps account for some of the differences between the spectra.
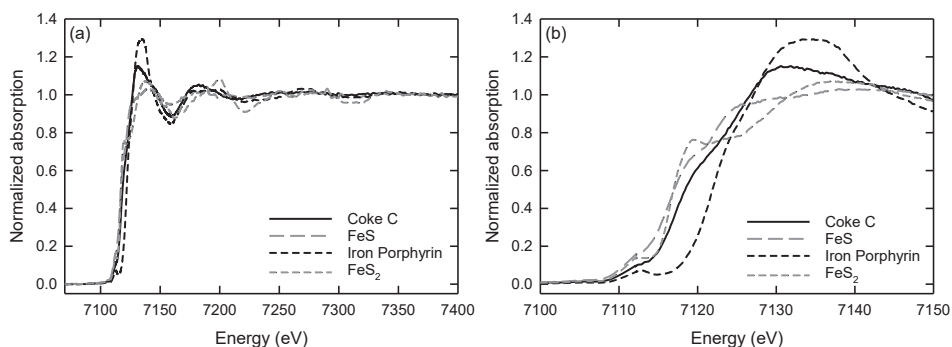
Figure 6.10: The normalized absorption iron *K*-edge XAS spectra for industrial coke C with reference spectra iron porphyrin, FeS_2 and FeS. **(a)** Whole energy region; **(b)** edge region.

The LCF provides estimates of the relative proportion of FeS, FeS_2, and iron porphyrin in the cokes (with more fits in Supplemental Material File, Table S-V), as shown in Figure 6.11 for cokes C and E. The ratio of FeS and FeS_2 varies between the cokes with approximately one third or less of the Fe as organic iron porphyrin. Using only one of the sulfides and porphyrin in the fitting yields approximately the same results for the fraction of porphyrin *vs* total sulfides, although Figure 6.11 shows small variations between the edge positions possibly explained by differences in the type of sulfides. Using the normalized derivative spectrum gives slightly less porphyrin and FeS, with the increasing FeS_2 for all cokes. The results thus show that most iron in the cokes is bound as sulfides but some proportion of iron porphyrin cannot be ruled out.
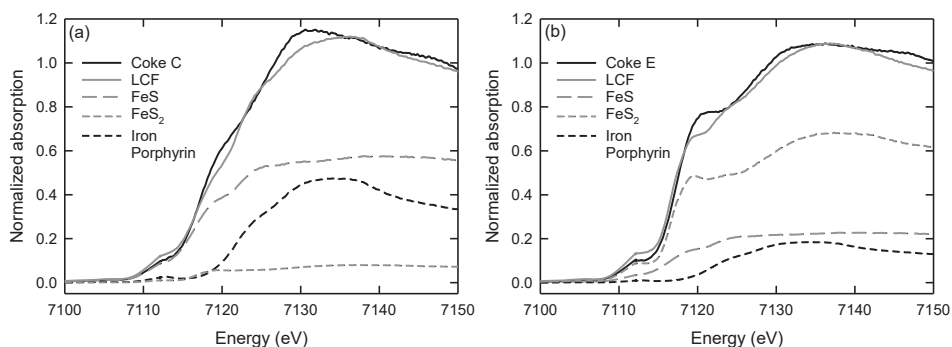
Figure 6.11: The linear combination fitting of the normalized absorption iron *K*-edge XANES spectra with nickel porphyrin, FeS_2, and FeS to **(a)** coke C fitted with FeS (0.559), FeS_2 (0.075), and iron porphyrin (0.366) giving an R-factor of 0.012, and **(b)** coke E fitted with FeS (0.221), FeS_2 (0.637), and iron porphyrin (0.142) giving an R-factor of 0.013.

6.3.6 Iron EXAFS

For modeling of the EXAFS region, the spectra from the low iron cokes A, B, and D are not of good enough quality for analysis. Therefore, EXAFS modelling was only performed on cokes C, E, and F. A variety of crystal structures (Table 6.5) were modeled and fitted to the spectra for the cokes. Of these, only the iron sulfide compounds, FeS and FeS_2, gave reasonable fits (Supplemental Material File, Table S-VI).

Table 6.5: Crystal structures tested for fit to the EXAFS of the cokes.

Compound	COD ID	Space group	Crystal system
FeS	1009043	P -6 2 c	Hexagonal
FeS_2	1011013	P n n m	Orthorhombic
FeS_2	1544891	P a -3	Cubic
FeO	1011198	F m -3 m	Cubic
Fe_3C	1008725	P n m a	Orthorhombic
Fe	9013463	I m -3 m	Cubic

The best fits (low R-factor, S_0^2 close to 1, $\Delta E_0 < 5$, good shape match) were obtained for hexagonal (P -6 2 c) FeS (Coke E in Figure 6.12) but reasonable fits were also obtained for orthorhombic (P n n m) FeS_2. Fitting was much improved by considering only short-range order and not including any paths containing Fe-Fe. This suggests that the Fe is highly dispersed and does not form crystals with

long-range order in the coke, although with the caution noted previously that the EXAFS data is recorded only up to $k = 9$ so the interpretation of short-range order may not be accurate.

Other possibilities considered for Fe in coke, including FeO and Fe_3C, did not give good fits, with either unrealistic S_0^2 values, large ΔE_0 (> 5) or poor (high) R-factors.
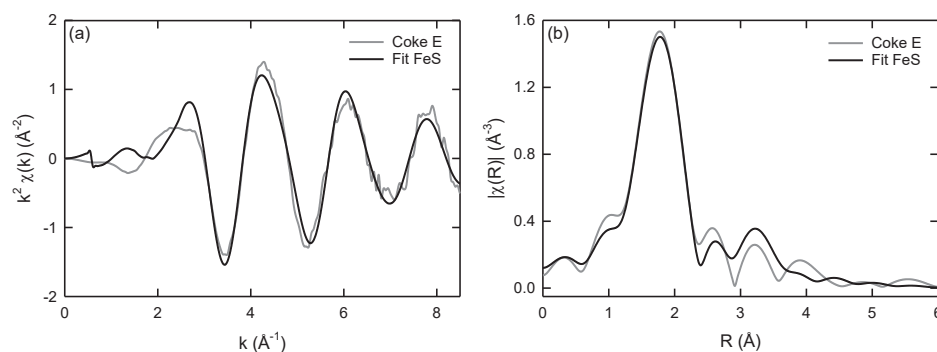
Figure 6.12: The experimental EXAFS spectrum for coke E and the FEFF theoretical fit for FeS hexagonal (P -6 2 c) fitted for k from 3 to 8.5 Å^{-1} in **(a)** k^2-space and **(b)** R-space. R-factor = 0.029, S_0^2 = 0.78, ΔE_0 = 1.20 using all S-Fe and S-S-Fe paths < 4.30 Å (excluding any path with Fe-Fe interaction).

In summary, the Fe XANES analysis suggested FeS_2 and FeS with some Fe porphyrin, while EXAFS analysis indicates that the cokes contain a sulfide with a structure similar to FeS hexagonal P -6 2 c, with short-range order.

6.3.7 Metal Species in Petroleum Coke

A good knowledge of the metal species present in the coke is provided by these XANES and EXAFS analyses. Each of the three elements studied (V, Ni, and Fe) is present mainly as a sulfide (where just a single structure was fitted). The sulfides are all hexagonally structured: NiS is primitive hexagonal P 6_3 / m m c, V_3S_4 is hexagonal P 6_3 / m and FeS is hexagonal P -6 2 c. For Fe and Ni there is likely only short-range order. Short-range order means one of two things - either the compound is highly disordered with no long-range-ordered crystallites or molecular structure, or the compound is highly dispersed within the coke matrix. For V_3S_4, a good fit was obtained without the necessity of assuming very short-range order only.

There were no major differences in the chemistry of V, Ni and Fe between the six cokes studied.

6.3.8 Origin and Development of the Metal Chemistry in Coke

The metals V and Ni in coke are derived from crude oil. In crude oil, these elements are found as soluble organometallic complexes, dominated by porphyrins where the metal is coordinated to N [17-19] and also non-porphyrin organic complexes where the metal is coordinated to S or O [20, 21]. The V is mostly present as porphyrins in the more widely studied maltene (light) fraction of crude oil, but it is also present in porphyrins in the asphaltene (heavier) fraction [19]. Quite a wide range of V porphyrins exists in crude [27]. It is believed that the porphyrin complexes are derived from chlorophyll in the plant matter from which these deposits are derived (a Mg containing porphyrin), and from heme from animal matter (a Fe containing porphyrin). Iron is present in crude oil as a mixture of organic acid salts and iron complexes [28]. The Mg is then exchanged with V and Ni during formation of the crude oil. During processing of crude oil, the metals concentrate in the heavy fractions and thus end up in the coke byproduct rather than the light fractions.

The chemistry of V and Ni has been studied in petroleum cracking residues and petroleum cokes produced at low temperatures. Initially much of the Ni and V in Mayan residuum asphaltene is found (by XAS) to be present as porphyrins. However, after cracking at 425 °C and 150 bar, the residue contains only 10 % of the Ni and V as porphyrins with the remainder in octahedral coordination [29]. Therefore, at these temperatures, Ni and V porphyrins decompose and are converted to other forms. However, in petroleum cokes produced from oil sands such as the Athabasca Oil Sands of northern Alberta, Canada, where petroleum coke is produced during upgrading of oil sands bitumen to synthetic crude oil, and the coke has high S and high metal contents [30], much of the Ni and V (studied with XANES) remains as porphyrins [31]. These oil sand cokes are produced at lower temperatures (ca. 500 °C) than the cokes in the study presented here (1200-1250 °C), suggesting that the porphyrins are relatively stable at lower temperatures but are converted to sulfides at the temperatures typically used to produce coke suitable for anode production.

The Fe in the coke samples studied here appears to have been converted from an unknown form in the oil to FeS. Fe possibly started as porphyrins (this was not investigated), and can also unintentionally be introduced from equipment during processing [6], however, in the lower temperature treated oil sand cokes, Fe has been found (with XANES) to be present as thiophenic coordination and pyritic-

ilmenitic (FeS2-FeTiO3) coordination [32]. In high-sulfur petroleum coke from a refinery, prepared at 950-1100 °C, Fe was found mostly in the form of Fe_3C (using XRD), but, on CO_2 gasification, some Fe reacted with S to form FeS, while some was reduced to metallic Fe^0 and some was oxidized to FeO, Fe_2O_3, and Fe_3O_4 [33]. Therefore, the FeS found in the petroleum cokes studied here, considering the conditions of formation of the coke, is consistent with other studies [28].

The metal sulfides have formed within a carbon matrix. The EXAFS study here found the metal sulfides are all hexagonally structured (although there are many sulfides known that do not have hexagonal structures) and likely with only short-range order for the Ni and Fe sulfides. The graphite matrix in which these sulfides form has a hexagonal P 6_3 m c structure. Therefore, hypothetically, it may be assumed that the aromatic compound has acted as a template in the formation of these sulfides during heating to form coke. Considering the origin of these compounds, derived from species soluble in the organic phase, where the metals start out highly dispersed, it seems likely that they also remain highly dispersed when the coke is formed with limited ability to coalesce, rather than ending simply amorphous. Therefore, the metal sulfides are likely not present as inclusions. Mapping of oil sands cokes show a broad and fairly uniform distribution of V and Ni with only slight concentration increases at the surfaces of the coke particles, which supports the above assumption [30, 31].

6.3.9 Sulfur Chemistry in Cokes

The S in cokes is only partially tied up in the metal sulfides. V, Ni, and Fe sulfides in these cokes only account for ca. 1 % of the total sulfur in the coke. The dominant form of the S in coke is not as metal sulfides, but appears to be in the form of organic or S-S bound sulfur [16].

6.3.10 Metal Sulfides and Anode Reactivity

It has previously been established that the presence of certain metals in anodes affects the reactivity. Vanadium has been proposed to be an active catalyst for the carboxy reactivity of anodes at elevated temperatures [3, 4], and for air reactivity [34]. The same is proposed for nickel where high contents have been shown to have a negative effect on both air reactivity and carboxy reactivity [4, 5]. Fe is also an active catalyst for air reactivity and the CO_2 reaction [7] to the extent that it will increase the CO_2 gasification catalytic reactions of petroleum coke [35]. In the study presented here, we have shown that the metals are present as sulfides of V, Ni, and Fe. This provides the option to investigate how these particular metal species influence the airburn and carboxy reactions, considering that the detailed mechanisms of the reactions involving the metal compounds have not yet been

established. The knowledge of the identity of the metal compounds will clearly be useful for the further understanding of the catalytic effects of these metals, and also in order to develop methods for poisoning these metal sulfide "reactivity catalysts" to mitigate the negative effect of high metal impurity levels. Most of these cokes have been thoroughly investigated with respect to the carboxy reactivity [16], while Figure 6.13 shows the relationship between the air reactivity and the specific metals (measurements on baked anodes of the respective cokes). The air reactivity generally increases with the metal content, although the individual effect of each metal is difficult to establish with these types of industrially produced cokes.
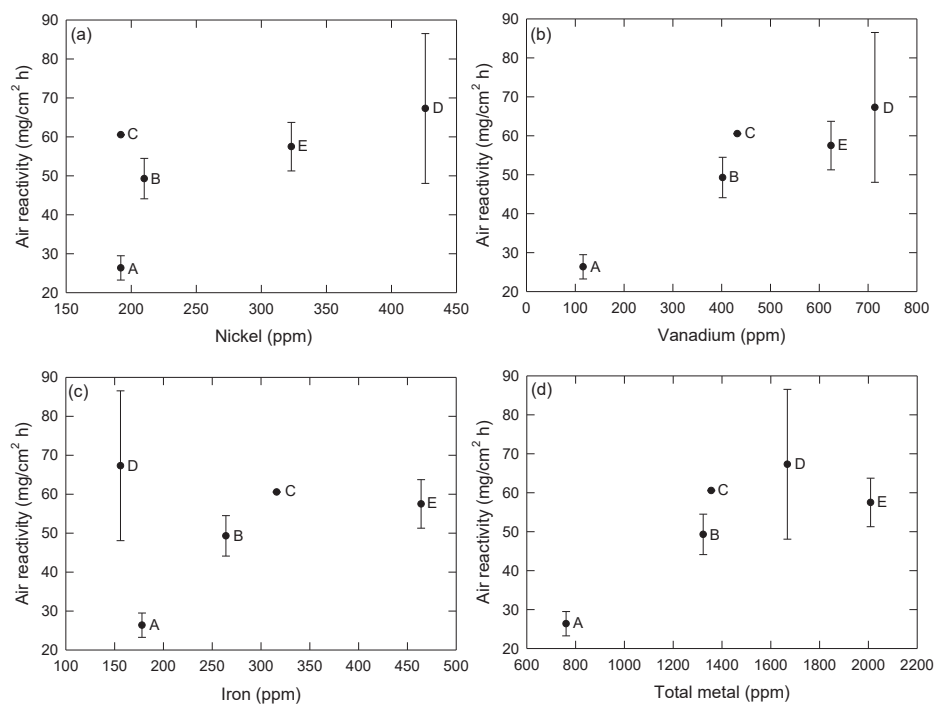
Figure 6.13: Air reactivity *vs* the metal concentration in the anodes made from the different cokes. Air reactivity relative to **(a)** Ni concentration; **(b)** V concentration; **(c)** Fe concentration; **(d)** total metal concentration. (Points corresponding to each coke are labelled A through E).

6.4 Conclusions

It has been shown for high-sulfur cokes containing high levels of V, Ni, and Fe that, contrary to the commonly accepted view, these are likely present as hexagonal sulfides rather than as metal porphyrins. The metals are very highly dispersed through the carbon matrix, and they are not present as large crystalline inclusions. These sulfides arise from reactions that occur during production of green coke, and are derived from the soluble metal porphyrins and other organic complexes in the heavy oil fractions. Only a small portion of the S present in the coke is bound as metal sulfides as the bulk of the sulfur is present as organic sulfur and S-S bonded sulfur. It has been established that the presence of the V, Ni, and Fe affects the air reactivity and CO_2 reactivity, acting as a catalyst for these reactions. Although this study has not investigated the mechanism by which the catalysis occurs, this new knowledge of the chemical species present will be very useful for further studies to understand the catalytic reactions.

Acknowledgements

Abbreviation	Full name
COD	Crystallography Open Database
CPC	Calcined Petroleum Coke
EXAFS	Extended X-ray Absorption Fine Structure
LCF	Linear Combination Fit
XAFS	X-ray Absorption Fine Structure
XANES	X-ray Absorption Near Edge Structure
XAS	X-ray Absorption Spectroscopy
XRD	X-Ray Diffraction
XRF	X-Ray Fluorescence

References

[1]   J. Thonstad, P. Fellner, G.M. Haarberg, J. Híveš, H. Kvande and Å. Sterten. *Aluminium Electrolysis: Fundamentals of the Hall-Héroult Process.* 3rd ed. Aluminium-Verlag: Düsseldorf, 2001.

[2]   L. Edwards. The History and Future Challenges of Calcined Petroleum Coke Production and Use in Aluminum Smelting. *JOM* (2015), **67**(2), pp. 308-321.

[3]   G.J. Houston and H.A. Øye. Consumption of anode carbon during aluminium electrolysis. I-III. *Aluminium* (1985), **61**, pp. 251-254, 346-349, 426,428.

[4]   T. Eidet and J. Thonstad. Effects of Sulphur, Nickel and Vanadium on the Air and CO_2 Reactivity of Cokes. *Light Metals* (1997), pp. 436-437.

[5]   Z. Li, N. Zhang and L. Wen. Effect of Nickel Content on Carbon Anode Reactivity. *Asian J. Chem.* (2016), **28**(8), pp. 1703-1707.

[6]   L. Edwards. Impurity Level Distribution in GPC and CPC and Impact on Anode Properties. *Light Metals* (2014), pp. 1093-1098.

[7]   T. Eidet, J. Thonstad and M. Sørlie. Effects of Iron and Sulphur on the Air and CO_2 Reactivity of Cokes. *Light Metals* (1997), pp. 511-517.

[8]   J.d.S. Batista and B.I.d. Silveira. Influence of the Sodium Content on the Reactivity of Carbon Anodes. *Mater. Res. (Sao Carlos, Braz.)* (2008), **11**, pp. 387-390.

[9]   S.M. Hume, W.K. Fischer, R.C. Perruchoud, J.B. Metson and J.B. Baker. Influence of Petroleum Coke Sulphur Content on the Sodium Sensitivity of Carbon Anodes. *Light Metals* (1993), pp. 535-541.

[10]   Y.D. Bensah and T. Foosnaes. The Nature and Effect of Sulphur Compounds on CO_2 and Air Reactivity of Petrol Coke. *ARPN J. Eng. Appl. Sci.* (2010), **5**(6), pp. 35-43.

[11]   M. Sørlie. Effect of Sulphur on Anode Reactivity and Rlectrolytic Consumption. *Light Metals* (1994), pp. 659−665.

[12]   S.J. Hay, J. Metson and M.M. Hyland. Sulfur Speciation in Aluminum Smelting Anodes. *Ind. Eng. Chem. Res.* (2004), **43**(7), pp. 1690-1700.

[13]   J. Xiao, Q. Zhong, F. Li, J. Huang, Y. Zhang and B. Wang. Modeling the Change of Green Coke to Calcined Coke using Qingdao High-Sulfur Petroleum Coke. *Energy Fuels* (2015), **29**(5), pp. 3345-3352.

[14]   Q. Zhong, J. Xiao, H. Du and Z. Yao. Thiophenic Sulfur Transformation in a Carbon Anode during the Aluminum Electrolysis Process. *Energy Fuels* (2017), **31**(4), pp. 4539-4547.

[15]   J. Xiao, S.-y. Deng, Q.-f. Zhong and S.-l. Ye. Effect of sulfur impurity on coke reactivity and its mechanism. *Trans. Nonferrous. Met. Soc. China* (2014), **24**(11), pp. 3702-3709.

[16]   G. Jahrsengene, H.C. Wells, S. Rørvik, A.P. Ratvik, R.G. Haverkamp and A.M. Svensson. A XANES Study of Sulfur Speciation and Reactivity in Cokes for Anodes Used in Aluminum Production. *Metall. Mater. Trans. B* (2018), **49**(3), pp. 1434-1443.

[17]   G. Caumette, C.P. Lienemann, I. Merdrignac, B. Bouyssiere and R. Lobinski. Element Speciation Analysis of Petroleum and Related Materials. *J. Anal. Atom. Spectrom.* (2009), **24**(3), pp. 263-276.

[18]   J. Goulon, A. Retournard, P. Friant, C. Goulon-Ginet, C. Berthe, J. Muller, J. Poncet, R. Guilard, J. Escalier and B. Neff. Structural Characterization by X-Ray Absorption Spectroscopy (EXAFS/XANES) of the Vanadium Chemical Environment in Boscan Asphaltenes. *J. Chem. Soc. Dalton* (1984), (6), pp. 1095-1103.

[19]   G.P. Dechaine and M.R. Gray. Chemistry and Association of Vanadium Compounds in Heavy Oil and Bitumen, and Implications for their Selective Removal. *Energy Fuels* (2010), **24**(5), pp. 2795-2808.

[20]   J.G. Reynolds and W.R. Biggs. Application of Size Exclusion Chromatography Coupled with Element-Specific Detection to the Study of Heavy Crude Oil and Residua Processing. *Acc. Chem. Res.* (1988), **21**(9), pp. 319-326.

[21]   J.G. Reynolds, E.J. Gallegos, R.H. Fish and J.J. Komlenic. Characterization of the Binding Sites of Vanadium Compounds in Heavy Crude Petroleum Extracts by Electron Paramagnetic Resonance Spectroscopy. *Energy Fuels* (1987), **1**(1), pp. 36-44.

[22]   *Sakura: A Tool to Pre-Process XAS Data*, http://archive.synchrotron.org.au/index.php/aussyncbeamlines/x-ray-absorption-spectroscopy/sakura [March 2019]

[23]   B. Ravel and M. Newville. Athena, Artemis, Hephaestus: Data Analysis for X-ray Absorption Spectroscopy using IFEFFIT. *J. Synchrotron Rad.* (2005), **12**(4), pp. 537-541.

[24]   S. Graulis, D. Chateigner, R.T. Downs, A.F.T. Yokochi, M. Quirós, L. Lutterotti, E. Manakova, J. Butkus, P. Moeck and A. Le Bail. Crystallography Open Database - An Open-Access Collection of Crystal Structures. *J. Appl. Crystallogr.* (2009), **42**(4), pp. 726-729.

[25]   G. Jahrsengene, H.C. Wells, C. Sommerseth, A.P. Ratvik, L.P. Lossius, R.G. Haverkamp and A.M. Svensson. Vanadium Speciation in Petroleum Cokes for Anodes used in Aluminium Electrolysis. *TRAVAUX - Proceedings for the ICSOBA Conference* (2017), **46**, pp. 617-624.

[26]   M.A. Duchesne, J. Nakano, Y. Hu, A. MacLennan, R.W. Hughes, J. Bennett and A. Nakano. Vanadium Oxidation State Determination by X-Ray Absorption Spectroscopy. *Advances in Molten Slags, Fluxes, and Salts: Proceedings of the 10th International Conference on Molten Slags, Fluxes and Salts* (2016), pp. 1405-1412.

[27]   B.M. Rytting, I.D. Singh, P.K. Kilpatrick, M.R. Harper, A.S. Mennito and Y. Zhang. Ultrahigh-Purity Vanadyl Petroporphyrins. *Energy Fuels* (2018), **32**(5), pp. 5711-5724.

[28]   G. Liu, X. Xu and J. Gao. Study on the Deferrization and Desalting for Crude Oils. *Energy Fuels* (2004), **18**(4), pp. 918-923.

[29]   J.T. Miller and R.B. Fisher. Structural Determination by XAFS Spectroscopy of Non-Porphyrin Nickel and Vanadium in Maya Residuum, Hydrocracked Residuum, and Toluene-Insoluble Solid. *Energy Fuels* (1999), **13**(3), pp. 719-727.

[30]   J.A. Nesbitt and M.B.J. Lindsay. Vanadium Geochemistry of Oil Sands Fluid Petroleum Coke. *Environ. Sci. Technol.* (2017), **51**(5), pp. 3102-3109.

[31]   J.A. Nesbitt, J.M. Robertson, L.A. Swerhone and M.B.J. Lindsay. Nickel Geochemistry of Oil Sands Fluid Petroleum Coke Deposits, Alberta, Canada. *FACETS* (2018), **3**(1), pp. 469-486.

[32]   J.A. Nesbitt, M.B.J. Lindsay and N. Chen. Geochemical Characteristics of Oil Sands Fluid Petroleum coke. *Appl. Geochem.* (2017), **76**, pp. 148-158.

[33]   Z.J. Zhou, Q.J. Hu, X. Liu, G.S. Yu and F.C. Wang. Effect of Iron Species and Calcium Hydroxide on High-Sulfur Petroleum Coke CO_2 Gasification. *Energy Fuels* (2012), **26**(3), pp. 1489-1495.

[34]   J.G. Rolle and Y.K. Hoang. Studies of the Impact of Vanadium and Sodium on the Air Reactivity of Coke and Anodes. *Light Met.* (1995), **1995**, pp.

[35]   L. Ren, R. Wei and Y. Gao. Co-gasification reactivity of petcoke and coal at high temperature. *Fuel* (2017), **190**, pp. 245-252.

Supplemental Material File for: An EXAFS and XANES Study of V, Ni and Fe Speciation in Cokes for Anodes Used in Aluminum Production

Gøril Jahrsengene[1], Hannah C. Wells[2], Camilla Sommerseth[3], Arne Petter Ratvik[3], Lorentz Petter Lossius[4], Katie H. Sizeland[5], Peter Kappen[6], Ann Mari Svensson[1] and Richard G. Haverkamp[2]

[1]Department of Material Science and Engineering, Norwegian University of Science and Technology (NTNU), Trondheim, Norway
[2]School of Engineering and Advanced Technology, Massey University, Palmerston North, New Zealand
[3]SINTEF Industry, Trondheim, Norway
[4]Hydro Aluminium AS, Primary Metal Technology, Årdal, Norway
[5]ANSTO, Lucas Heights, New South Wales, Australia
[6]Australian Synchrotron, ANSTO, Clayton, Victoria, Australia

Corresponding author Richard Haverkamp: r.haverkamp@massey.ac.nz

1. XAS data

The following graphs and tables include X-ray absorption spectroscopy (XAS) spectra and fitting of X-ray absorption near edge structure (XANES) and extended X-ray absorption fine structure (EXAFS) data for six cokes (A-F). Details on the experimental method and coke specifics (as described in the main paper) is added in section 2 for clarification.

1.1 Ni XANES
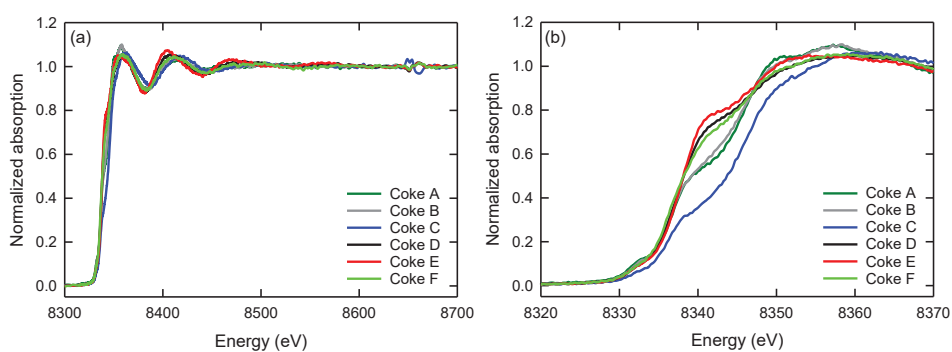
Fig. S-1 – The normalized absorption nickel K-edge XANES spectra for industrial cokes A-F. (*a*) Whole energy region; (*b*) edge region covering 50 eV.

Table S-I. Linear combination fits (LCF) of Ni K-edge reference spectra to coke samples.

Coke	Fraction Ni_3S_2	Fraction nickel porphyrin	Reduced χ^2 for fit	R-factor
A	0.41	0.59	0.0014	0.009
	1	-	0.0077	0.045
B	0.46	0.54	0.0012	0.007
	1	-	0.0063	0.036
C	0.24	0.76	0.0120	0.079
	1	-	0.0230	0.150
D	0.69	0.31	0.0016	0.009
	1	-	0.0033	0.019
E	0.71	0.29	0.0018	0.011
	1	-	0.0034	0.021
F	0.66	0.34	0.0012	0.007
	1	-	0.0032	0.018

1.2 Ni EXAFS

Table S-II. EXAFS model fits to Ni K-edge data from cokes.

| Coke	Compound (COD ID) Space group (crystal system)	R-factor	S_0^2	ΔE_0	ΔR	σ^2	Paths included
D	NiS (1010435) P 6_3 / m m c (Hexagonal)	0.042	1.23	0.90	-0.10	0.025	All paths < 5.00 Å
		0.014	1.08	0.08	-0.10	0.022	All paths < 4.10 Å
	NiS (1011038) R 3 m n (Trigonal)	0.030	1.39	0.44	-0.04	0.021	All paths < 4.00 Å
	Ni_3S_2 (1011250) R 3 2 (Trigonal)	0.057	2.56	2.81	0.07	0.030	All paths < 4.02 Å
	NiS_2 (1544738) P a -3 (Cubic)	0.057	1.02	1.71	-0.12	0.020	All paths < 4.20 Å
	NiO (1010093) F m -3 m (Cubic)	0.513	-1.50	0.50	0.16	0.036	All paths < 4.20 Å
	Ni_3C (1528750) R -3 c (Trigonal)	0.024	2.71	-29.15	-0.24	0.032	All paths < 3.80 Å
	Ni (9013024) F m -3 m (Cubic)	0.119	-4.47	-3.70	-0.14	0.050	All paths < 5.00 Å
E	NiS (1010435) P 6_3 / m m c (Hexagonal)	0.038	1.10	-0.33	-0.06	0.020	All paths < 4.10 Å
	NiS_2 (1544738) P a -3 (Cubic)	0.123	1.18	2.56	-0.06	0.021	All paths < 4.20 Å
		0.017	1.03	0.73	-0.08	0.017	All paths < 4.20 Å excluding Ni-Ni
F	NiS (1010435) P 6_3 / m m c (Hexagonal)	0.020	0.82	-3.32	-0.18	0.020	All paths < 4.10 Å
	NiS_2 (1544738) P a -3 (Cubic)	0.105	0.89	-0.24	-0.18	0.021	All paths < 4.20 Å

1.3 V XANES
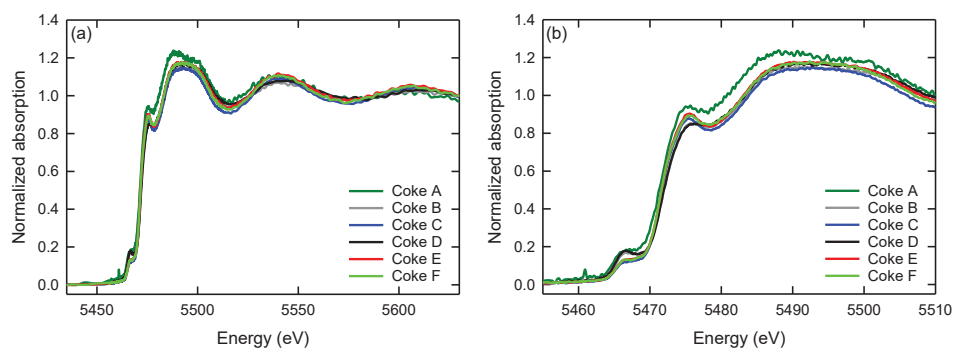
Fig. S-2 – The normalized absorption vanadium K-edge XANES spectra for industrial cokes A-F. (*a*) Whole energy region; (*b*) edge region.

1.4 V EXAFS

Table S-III. EXAFS model fits to V K-edge data from coke D.

Coke	Compound (COD ID) Space group (crystal system)	R-factor	S_0^2	ΔE_0	ΔR	σ^2	Paths included
	V_3S_4 (2001606) P 6_3 / m (Hexagonal)	0.045	0.51	-3.61	-0.09	0.003	All paths < 4.11 Å
	V_3S_4 (1537894) C 1 2 / m 1 (Monoclinic)	0.239	0.74	-7.60	-0.14	0.012	All paths < 4.00 Å
	VS (1010579) P 6_3 / m m c (Hexagonal)	0.260	0.77	-3.35	-0.09	0.018	All paths < 4.20 Å
D	V_2O_3 (1537656) R -3 c (Trigonal)	0.466	0.432	15.68	0.19	0.011	All paths < 3.41 Å
	VC (1011321) F m- 3 m (Cubic)	0.111	0.69	-32.53	-0.56	0.016	All paths ≤ 4.30 Å excluding forward, rattle, dogleg and triple scattering paths.
	V (9012770) I m -3 m (Cubic)	0.351	-1.05	-7.06	-0.17	0.025	All paths < 5.00 Å
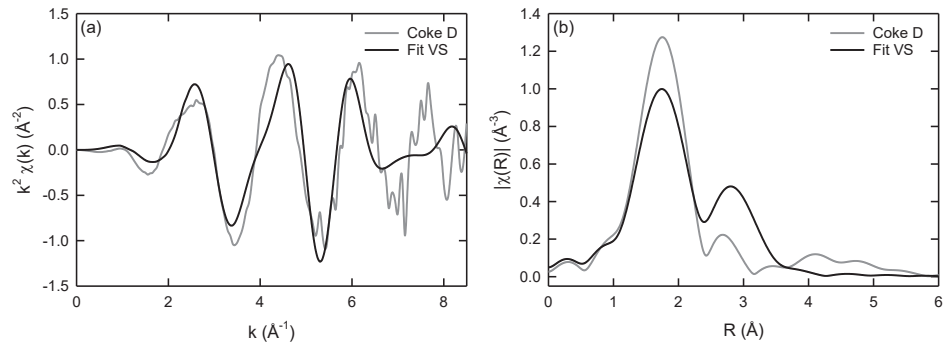
Fig. S-3 – The experimental EXAFS spectrum for coke D and the FEFF theoretical fit for VS in (*a*) k-space and (*b*) R-space.
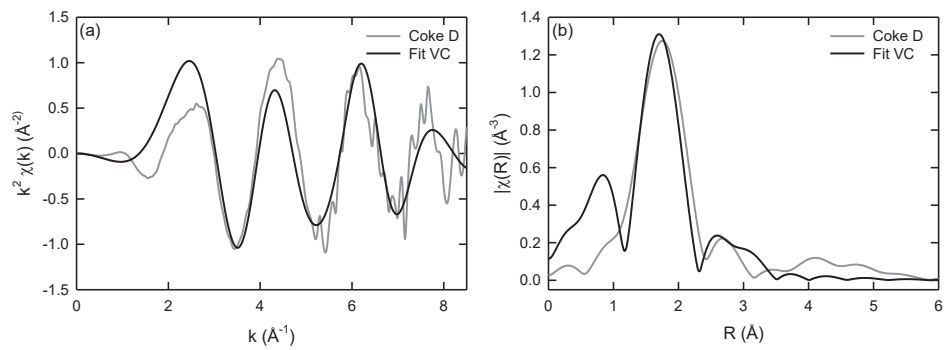
Fig. S-4 – The experimental EXAFS spectrum for coke D and the FEFF theoretical fit for V_2O_3 in (*a*) k-space and (*b*) R-space.
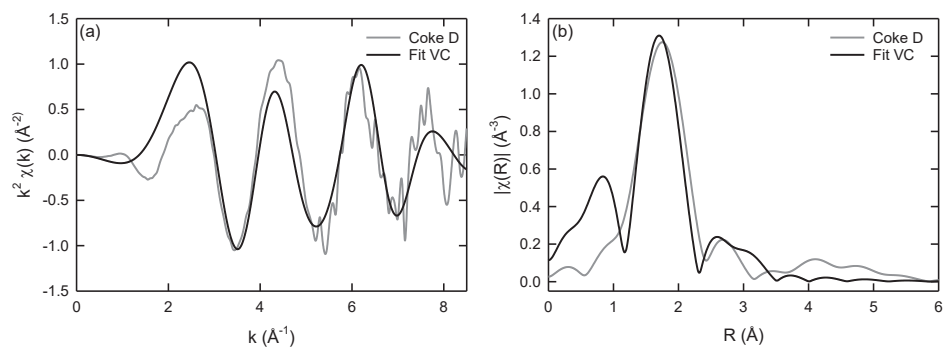
Fig. S-5 – The experimental EXAFS spectrum for coke D and the FEFF theoretical fit for VC in (*a*) k-space and (*b*) R-space.

Table S-IV. EXAFS model fits hexagonal V_3S_4 to V K-edge data from cokes. All paths < 4.11 Å, k from 2 to 8.5 $Å^{-1}$

| Coke	R-factor	S_0^2	ΔE_0	ΔR	σ^2
A	0.089	0.74	-2.03	-0.04	0.009
B	0.048	0.50	-4.05	-0.08	0.003
C	0.040	0.53	-2.02	-0.05	-0.003
D	0.045	0.51	-3.61	-0.09	0.003
E	0.034	0.58	-1.55	-0.04	-0.001
F	0.029	0.59	-1.65	-0.04	-0.001

1.5 Fe XANES
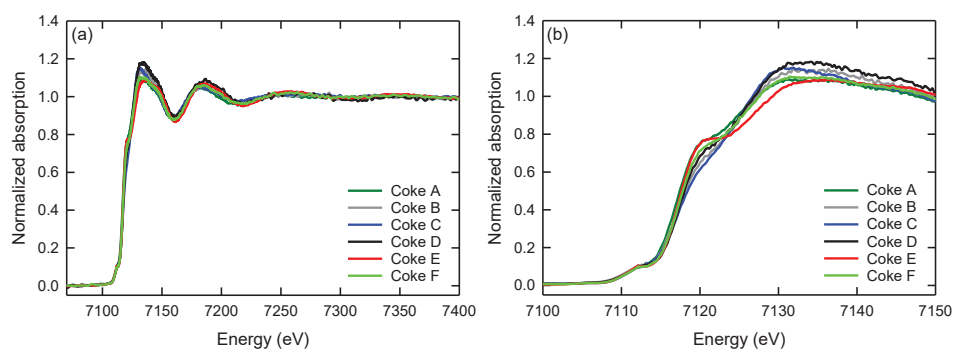
Fig. S-6 – The normalized absorption iron K-edge XANES spectra for industrial cokes A-F. (*a*) Whole energy region; (*b*) edge region.

Table S-V. Linear combination fits of Fe K-edge reference spectra to coke samples.

Coke	Iron porphyrin	FeS	FeS$_2$	Reduced χ^2 for fit	R-factor
A	0.14	0.56	0.30	0.0015	0.018
B	0.31	0.46	0.23	0.0012	0.013
	0.37	0.56	0.07	0.0011	0.012
C	0.37	0.63	-	0.0012	0.012
	0.39	-	0.61	0.0023	0.024
C*	0.34	0.35	0.31	0.0002	0.137
D**	0.34	0.43	0.23	0.0035	0.034
	0.14	0.22	0.64	0.0011	0.013
E	0.18	0.82	-	0.0025	0.030
	0.15	-	0.85	0.0013	0.015
E*	0.13	0.17	0.70	0.0003	0.142
F	0.22	0.42	0.36	0.0013	0.014

* LCF based on derivative spectrum, Red χ^2 value not comparable to the others.
**Coke D poorer fit caused by low Fe content.

1.6 Fe EXAFS

Table S-VI. EXAFS model fits to Fe K-edge data from cokes.

Coke	Compound (COD ID) Space group (crystal system)	R-factor	S_0^2	ΔE_0	ΔR	σ^2	Paths included
C	FeS (1009043) P -6 2 c (Hexagonal)	0.081	1.32	-1.33	-0.15	0.023	All paths < 4.30 Å excluding Fe-Fe and S-Fe-Fe
	FeS$_2$ (1011013) P n n m (Orthorhombic)	0.052	1.58	-5.27	0.04	0.031	All paths < 4.03 Å excluding Fe-Fe and S-Fe-Fe
	FeS$_2$ (1544891) P a -3 (Cubic)	0.047	2.00	-7.81	-0.01	0.034	Single and double scattering paths < 4.50 Å excluding Fe-Fe and S-Fe-Fe
E	FeS (1009043) P -6 2 c (Hexagonal)	0.029	0.78	1.20	-0.17	0.003	All paths < 4.30 Å excluding Fe-Fe and S-Fe-Fe
	FeS$_2$ (1011013) P n n m (Orthorhombic)	0.048	0.90	-0.02	0.05	0.012	All paths < 4.03 Å excluding Fe-Fe and S-Fe-Fe
	FeS$_2$ (1544891) P a -3 (Cubic)	0.046	0.98	-2.95	-0.01	0.013	Single and double scattering paths < 4.50 Å excluding Fe-Fe and S-Fe-Fe

	FeS (1009043)					All paths
	P -6 2 c (Hexagonal)	0.033	0.92	0.20	-0.15	0.010	< 4.30 Å excluding Fe-Fe and S-Fe-Fe
	FeS$_2$ (1011013)						All paths
	P n n m (Orthorhombic)	0.038	1.13	-1.89	0.05	0.020	< 4.03 Å excluding Fe-Fe and S-Fe-Fe
F	FeS$_2$ (1544891) P a -3 (Cubic)	0.040	1.32	-5.00	-0.01	0.022	Single and double scattering paths < 4.5 Å excluding Fe-Fe and S-Fe-Fe
	FeO (1011198) F m -3 m (Cubic)	0.430	-5.21	-3.40	0.14	0.063	All paths < 3.70 Å
	Fe$_3$C (1008725) P n m a (Orthorhombic)	0.055	2.69	-27.63	-0.13	0.028	All paths < 3.37 Å
	Fe (9013463) I m -3 m (Cubic)	0.365	-23.29	4.02	0.07	0.081	All paths < 5.00 Å

2. Experimental Design, Materials, and Methods

Table S-VII. Concentration of S, V, Ni and Fe in the six cokes. Sulfur (S) and metal content were measured on coke material using XRF.

Coke	S (mass%)	V (ppm)	Ni (ppm)	Fe (ppm)
A	1.42	116	192	178
B	3.56	402	210	264
C	5.54	432	192	316
D	3.86	714	426	156
E	4.42	624	323	464
F	4.76	541	234	724

XAS spectra were recorded around the K-edges of Fe, Ni and V at room temperature of the six CPCs and a variation of reference samples. Cokes were ground finely and investigated without dilution. Reference materials were diluted with cellulose powder.

X-ray absorption spectra were recorded on the XAS beamline at the Australian Synchrotron, Victoria, Australia. The beamline controls the energy by using a fixed exit Si(111) double crystal monochromator and conditions the beam using a collimating mirror (Si) and a toroidal focusing mirror (Rh coated). The mirrors were also used to reject the higher harmonics together with a flat harmonic rejection mirror (SiO_2). A 100 element Ge pixel array fluorescence detector were used to record the spectra, and beamsize on the sample was approximately 1 x 1.5 mm. A calibration of the energy scale was done by simultaneously measuring a metal foil (V, Ni or Fe) placed between two downstream ion chambers.

By varying the energy steps, the data collected was suitable for both XANES and EXAFS analysis. A constant dwell time of 1 s at each step was used. Pre-edge data was collected at 0.003 eV energy intervals, and at around the edge at 0.00025 eV intervals. Above the XANES region steps of $k = 0.07$ $Å^{-1}$ was used up to $k = 10$ $Å^{-1}$ above the edge, where the collection terminated.

The spectra was normalised with step-edge equal to 1, with removal of possible glitches as high energies. Further analysation was done on the resulting Ni-spectra, and the averaged spectra of two or three runs for V and Fe.

The XANES region was used for linear combination fitting (LCF) on normalized $\mu(E)$ and derivative and was performed with Athena software [1]. The X-ray edge position, E_0, was held to be the same for all components. Athena use non-linear least squares minimization fitting and it was carried out over an energy range 20 eV below E_0 to 50 eV above E_0. The final LCF's used a combination of the most promising reference compounds.

The EXAFS analysation for V, Ni and Fe in the cokes were done using Artemis software [1] and fitted to crystal data from the Crystallographic Open Database [2]. The resulting fits are fitted in R (with k^2), and the fit was terminated around 8-8.5 Å^{-1}. The goodness of the fit was evaluated by the EXAFS R-factor (as low as possible), visual inspection, and the unrestricted fitting values S_0^2, ΔE_0, ΔR and σ^2. S_0^2 was evaluated as good in the range 0.5-1 and $\Delta E_0 < 5$ eV, while ΔR and σ^2 were around 0 for all fits.

References

1.   B. Ravel and M. Newville, *J. Synchrotron Rad.* 2005, vol. 12, pp. 537-541.
2.   S. Gražulis, D. Chateigner, R. T. Downs, A. F. T. Yokochi, M. Quirós, L. Lutterotti, E. Manakova, J. Butkus, P. Moeck and A. Le Bail, *J. Appl. Crystallogr.* 2009, vol. 42, pp. 726-729.

Chapter 7 Electrochemical Characterisation of Anodes for the Aluminium Industry made from Cokes with Variable Impurity Content

Gøril Jahrsengene[1], Arne Petter Ratvik[2], Lorentz Petter Lossius[3], Ann Mari Svensson[1]

[1]Department of Materials Science and Engineering, NTNU Norwegian University of Science and Technology, Trondheim, Norway
[2]SINTEF Industry, Trondheim, Norway
[3]Hydro Aluminium AS, Primary Metal Technology, Årdal, Norway

Abstract

The aluminium industry is concerned by the predicted quality changes in available petroleum cokes used for the prebaked carbon anodes. Any changes for the production related to using higher sulfur cokes in anode blends needs to be evaluated. These lower quality cokes will, naturally, produce more SO_2, which needs to be handled by the smelters, and result in a more impure product as a result of more metal impurities in the anodes. The knowledge on effects of the high-sulfur cokes on the electrochemical reactivity is, however, limited. In this study, the electrochemical performance of pilot anodes made from five industrial cokes, ranging from 1.42 to 5.54 wt% S is studied, in order to determine if the use of lower quality cokes will influence the electrochemical reactivity. Electrochemical performance implies the assessment of overpotential and electrochemical impedance at a given current density in a set-up where bubble formation is minimized, as well as studies of voltage oscillations related to bubble formation on horizontal anodes. The cokes with an anisotropic structure are very similar with respect to electrochemical performance, except for the anode made from the purest coke, which exhibit lower voltage oscillations due to bubbles. This anode also has a slightly higher permeability compared to the others. The isotropic anode has lower charge transfer resistance, higher double layer capacitance and lower voltage amplitude related to bubbles compared to most anisotropic anodes. The

difference is attributed to a combination of coke properties and anode properties, as some of the positive effects observed for the more permeable isotropic anode were also observed for anisotropic anodes with high permeability and high surface roughness.

7.1 Introduction

During aluminium production, alumina (Al_2O_3) dissolved in cryolite reacts electrochemically with carbon in the prebaked carbon anode, producing aluminium and CO_2 [1]. Constant current is applied, and the cell voltage is about 4 V. A significant fraction of the irreversible voltage losses are associated with the anode. The main contributions include the anode overpotential, resistance increase because of produced gas bubbles, and resistance of the anode material itself [2]. The prebaked anodes consist of calcined petroleum coke (CPC), coal tar pitch binder and recycled anode butts, and the quality of the available coke is assumed to affect the irreversible losses at the anode. Understanding and decreasing the cell voltage is important, and the large variation in anode material make these investigations important when searching to improve the overall process and reducing the cost.

There is a large variation of CPCs used in aluminium production, most anodes have a mix of several types of coke material to reach the specifications set by the smelter [3, 4]. In baked anodes it is important to control the levels of impurities, chemical reactivity, density, electrical conductivity and strength. Anode grade coke (often referred to as sponge coke) have traditionally been characterised by low sulfur and metal content, a mixed optical structure, and an open porosity permitting good pitch penetration. The availability of regular anode coke is not following the high demand from the aluminium industry, so higher sulfur cokes are increasingly used in the anodes. This is usually accompanied by higher metal impurity levels in the cokes as well. In addition, to meet the high demand, the use of fuel grade cokes (typically spherical, dense and isotropic particles) has been introduced as well [5, 6]. Today, anodes are typically produced from blends of sponge cokes with relatively high variations in sulfur, while holding the anode sulfur level relatively constant.

By using higher sulfur cokes, eventually the total sulfur levels in the anodes are predicted to rise as well. Increased emissions of SO_2 due to utilisation of higher sulfur cokes can be remedied by wet scrubbing (seawater or caustic scrubbing dependent on location of the plant) the pot room gases; the regular Gas Treatment

Centre (GCT) has a low efficiency for sulfur scrubbing [7]. Sulfur seems to have the positive effect of reducing the reactivity of the carbon towards the produced CO_2 [8-10], and is for this reason beneficial at reasonable levels in the anodes. Sulfur can also be removed directly from the coke by desulfurisation, *i.e.* high temperature calcination, but this introduces unwanted microporosity in the coke material, bulk density is reduced, and the air reactivity of the material increases [11, 12].

The metal impurities seem to catalyse the unwanted reactions between anode, air and CO_2 [13, 14], and needs to be controlled or minimised to reduce reactivity and contamination of the primary aluminium. Isotropic cokes, with its very different structure, have significantly higher thermal expansion than the regular anode cokes. To avoid cracking of the anode, the potential for blending isotropic and anisotropic coke is limited. The maximum value of isotropic coke is believed to be in the 20 - 30 % range [6, 15, 16].

A proposed mechanism of the electrochemical reactions on the anode is given in Equations 7.1-7.2 [17]. The details of the reactions occurring at the anode is not fully agreed upon, especially as the exact composition of the oxyfluoraluminate compound is disputed. The mechanism is assumed to be a sequence of reactions that include formation of an oxyfluoraluminate ion followed by electrochemical oxidation of this specie by charge transfer reactions with an adsorbed intermediate specie, CO_{ads} [17-19].

$$Al_2O_2F_6^{4-} + C \rightarrow Al_2OF_6^{2-} + CO_{ads} + 2e^- \qquad (7.1)$$

$$Al_2O_2F_6^{4-} + CO_{ads} \rightarrow Al_2OF_6^{2-} + CO_2 + 2e^- \qquad (7.2)$$
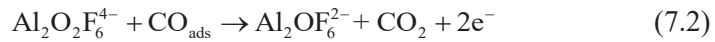
The anodic potential consists of several components, several of which are also dynamically influenced by bubble evolution on the surface. Equation 7.3 shows the components of the measured anode potential [1, 20, 21]. In this reaction, the reversible potential E^{rev} refers to the CO_2 formation reaction and may be assumed to be independent of material properties. The concentration overpotential, η_c, is considered negligible in saturated melts, as well as being very small in industrial cells [22]. The reaction overpotential is associated with the charge transfer reactions and consists of two contributions. The first is η_r', the reaction overpotential when the surface is free of bubbles, and the second part η_h, often called hyperpolarisation, which represents the increased overpotential due to locally higher current density from partial screening of the anode surface by bubbles. The $I(R_s' + \delta R_s)$ is the term related to the electrical resistance in the system with a current I flowing through the cell, where the R_s' part is the series resistance

with no bubbles screening the surface and the δR_s part is the increase due to bubbles blocking the anode surface.

$$E_{\text{anode measured}} = E^{\text{rev}} + \eta_c + \eta_r{'} + \eta_h + I(R_s{'} + \delta R_s) \qquad (7.3)$$

In laboratory studies the different contributions can be investigated separately by suitably adapting the anode assembly. Using a vertical anode assembly [20, 23, 24] will minimise the bubble screening of the surface, and the reaction overpotential can be investigated without the effect of hyperpolarisation. A horizontal anode assembly [21, 25] will maximise the bubble formation, and can be used to investigate the effect of hyperpolarisation. Hyperpolarisation has also been investigated with a rotating disk [26]. Graphite is frequently used as a reference material, as it may be assumed to be homogenous, constant quality and give reproducible results.

Bubbles are likely to nucleate according to type IV model by Jones, Evans and Galvin [27] at preferential positions on the anode surface. These positions are pores, which will be filled with gas, and when the bubble reaches a certain size, dependent on the pore size, it detaches and start moving along the anode surface. A new bubble immediately starts to nucleate in the gas cavity, while the detached bubbles continue to grow by coalescence [28, 29]. The large bubble will cover the anode with a coverage factor θ, and form a bubble sheet with thickness d_b. When the bubble reaches the side, it will escape the anode. Size and number of pores will therefore affect the bubble behaviour and growth. It has been shown by modelling that the mean pore diameter is important; Einarsrud concluded that smaller pores will result in higher voltage amplitudes, faster bubble release frequency and larger screening of the anode [29]. This has been observed experimentally as well, for example by monitoring the voltage, using see-through cells and cameras [30-33]. Some other important factors are the geometry of the anode, microstructure and wetting properties, anode-cathode distance, bath composition, electrical conductivity and the magnetic field motion.

Regarding voltage fluctuations associated with bubble formation, it has been shown that for sufficiently small anodes used for laboratory scale experiments, the behaviour of the bubbles will result in a quasi-periodical dynamic pattern of voltage oscillations [34, 35]. The length the bubble needs to travel is short in the laboratory scale experiments, different from the large industrial anodes where several bubbles can form at the same time affecting the voltage response [33]. Laboratory experiments can therefore not easily be compared to each other, if the geometry is different, or directly to the industrial case, but the bubbles formed

during laboratory scale experiments may provide useful information on what happens locally on the industrial anodes [33]. In industrial anodes, slots are used to facilitate faster removal of bubbles formed under the anodes, proven to be an efficient way to decrease the hyperpolarisation.

The screening of the anodes by the formed bubble layer has been reported to vary depending on the geometry, current density and material. For lab scale experiments, 45 % has been reported by Aaberg *et al.* [36] and values in the 50-90 % range by Zhao *et al.* [32], who also showed the improvement when introducing slots. Anisotropic cokes were shown to have values around 40 % by Thorne *et al.* [21] and Sommerseth [16], and for isotropic cokes a lower value around 20 %. This corresponded to a reduction of the voltage caused by bubbles of almost 0.2 V, and the frequency of the voltage oscillations was also lower for the isotropic anodes. Increasing the current density is reported to increase the frequency of bubble release and increase the voltage oscillation amplitude [21, 37]. Wetting is also assumed to be affecting the voltage oscillation, as *i.e.* a low liquid-solid wetting angle will result in smaller screening [31]. Polarisation improve the wettability of the carbon anode, more so for isotropic anodes than anisotropic anodes [16, 38]. In these works, anodes containing isotropic coke was shown to have lower voltage oscillations on horizontal, lab-scale electrodes, attributed to the improved wetting.

The double layer capacitance, C_{dl}, is a measure of surface's ability to store electric charge by polarisation, and the area that is electroactive and wetted by the melt should be proportional to C_{dl}. This value can be extracted, *e.g.* by electrochemical impedance spectroscopy (EIS) [17, 39, 40]. Typical values reported for C_{dl} in laboratory experiments on graphite include 15-100 $\mu F/cm^2$ in the 0.03-0.05 A/cm^2 range, while values for baked industrial anodes are typically reported larger, in the 100-350 $\mu F/cm^2$ range [17, 41]. Lower values for baked anodes was reported by Gebarowski *et al.* [23], in the range 60-80 $\mu F/cm^2$. Anodes made of isotropic cokes have been shown to have larger C_{dl} than anisotropic cokes [23, 38], likely corresponding to the better wetting between anode and electrolyte and thus a larger electroactive area. The scatter of reported C_{dl} values is likely the effect of material type, homogeneity of samples and pre-treatment of the anode surface [42].

Although the production parameters, surface roughness and open porosity of the anodes are of great importance and likely a factor on the electrochemical behaviour of the anodes, it is important not to disregard the effect of the coke itself, especially keeping in mind the large variation of coke quality. The

properties of coke that can influence the electrochemical reactivity in the industrial anode is not well documented, varying results are found in literature and not all can be directly applied to the industrial anodes. Most has been focused on impurities, investigating doped carbon materials (an overview of some is given in [14]). Investigations have been done on graphite, having significantly higher overpotential than regular coke anodes [41], blended anodes as used in the industry [39], and pilot anodes made from single source cokes [20]. A decrease in overpotential using isotropic cokes rather than regular anisotropic anode coke was observed by Thorne *et al*. [20, 24], also correlating with the double layer capacitance, C_{dl} [23, 38]. This was further suggested to correlate with the microstructural properties (edge sites, surface chemistry and isotropy was evaluated) rather than surface roughness and open porosity. The laboratory study by Pietrzyk and Thonstad [43] focused on the effect of sulfur on carbon consumption and current efficiency. They found no large differences in consumption, dusting or degree of Boudouard reaction going from 2 to 3.8 % sulfur, but a lower current efficiency was observed with increasing sulfur.

In this work the electrochemical behaviour of pilot anodes made of single source industrial cokes of varying sulfur and metal content was investigated. The five cokes have previously been investigated with respect to sulfur, vanadium, nickel and iron speciation using X-ray absorption spectroscopy (XAS) techniques (Chapter 4 and 6) and evaluated with respect to reactivity and microstructure (Chapter 5). The cokes were chosen mainly because of the S-V relationship, as described in [44]. The goal was to investigate whether the differences in levels of impurities, in particular the differences observed with respect to level and speciation of sulfur in the cokes, also influence the electrochemical reactivity and behaviour, while also keeping in mind the anode properties (like surface roughness). The anodes were investigated with respect to voltage oscillations caused by bubble formation, and reaction overpotential. In addition, electrochemical impedance spectroscopy was used as a complementary technique to assess electrochemical reactivity in terms of charge transfer resistance. Furthermore, impedance spectra were used to extract information about the electrochemically active area (C_{dl}), as well as the inductive behaviour related to the adsorbed intermediate step (Equation 7.2).

7.2 Experimental

7.2.1 Materials and Anode Assembly

The coke material and resulting anodes are labelled A-E in accordance with specifications in Table 7.1 and Table 7.2, the same label names as in other published works regarding cokes by Jahrsengene *et al.* [44-46]. The cokes A, B and C are also the same as used in the work by Gebarowski *et al.* [25] (Coke 1=A, Coke 2=C, Coke 3=B), where the small fraction anodes are from the same pilot anode as this study, and the large fraction anode (0-6 mm) are made from the same cokes. Graphite is used as reference material.

Pilot scale anodes were produced in-house by Hydro Aluminium. The metal and sulfur content of the cokes are given in Table 7.1. The aggregate size was 0-2 mm, where the small size was chosen to ensure a surface as homogenous as possible for the small-scale laboratory anodes. The pitch used had a Mettler softening point of 125 °C. The composition was held relatively similar for all pilot anodes and is given in Table 7.2, the exception being the lower pitch content of anode E. Mixing and baking temperatures were the same for all anodes, 200 °C and 1275 °E respectively (see [47] for details on the equivalent baking temperature °E).

Table 7.1: Coke composition. M includes Na, Mg, Al, Si, Ca, V, Fe, and Ni.

Coke type	S (wt%)	V (ppm)	M (ppm)
A	1.42	116	761
B	3.56	402	1323
C	5.54	432	1356
D	3.82	714	1668
E	4.42	624	2009

Table 7.2: Pilot anode composition.

Coke type / Anode name	1-2 mm aggregate (wt%)	0-1 mm aggregate (wt%)	Ball mill product < 64 μm (wt%)	Pitch content (wt%)
A	39.5	15.9	44.6	14.5
B	40.8	13.7	45.5	14.6
C	38.0	15.8	46.2	14.2
D	37.5	16.6	45.9	13.8
E	37.7	19.2	43.1	11.7

10 mm core samples were drilled from the pilot anodes. Three different anode assemblies were used; unshielded anodes, horizontal assembly and vertical assembly, shown in Figure 7.1. The horizontal and vertical assembly gave well defined areas for the reactions to be studied; 0.76 cm^2 for the horizontal surface and 1.53 cm^2 for the vertical surface. Boron nitride was used as shield. A graphite rod in the middle of the vertical assembly was needed to obtain electrical contact with the anode.
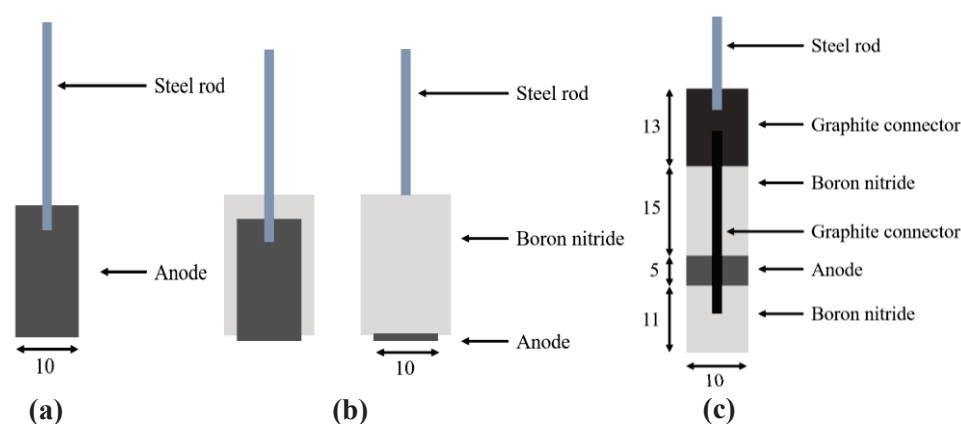
Figure 7.1: The cross-section of the three types of anode assemblies for electrochemical investigations. **(a)** Unshielded anode, **(b)** horizontal assembly (left: cross section; right: outside view) and **(c)** vertical assembly. All numbers in the figure are in mm.

7.2.2 Physical Analysis

The pilot anodes were characterised using International Organization for Standardization (ISO) methods. Density (ISO-12985-1:2000), specific electrical resistivity (SER) (ISO 11713:2000) and permeability (in-house Hydro method similar to ISO 15906:2007) was measured for all anodes. A single anode of each coke type, with 0-6 mm fraction coke particles, were analysed by X-ray fluorescence (XRF) (ISO 12980:2000) to determine the levels of sulfur and metal impurities in the anode. This specific pilot anode was not analysed further in this work, but the impurity levels are assumed similar in the 0-2 mm anode as the pitch content was close to identical in the two cases. These measurements are routine measurements done by Hydro Aluminium.

7.2.3 Surface Characterisation

Surface topography was analysed using an Infinite Focus confocal microscope from Alicona. The method consists of scanning the area of interest by taking pictures over a certain height range, and then construct a 3D image of the surface. The vertical resolution was 100 nm. The surface roughness, including pits and other topography, was defined as the ratio between true and projected area (TA/PA). The analysis was performed on several anodes as prepared before electrochemical testing to get an overview of the roughness and roughness variation between samples. The technique was also applied on the unshielded anodes before and after electrolysis, to investigate local consumption of the anode. These samples were ground to P#2000 using SiC paper before the electrochemical analysis, to facilitate identification of specific grains. After electrolysis the remaining electrolyte was removed by soaking in warm, saturated $AlCl_3$ solution before imaging.

7.2.4 Electrochemical Measurements

All electrochemical experiments used the same closed furnace set up, shown in Figure 7.2 with the vertical anode assembly as an example. The Si_3N_4 shielding in the bottom was not used for the horizontal and unshielded samples. For the unshielded setup, the bottom of the anode was approximately 0.5 cm from the top of the electrolyte. For the horizontal set up it was 1 cm from the top of the electrolyte, and for the vertical setup there was 1 cm from the bottom of the exposed surface to the top of the electrolyte. The reference electrode was an in-house produced aluminium electrode, (see appendix A in the thesis of Sommerseth [16]) which measured and controlled the potential between anode test electrode and the reference; the graphite crucible acted as the counter electrode. The electrolyte was the same in all experiments, a cryolite melt with cryolite ratio CR = 2.3 saturated in aluminium oxide. Synthetic cryolite (≥ 97 %, Sigma Aldrich), an excess of 9.8 wt% AlF_3 (industrial grade, sublimed in-house), 9.4 wt% Al_2O_3 (99.4 %, Merck) and 4 wt% CaF_2 (≥ 97 %, Merck) was mixed. The experiments were performed in an argon atmosphere at 1000 °C.
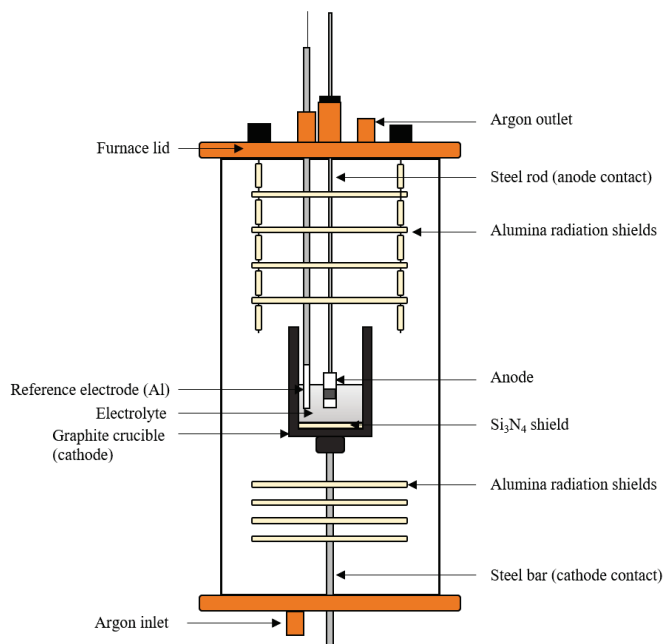
Figure 7.2: Electrochemical experimental setup for vertical anodes.

Two potentiostats were used for the electrochemical measurements. A Parstat 4000+ from Princeton Applied Research was used with a Bipolar Operational Power supply (amplifier) from Kepco for the horizontal and unshielded anode experiments. A Zahner IM6eX from Zahner-Elektrik (± 2 A/4 V) was used for the vertical anode assembly.

The unshielded anodes were kept at constant current of approximately 1 A/cm^2 (small variations were possible due to variations in the exposed surface area) for 40 minutes, resulting in wear of approximately 0.5 mm and consumption of 0.18 g carbon. These samples were hot-pulled (current still on when extracted from the bath) to reduce the amount of electrolyte on the anode before cleaning and imaging.

For the horizontal samples, a current density of 1.0 A/cm^2 was applied for 400 seconds and the voltage response measured. The anode assembly was made to specifically study the potential oscillations due to bubble build up and release. The bubble volume can be calculated using Faraday's law assuming ideal gas law as shown in Equation 7.4. Here, Δt is the average time for a bubble to grow and release, I is the current, F is Faradays constant, while the number of electrons

passed (n) is 4, R is the gas constant, T is the temperature, and the pressure P is assumed to be 1 atm.

$$V_{bubble} = \frac{I \cdot \Delta t \cdot R \cdot T}{n \cdot F \cdot P} \tag{7.4}$$

Bubble screening of the surface was investigated next, by holding the anode at constant voltage of 2.0 V for 2 minutes, evaluating the maximum and minimum current responses (Equation 7.5). As the anode is small, it is assumed that at the maximum current, I_{max}, the anode is free from bubbles [16, 25].

$$Screening = 1 - \frac{I_{min}}{I_{max}} \tag{7.5}$$

The sampling frequency was 10 or 100 Hz. Screening was also evaluated at 2.2 V, performed directly after the 2.0 V chronoamperometry measurements for selected samples. The measured responses for both chronopotentiometry and chronoamperometry were analysed with fast Fourier transform (FFT).

Chronopotentiometry was performed for the vertical samples, 400 seconds at 1.0 A/cm^2, followed by cyclic voltammetry (CV) from open circuit potential (OCP) to 2.3 V with 0.1 V/s and three cycles. The slow CV scan was considered comparable to polarisation curves. Electrochemical impedance spectra (EIS) were then recorded at OCP and voltages in the 1.4-1.7 V (w.r.t. Al) range in the frequency range 100000 Hz to 0.1 Hz. The AC amplitude was 50 mV. All EIS data were fitted to equivalent electrical circuits using ZView 3.5f by Scribner Associates, Inc.. The series resistance R_s, *i.e.* the ohmic resistance resulting from resistivity of the electrolyte and resistance in the leads to the electrode, was extracted from the high frequency OCP spectra and used to correct the measured chronopotentiometry and CV data. A LR(Q(R(LR))) equivalent circuit as described by Harrington and Conway [48], developed for the description of two-step electrochemical reactions with an adsorbed intermediate, was used to fit the impedance data. The equivalent circuit is provided in Figure 7.3a, where L is the inductance in the external wires, R_s is the series resistance, Q is the constant phase element used to model a non-ideal double layer capacitance, $R_{ct,1}$ and $R_{ct,2}$ are the charge transfer resistances, and the L_{ads} is an inductance associated with the adsorbed intermediate species. The effective capacitance (C_{eff}), corresponding to the double layer capacitance, can be derived in accordance with Equation 7.6 [49]. The model in Figure 7.3a presents two contributions from the constant phase

element Q, where the α in Equation 7.6 is the dimensionless constant of the Q (a value between 0 and 1 where 1 corresponds to an ideal capacitor).

(a)   **(b)**
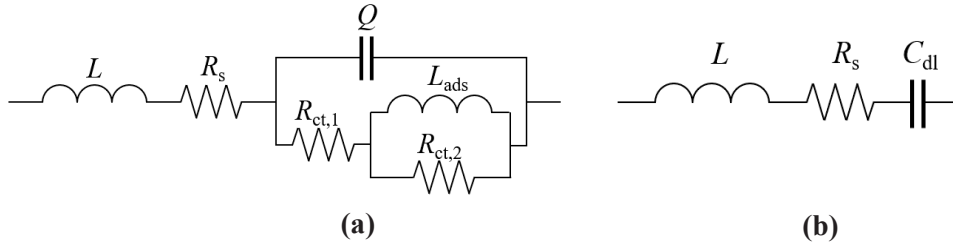
Figure 7.3: The two equivalent circuits used to model the system and extract the capacitance, the **(a)** LR(Q(R(LR))) and **(b)** LRC circuit, respectively.

$$C_{eff} = Q^{1/\alpha} \left(\frac{R_s \left(R_{ct,1} + R_{ct,2} \right)}{R_s + R_{ct,1} + R_{ct,2}} \right)^{(1-\alpha)/\alpha} \tag{7.6}$$

The high frequency data was also used to extract the double layer capacitance, C_{dl}. At high frequencies no faradic reactions are assumed to occur and a simple LRC circuit can be used (Figure 7.3b). The inductance L could be extracted from the imaginary impedance, Z_{Im}, at the highest frequency, f, (100000 Hz, Equation 7.7), as it may be assumed to be dominating at this frequency. The double layer capacitance can then be calculated according to Equation 7.8. By definition, the double layer capacitance should be constant in this frequency region (100000-5000 Hz), but in practice the value is only constant for a limited frequency range, which varied between samples (method described in *e.g.* [39], and an example is provided Appendix B). The capacitances, using both methods, were the reported in $\mu F/cm^2$.

$$L = L_{100000\,Hz} = \left(\frac{Z_{Im,100000\,Hz}}{2\pi f} \right) \tag{7.7}$$

$$C_{dl} = \left(\frac{1}{2\pi f \left(2\pi f L - Z_{Im} \right)} \right) \tag{7.8}$$

Information about the kinetics of the reaction can be extracted using the rewritten equations from [48]. The charge transfer resistance in Equation 7.9 will be a direct measure of the kinetics, assuming constant coverage of the adsorbed specie. As L_{ads} is a rather complex function of kinetic parameters, concentration and overpotential [48], the parameter τ, as given by Equation 7.10, has been applied in order to compare the adsorption process between the different anodes. τ is a time constant corresponding to the rate of relaxation of the coverage θ to a new value after a change in potential and is therefore a measure of the rate of adsorption in Equation 7.1.

$$\frac{1}{R_{ct}} = \frac{1}{R_{ct,1} + R_{ct,2}} = (\frac{\partial i}{\partial E})_{\theta} \qquad (7.9)$$

$$\tau = \frac{L_{ads}(R_{ct,1} + R_{ct,2})}{R_{ct,1} \cdot R_{ct,2}} \qquad (7.10)$$

7.3 Results and Discussion

7.3.1 Anode Properties

Physical parameters of the anodes are shown in Table 7.3. The sulfur level is lower than the coke sulfur content (Table 7.1) for all but anode A. The sulfur content in the pitch is lower than in the anode material, reducing the sulfur content of the anode with respect to the coke. The higher density anodes had lower SER than the low-density anodes. This does not include anode E, where a lower SER was observed despite the low density and high permeability. This is expected behaviour, as anode E is an isotropic anode, and the data reflects what is found in previous work on anodes made of isotropic coke [16, 50]. The low density and high permeability of anode E can be assumed to be caused by problems of achieving an optimum packing when the particles are spherical, resulting in more open porosity. Poor wetting between pitch and coke can also result in high open porosity in the anode.

Table 7.3: Physical parameters for the anodes performed by Hydro.

Coke type / Anode name	Density	Permeability	Specific Electrical Resistivity	S*
	(g/cm^3)	(nPm)	($\mu\Omega$m)	(wt%)
A	1.557	3.53	61.3	1.52
B	1.638	0.30	51.7	3.04
C	1.627	0.57	51.1	4.63
D	1.596	1.07	57.4	3.38
E	1.588	2.79	48.7	3.84

*The sulfur level is obtained from another pilot anode (0-6 mm fraction) and is therefore approximate.

7.3.2 Characterisation of Horizontal Anodes

Electrochemical characterisation of anodes with the horizontal assembly at 1.0 A/cm^2 showed the expected periodical oscillations corresponding to bubble formation, growth and coalescence, and finally release. Examples of the recorded voltage for graphite and all five anodes are shown in Figure 7.4, with a high sampling frequency (100 Hz). The oscillation amplitude and Δt were extracted manually from five bubbles near the end of the chronopotentiometry measurement; the averages are assumed representative for that parallel. However, some samples were observed to have bubbles of dissimilar sizes (like anode D in Figure 7.4 with an irregular oscillation pattern). In this case the average was determined from the larger bubbles, as these were consistent with the oscillation in the other parallels. Some oscillation sequences exhibited partial bubble release; the amplitude was close to maximum, but when the potential dropped to a significantly lower value it did not reach the minimum. These bubbles were not included (possibly leading to an overestimated Δt). For graphite, the bubbles were observed to release with a higher frequency than the anodes, and the recorded oscillation amplitude is larger. The anisotropic cokes are very similar to each other. Anode E, made of the isotropic coke, has the smallest oscillation amplitude and the bubble shielding of the surface appears more slowly.

A fast Fourier transform (FFT) algorithm was used on the potential *vs* time measurement for the last 2 minutes of the measurement to get a more precise Δt than manually extracting an average for bubbles in the last 30 seconds. FFT was also used as a quality check to confirm whether a pseudo-steady potential was obtained with a relatively constant oscillation amplitude and Δt during the last 2 minutes. The presence of one significant peak is an indication that steady state is

achieved, while more than one peak in the same region is probably due to a constant shift in oscillations over time, or a large variation in bubble sizes being released from the anode surface. The results are shown in Figure 7.5 for the samples shown in Figure 7.4 (and expanded on in Appendix A).
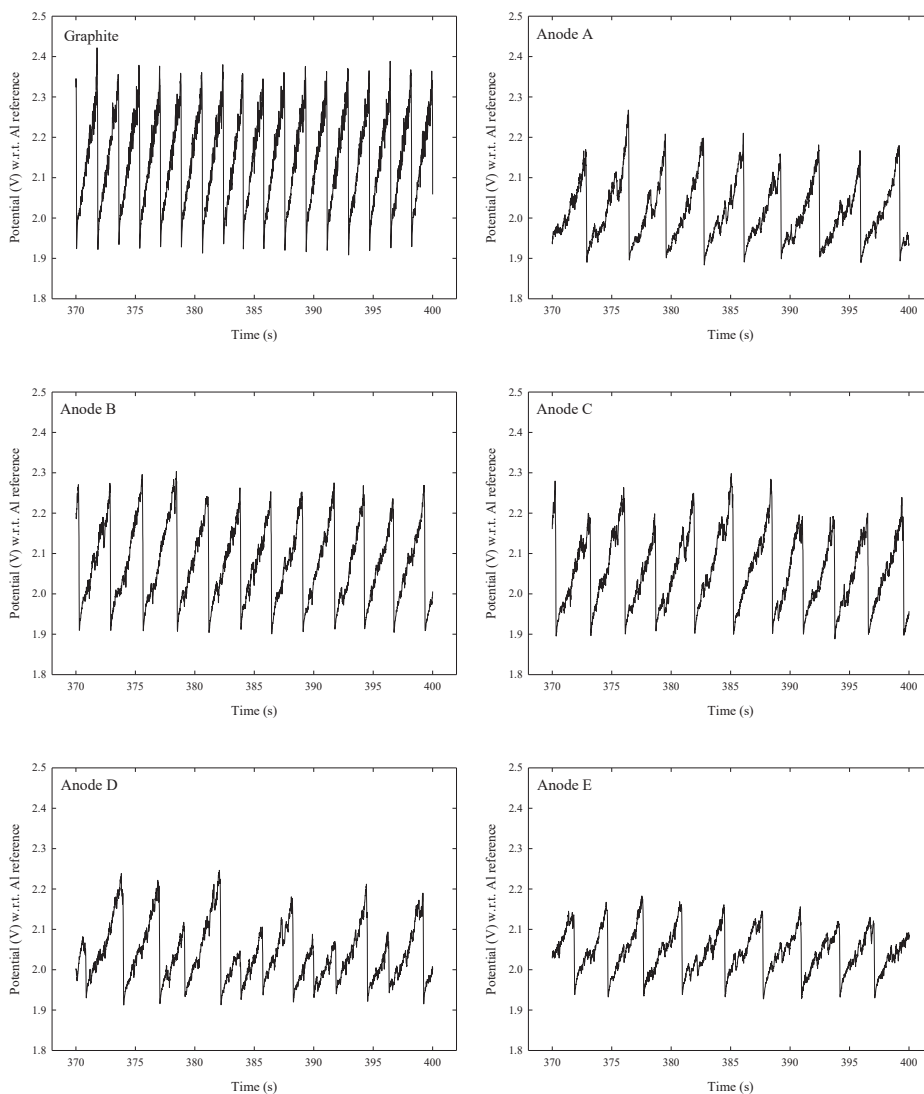
Figure 7.4: Examples of measured potential *vs* time for graphite and one parallel of the pilot anodes at the end of 400 s when constant current density of 1.0 A/cm^2 was applied.
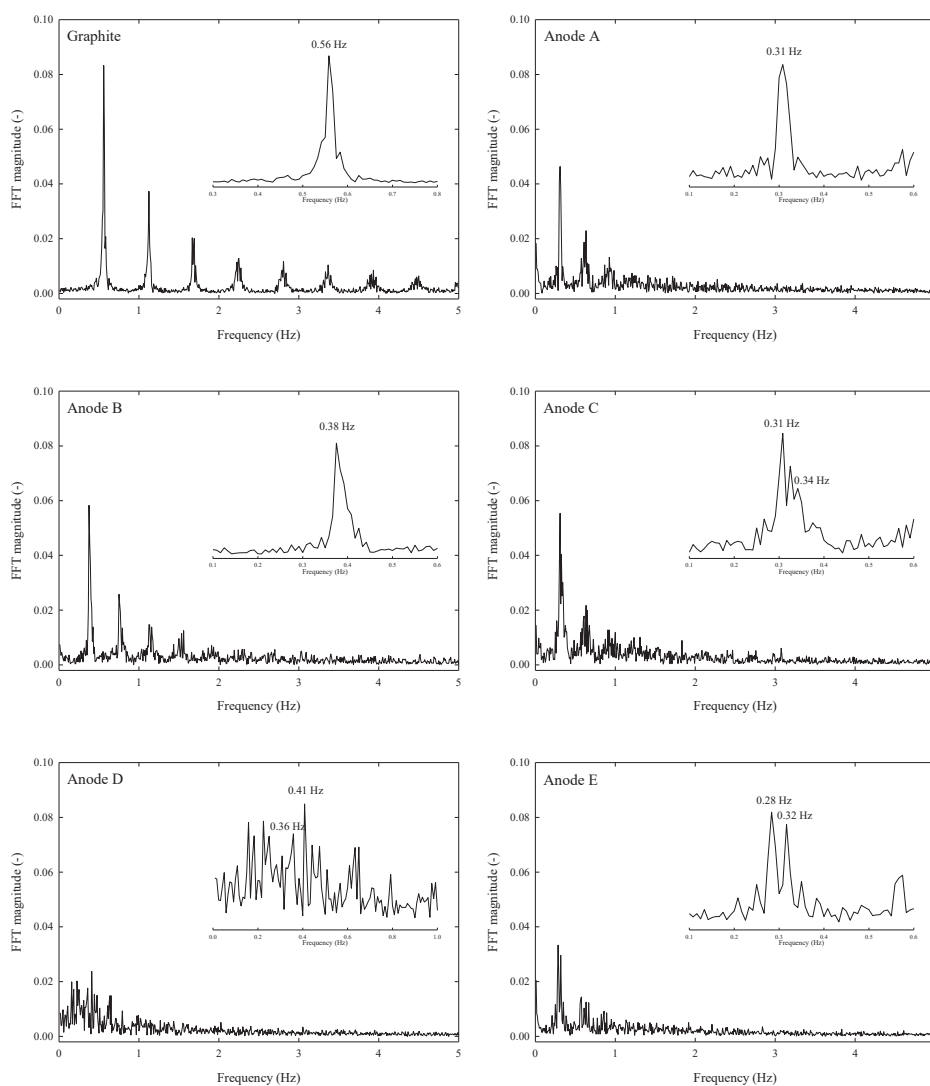
Figure 7.5: The frequency distribution from the fast Fourier transform (FFT) results for the last 2 minutes of the measurements at constant current density of 1 A/cm^2.

The main FFT peak was in the range 0.28-0.39 Hz and is marked in the figures. For graphite, as well as anodes A and B, the main peak correlated well with the average bubble periods extracted from Figure 7.4 (*i.e.* during the last 30 seconds). In this case the pseudo-steady state was achieved. For anode D the FFT result was

noisy. This was expected, as a large variation in the bubble amplitude and time was observed in Figure 7.4 for this anode. The two peaks marked correspond to the small and large bubbles. The FFT results of anodes C and E had several peaks of approximately same magnitude, indicating that the pseudo-steady state was not achieved. For all samples the bubbles got smaller and released more quickly after longer electrolysis time, shifting the peak to a higher frequency (example in Appendix A). One of the peaks marked in Figure 7.5 for anode C and E corresponds to the maximum FFT magnitude frequency, the other the frequency obtained by manual evaluation of the data in Figure 7.4.

The cause of variations observed between parallel samples from the same pilot anode is assumed to be twofold. First, there are some variations within the pilot anode and the samples are extracted from various part of the anode (also observed by Thorne *et al.* [21]). Results from analysis of variations in the surface roughness is provided later. Second, with the experimental setup it is difficult to position the sample precisely horizontal, and a tilt can greatly affect the bubble behaviour [29]. This is confirmed by considering the relationship between oscillation amplitude and Δt for bubbles on the same sample, as well as for samples of the same pilot anode (Appendix A). This relationship was close to linear, indicating that the bubble growth rate is the same. Considering the variable bubble sizes in Figure 7.4 for anode D also illustrate this; the slope for the increasing voltage with time is the same, 0.10 V/s, for all bubbles independently of final size (details in Appendix A).

Figure 7.6 shows the summary of the oscillation amplitudes for the anode samples. For graphite, the results appear to depend on the sampling frequency (Figure 7.6a), 10 Hz was not a sufficient sampling frequency. For the anodes, the variation between samples does not appear to be an effect of the sampling frequency. Figure 7.6b shows the average oscillation amplitudes for all samples, in the range 0.21-0.39 V.
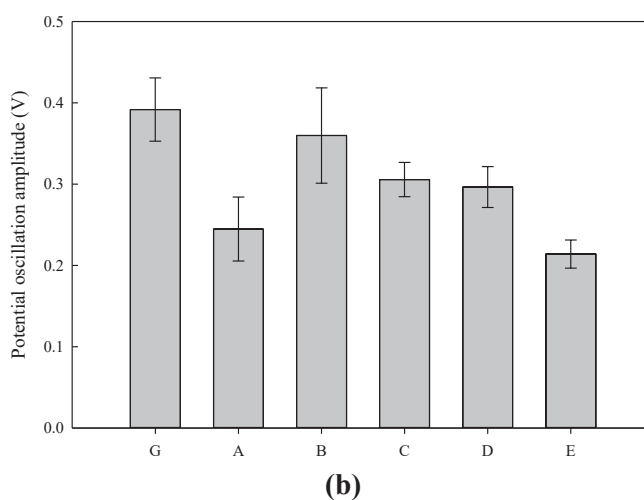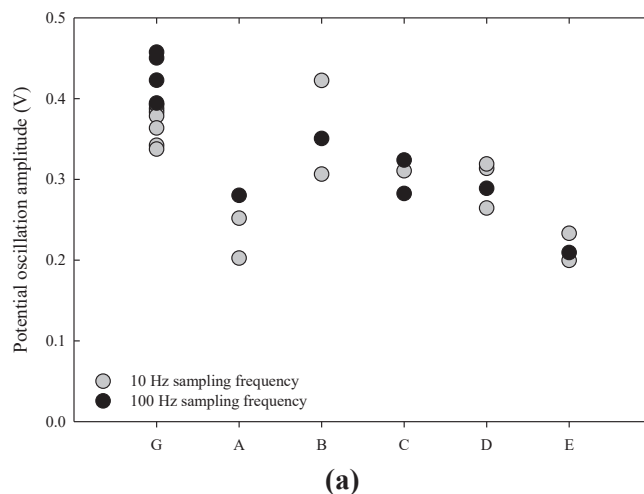
Figure 7.6: The potential oscillation amplitudes for the bubble evolved during electrolysis at 1.0 A/cm^2 for 5 selected bubbles at the end of the 400 s period. **(a)** The parallels evaluated to be representative and **(b)** average results with error bars using one standard deviation.

The observed voltage oscillation amplitudes for the anodes are similar to the results obtained by Sommerseth [16] and Thorne *et al.* [21], who investigated similar sized samples with identical furnace setup. They evaluated the isotropic anodes to have close to 0.2 V lower voltage amplitude than the fully anisotropic

anode, and similar values are observed between anode B and E in this study (Figure 7.6b). Anodes B, C and D were all very similar and have significantly higher amplitudes than the isotropic coke. The only other anode with oscillations approaching the isotropic coke was anode A, but this is likely caused by the anode properties rather than coke properties; this anode had higher permeability and lower density than the rest of the anisotropic anodes. The results add to the suggestion that using isotropic cokes indeed is a potential for energy saving in the aluminium production process. In addition, the results suggest that high porosity and permeability (*i.e.* high surface roughness) is an advantage for the bubble oscillation potential of small samples; total pore area and pore diameter are known factors known to affect this response [29].

Faraday's law was used to estimate the bubble volume according to Equation 7.4 (proportional to Δt). As seen in Figure 7.7, the bubbles formed at anodes A and E have a larger volume than anodes B, C and D. These anodes also have a similar and lower potential oscillation amplitude than A and E, confirming Einarsrud's modelling results [29] and other experimental observations [30-33]. This indicates less screening of the anodes or fewer possible nucleation points; both are further analysed in the next paragraphs. The uncertainties for the FFT main peak calculation for C and D are affected by the previously discussed variation of bubble size and time during the last 2 minutes (pseudo-steady state not achieved).
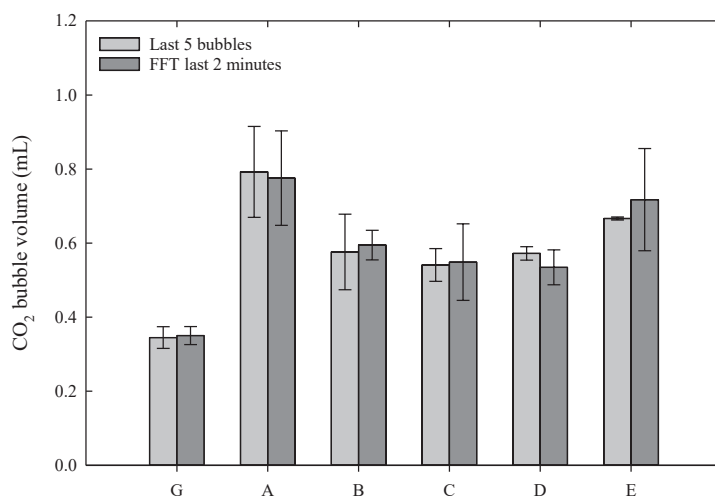

Figure 7.7: The average CO_2 bubble volume as calculated by Faraday's law using 5 bubbles at the end of the 400 s 1.0 A/cm^2 period and the FFT analysis using the last 2 minutes. Error bars show one standard deviation.

Figure 7.8 shows the chronoamperometry results recorded with constant voltage of 2.0 V for the same anodes as presented in Figure 7.4. The measurement is performed directly after the chronopotentiometry measurements, and the surface is assumed to be unchanged. The bubble frequency increased slightly by increasing the voltage to 2.2 V, as can be observed from the FFT graphs of anode B in Figure 7.9a, but the calculated screening was within the standard deviation between parallels (Appendix A). A larger effect was observed for graphite (Figure 7.9b), partly due to the higher overpotential of graphite, and the screening on graphite is still significantly larger than for the anodes.

The average screening presented in Figure 7.10 is obtained from measurements at 2.0 V. The bubble screening was very similar for all the anodes. It was 34 % for the isotropic anode E, around 40 % for anodes A, C and D, and highest average screening of 49 % was observed for anode B. The results reflect the potential amplitudes in Figure 7.6, confirming that higher screening is observed for anode B with highest potential oscillations. However, considering the standard deviations (especially for anode C) no significant differences can be established between the anisotropic cokes. Values of 35-50 % were observed for other anisotropic cokes using anodes of similar size [16, 21], therefore the values in this study are within what are expected using the same geometry of the samples. For anode E the screening is somewhat larger than what was observed in [16, 21] for the isotropic cokes, where values around 20 % was achieved. As mentioned earlier, this is possibly due to the difference in permeability of the anodes, which was much higher for the isotropic anodes investigated by Thorne *et al.* [21] than the isotropic anode E in this study. The high graphite maximum screening is consistent with the higher potential oscillations and faster bubble release frequency compared to the anodes made from the industrial cokes.
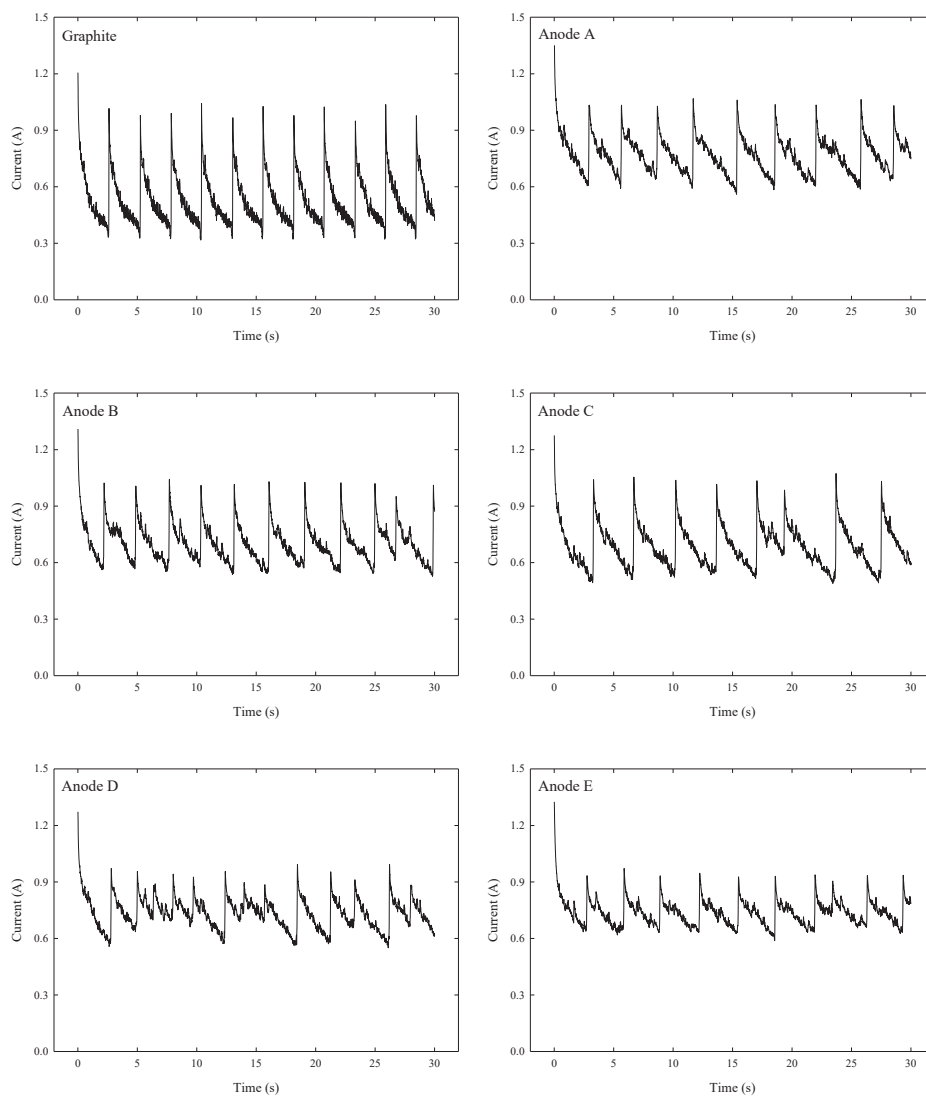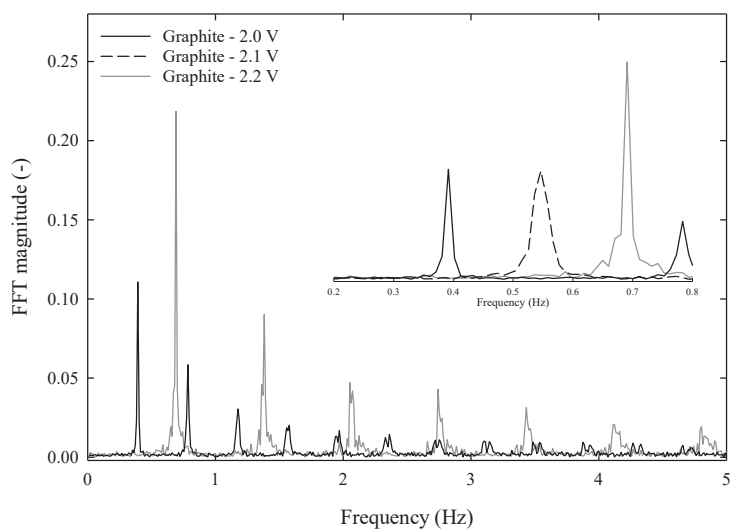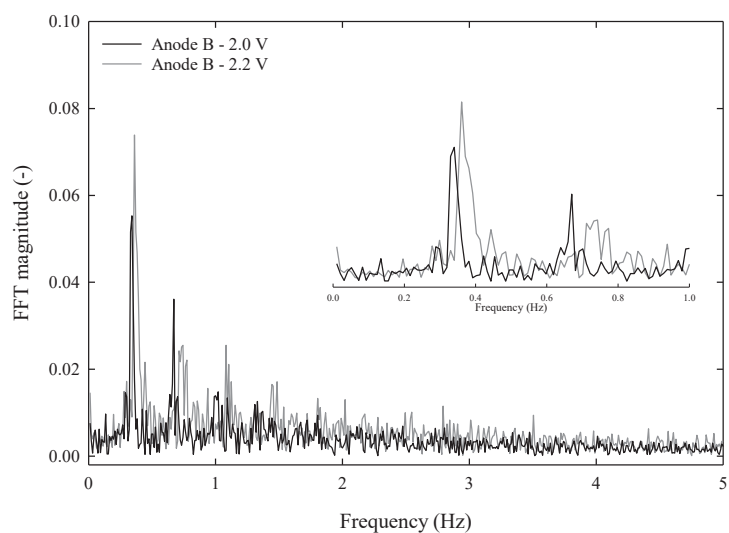
Figure 7.8: Examples of measured current *vs* time for graphite and one parallel of each of the pilot anodes when a constant voltage of 2.0 V was applied.

(a)

(b)

Figure 7.9: The frequency distribution from the fast Fourier transform (FFT) results for 1 minute of the measurements at constant voltage for **(a)** graphite and **(b)** anode B.
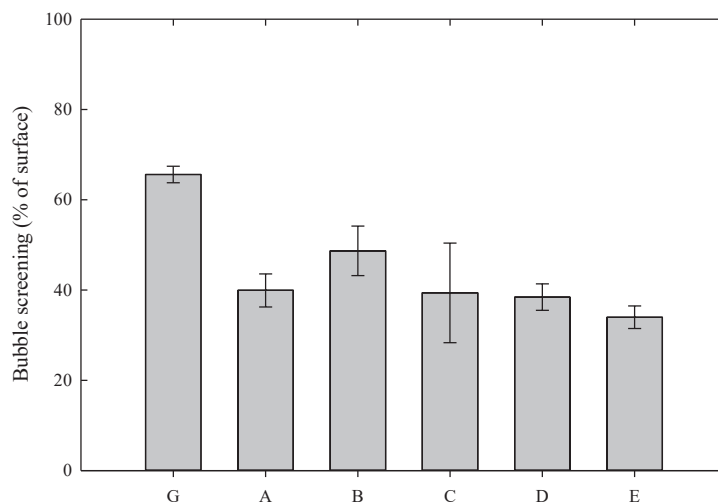
Figure 7.10: Bubble screening of the surface at maximum bubble coverage calculated from using minimum and maximum measured current at constant voltage of 2.0 V.

Gebarowski *et al.* [25], using a larger geometry (41 mm diameter electrodes), investigated the anisotropic pilot anodes of A, B and C. The potential amplitudes were larger than in this study, assumed to be caused by the longer distance bubbles have to travel before release. The variations between the anodes were small, but anode C, with the highest sulfur content, had lower amplitudes than anode B in this study as well. Very small variations between the screening of the anodes was observed (screening was less than 25 %, *i.e.* significantly smaller than obtained in this study). Thorne *et al.* [21] studied horizontal graphite anodes with 8, 10 and 14 mm diameter, and these gave very similar potential oscillation amplitudes and screening, while the 6 mm anode was completely blocked by bubbles. A larger sample is assumed to exclude some of the larger uncertainties assumed to be caused by local differences in the pilot anode, for example the variation of pores on the electrochemically investigated surface observed for small samples. On the other hand, for the larger anodes (*e.g.* 41 mm), multiple bubbles will form and escape from the anode, implying that bubbles will be transported along the surface before escape. This latter effect may be excluded for smaller anodes, as bubble events are mainly related to formation of eventually one large bubble.

The observed effects of bubbles in this study correlates with the permeability of the anodes, where the higher permeable anodes have lower voltage amplitudes, frequencies and (in some degree) screening. The possibility of gas escaping

through the anode due to high permeability was addressed by Thorne *et al.* [21]. Estimates showed that due to the relatively low overpressure below the anode in the laboratory scale set-up, the escape of gas through the anode is limited, and also the capacity of the anode to act as a gas reservoir is low. However, the highly permeable anodes have been observed to generally have a different behaviour than similar low permeable anodes [16, 21, 25]. Consequently, this may be because of presence of more, or different sized, surface pores on the investigated surface area, which is believed to be the nucleation points for CO_2 bubbles, rather than the possibility of gas "escaping" through the anode.

For the anodes studied in this work, the true area/projected area (TA/PA) ratio obtained from the confocal microscopy analysis of unused samples, was used in combination with visual observation of pores using the 3D profiles to evaluate the surface roughness. The TA/PA ratios for several parallels of the different anodes are presented in Figure 7.11, while the 3D profiles can be examined in Appendix C.
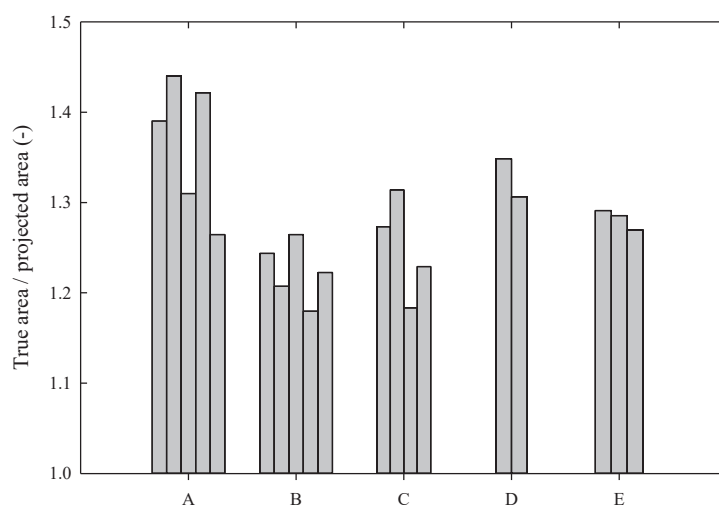
Figure 7.11: The true area/projected area (TA/PA) obtained using a confocal microscope.

For the anisotropic anodes the roughness correlates well with the permeability. Anode A, with the lowest density and highest permeability, had the highest TA/PA ratio, correlating to many large open pores increasing the true surface area. The high density and low permeable anode B had the lowest TA/PA ratio, which is logical as it may be assumed that there are fewer large pores in samples taken

from this pilot anode. The isotropic anode E was expected to have larger roughness as well, due to the lower density and high permeability, but the TA/PA was comparable to the ones for anodes C and D. Furthermore, a significant variation in the sample roughness between the parallels from the same pilot anodes is observed, depending on quantity of large pores included in each investigated sample. These differences show that using a small aggregate size with grains smaller than 2 mm for the pilot anode, can still result in a large variation between investigated samples when the diameter is 10 mm.

The variations observed for samples of the same pilot anode can be assumed to cause some of the significant variations of the electrochemical measurements, and for the horizontal assembly, the pores and their sizes are assumed to be of high importance. For anode A the high roughness and many large pores resulted in lower voltage oscillation amplitudes and larger bubbles. This correlates well with Einarsrud's description [29], where larger pores facilitated lower bubble frequency and lower potential amplitudes. This behaviour was also observed in [21], where the highest TA/PA ratio also was observed for the anodes with lower bubble oscillation. Anode B have the lowest TA/PA ratio, correlating to smaller pores which again results in faster bubble frequency and higher voltage amplitudes.

The solid-liquid wettability will affect the bubble behaviour, and larger screening of the anode is expected with less wetting between anode and electrolyte. The wetting is affected by polarisation of electrodes, as shown in experiments applying immersion-emersion methods (described in [51, 52]). A comparison of wetting properties of polarised samples of graphite, anisotropic and isotropic cokes was done by Sommerseth *et al.* [38]. A decrease in wetting angle after polarisation was observed, thus increasing the wettability. The relative change varied depending on the material; a larger change was observed for the isotropic anodes. The lowest screening observed for the isotropic anode (Figure 7.10) is therefor expected, as anodes made of isotropic coke material has been shown to have better wetting properties between anode material and electrolyte, and this facilitates a higher contact angle between the formed gas bubbles and anode [16].

The isotropic anode E had, as expected, the lowest potential amplitudes, lowest screening of anodes, and the lowest bubble frequency. For the anisotropic anodes B, C, and -D, a larger oscillation amplitude was observed in combination with high surface screening at maximum coverage, and faster bubble release frequency. For the anisotropic anodes this corresponded well with the surface roughness, as the highest oscillations were observed for anode B, with the lowest TA/PA ratio.

Larger pores in the anisotropic coke A is suggested as the reason for this anode having bubbles similar in size and voltage amplitude as anodes made of the isotropic coke E, but high porosity is generally not wanted in industrial anodes. The combined results, considering the high permeability of all isotropic anodes, indicate that the properties of the anode, like baked density, permeability and roughness, also have a significant effect on the anode bubble mechanism independently of coke type.

7.3.3 Characterisation of Vertical Anodes

The *IR* corrected CV curves, comparable to polarisation curves, of graphite and three of the anodes are presented in Figure 7.12 (and in Appendix B). Graphite clearly have a higher overpotential at lower current densities than the anodes, in accordance with literature (see *e.g.* [20, 26]). Anode A and E have lower overpotential than anode D. The difference in gas formation on the surface of the graphite compared to the anodes is also visible in the polarisation curve, correlating to what is observed for the horizontal samples, where the bubbles are formed faster and release faster for the graphite than the anodes. Thus, minor bubble oscillations cannot be completely excluded on vertical electrode surfaces either.
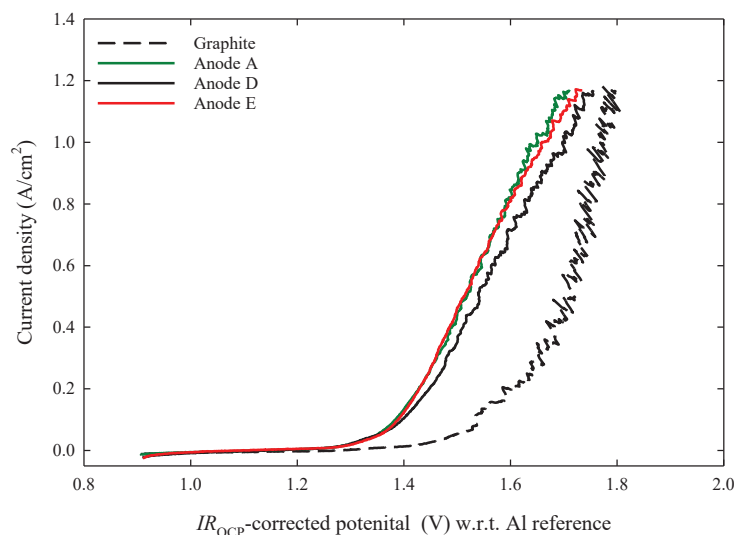
Figure 7.12: IR_{OCP} corrected CV curves of graphite, and anodes made of coke material A and D (anisotropic) and E (isotropic).

The anode overpotential reduction at 1.0 A/cm^2 with respect to graphite is presented in Figure 7.13 for the chronopotentiometry and CV curves. The general trend is the same whichever method is used; it looks like anodes made of coke material C and D have a marginally larger overpotential than anodes made of material A, B and E. Using the CV curves a larger difference is observed for the high sulfur anode C, but the chronopotentiometry results are considered more reliable because the values are obtained from an average of 50 s. The CV results are extracted when the voltage was changing with 0.1 V/s, assuming approximate linearity in the current density region around 1 A/cm^2 (which was difficult especially for the noisy signal for graphite. Within the standard deviation any differences between anode materials are difficult to identify.
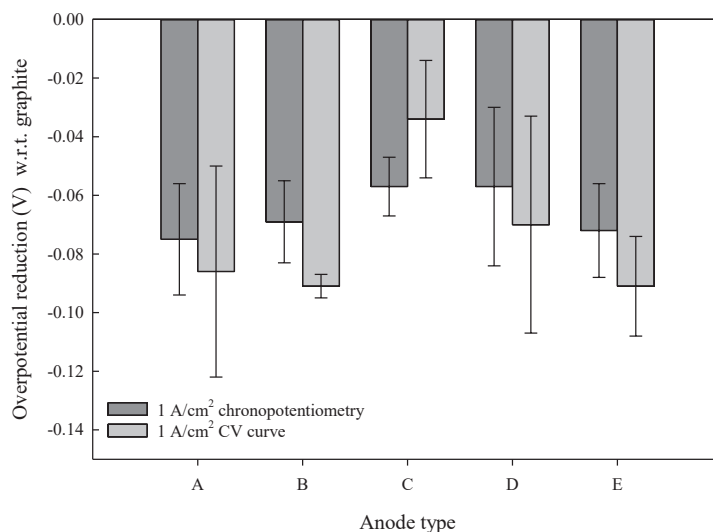
Figure 7.13: Anode overpotential reduction with respect graphite recorded by chronopotentiometry and polarisation. The error bars show one standard deviation based on 3 samples.

The Nyquist plots with the impedance raw data obtained at 1.5 V (not *IR*-corrected), and the modelled LR(Q(R(LR))) equivalent electrical circuit, is presented for the anode materials in Figure 7.14. Due to a difference in the in-house produced reference electrode, the graph for anode material C differs from the rest (also different scales on the axis). The graphite samples had much noise in the whole frequency range and fitting the data to the LR(Q(R(LR))) circuit was not possible. This is assumed to be because of the higher bubble noise, also observed in Figure 7.12.
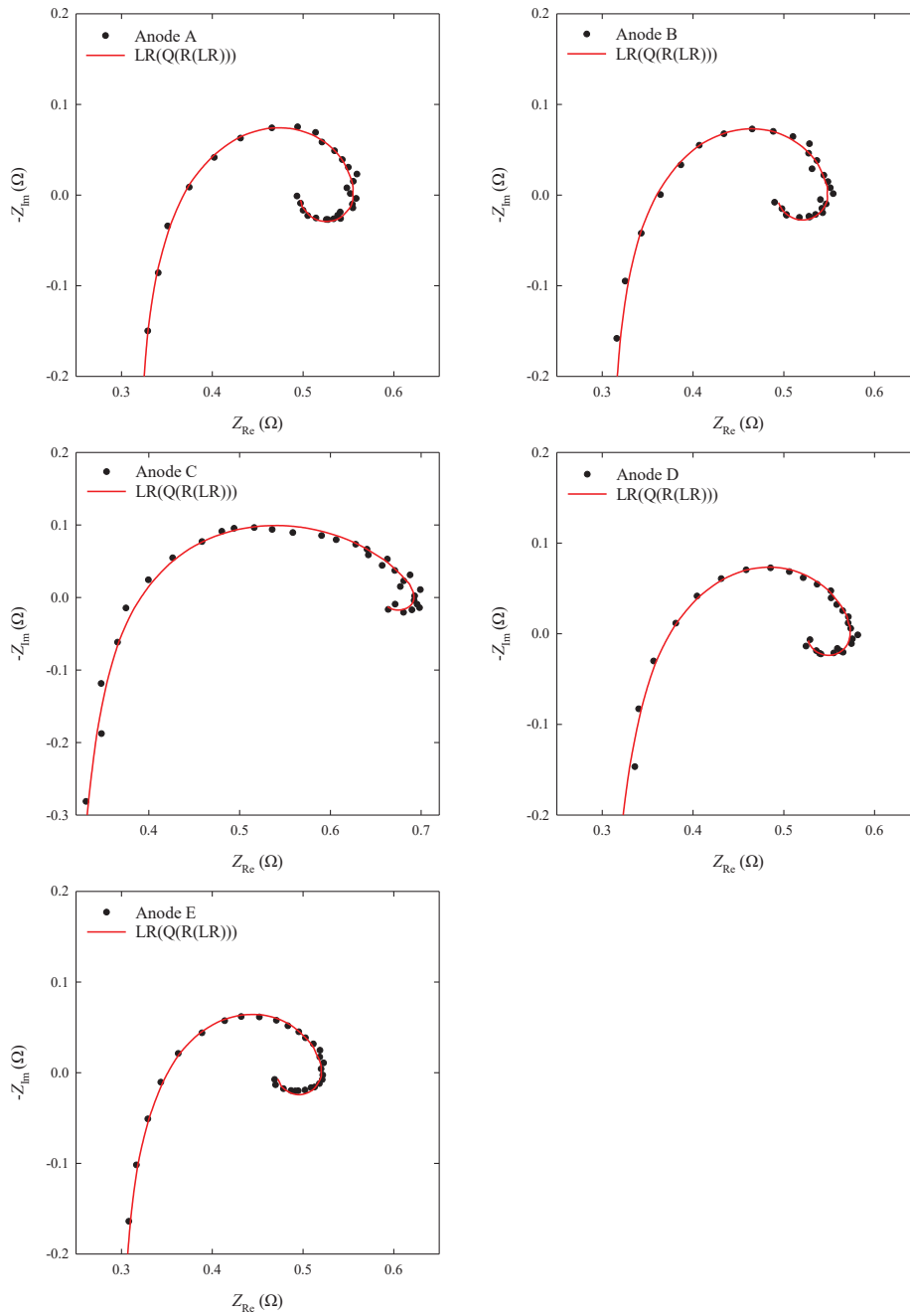
Figure 7.14: The raw data from EIS at 1.5 V (not *IR*-corrected) with the modelled equivalent circuit LR(Q(R(LR))).

The LR(Q(R(LR))) model can be used to estimate the effective capacitance, C_{eff}, from Q, in accordance with Equation 7.6 (the fits and calculated C_{eff} are presented in Appendix B). A simple LRC circuit can also be used to evaluate the high frequency data, assuming no Faradic reactions take place in this range, and the double layer capacitance, C_{dl}, can be extracted. A comparison between the capacitance determined by the two methods is shown in Appendix B; C_{eff} is always estimated lower than C_{dl}, but the trends are the same. The simple LRC model do not rely on data in the low frequency region and was used on a larger collection of EIS spectra obtained at different voltages (1.4 V to 1.7 V). For graphite, only the high frequency data and the LRC circuit was used to evaluate the capacitance.

To better compare the results from different days, C_{dl} is plotted against current density rather than potential. The result can be observed in Figure 7.15, where the capacitance is relatively unchanged at lower current densities for all anodes. This is similar to the observations of Gebarowski *et al.* [23], where the capacitance stabilised at a voltage around 1.3 V, when current has reached a certain level. Figure 7.15 also shows an increase in capacitance for several of the anodes at higher current densities; especially Anode E, which already have a significantly larger capacitance than the other anodes at all current densities investigated. The larger capacitance of the isotropic anode is comparable to what Sommerseth *et al.* [38] found, and the increase of capacitance for isotropic materials was also observed by Gebarowski *et al.* [23]. Gebarowski calculated capacitance values in the same range as in this study; Sommerseth reported higher values. The anisotropic anodes in this study had comparable capacitances. The significantly lower capacitance of graphite with respect to baked anodes was expected based on previous experimental observations [17, 38, 41].
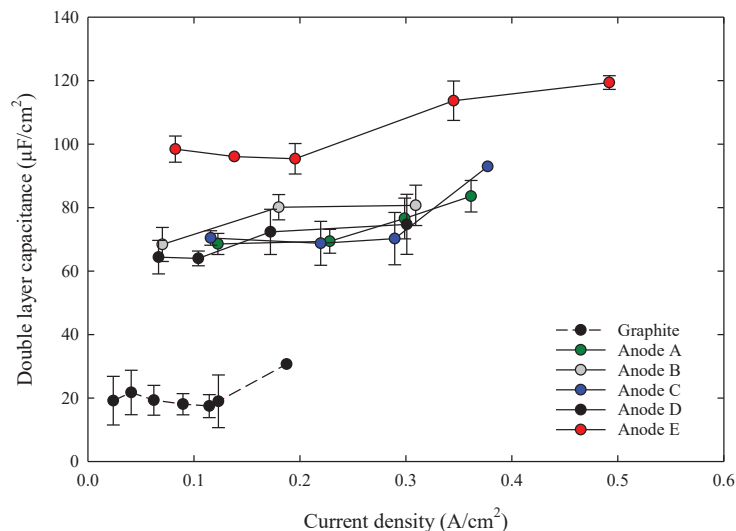
Figure 7.15: The double layer capacitance estimated with the LRC circuit w.r.t. current density, where standard deviation is given for n=(2-)3 samples.

Figure 7.15 shows that isotropic anode E has a double layer capacitance, C_{dl}, above 100 $\mu F/cm^2$. This is significantly higher than the anisotropic anodes, which all have very similar values around 70-80 in $\mu F/cm^2$. Anode A was shown to have higher surface roughness and large pores than the rest of the anisotropic anodes (Figure 7.11), but this is not reflected in a larger electroactive area for this anode. The observations indicate that the pores are filled with gas, and not available for the reaction. This was also the conclusion by Sommerseth *et al.* [53], who observed that electrolyte generally does not penetrate the pores on the surface. Sommerseth also showed little difference on the overpotential comparing anodes with different porosity and permeability, similarly to the chronopotentiometry results in this study (Figure 7.13).

Information on the total charge transfer resistance, R_{ct} (Equation 7.9) and on the rate of the adsorption reaction (Equation 7.1), as given by the time constant τ (Equation 7.10) were also extracted from the impedance spectra. All data are provided in Appendix B. Due to variations in the measurements performed at different days (most probably due to the reference electrodes), only samples measured the same day were compared. The results are shown in Table 7.4, showing that anode E has a lower charge transfer resistance than anodes B and D. Similarly, anode A appear to have a lower charge transfer resistance than anode

C. No differences could be observed for τ. The improved kinetics of anode E is consistent with the higher capacitance for this anode.

Table 7.4: The charge transfer resistance R_{ct} and time constant τ, average values for three parallels (except Day 1 – A, only one parallel).

	1.5 V		1.6 V	
	R_{ct}	τ	R_{ct}	τ
	(Ω)	(ms)	(Ω)	(ms)
Day 1				
A	0.250	7.851	0.160	2.996
B	0.260	7.405	0.157	2.996
D	0.273	7.928	0.167	2.668
E	0.237	7.768	0.140	3.026
Day 2				
A	0.350	25.349	0.215	5.073
C	0.387	27.161	0.237	3.682

R_{ct} and τ were plotted *vs* current density in the range 0.1-0.35 A/cm^2, as shown in Figure 7.16. As may be inferred from the figure, they all follow a similar exponential decay as the current density increases, implying that the mechanisms of the reactions appear to be the same.
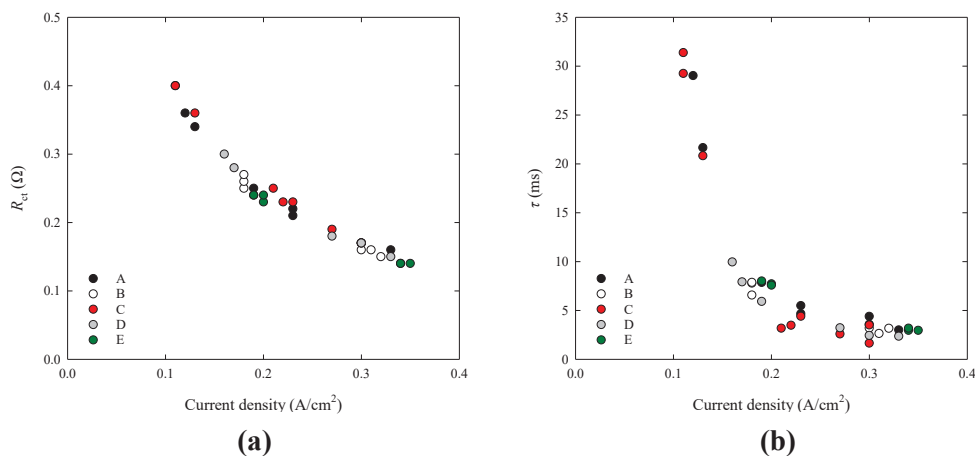

Figure 7.16: (a) The total charge transfer resistance and **(b)** time constant τ plotted with respect to the current density.

The vertical anode assembly results correlate well with previous investigations on anisotropic and isotropic anode materials [23, 24, 38]. Lower overpotential at 1 A/cm^2 and higher capacitance in the 0.1-0.35 A/cm^2 region was observed for anodes made of isotropic coke compared to those made of anisotropic cokes. Higher capacitance indicates higher electrochemically active area for isotropic anodes, possibly correlating to better wetting between anode and electrolyte. Considering the standard deviations, the differences observed between the four anisotropic anodes A-D were small, both with respect to overpotential and capacitance, and the higher porosity and surface roughness observed for anode A did not seem to have a significant effect on the reaction overpotential.

7.3.4 Unshielded Anode Assembly

The optical images obtained for the anode before and after the electrolysis of the unshielded anodes, held for 40 minutes at 1.0 A/cm^2, corresponding to consumption of wear of approximately 0.5 mm (0.18 g carbon) are presented in Figure 7.17-Figure 7.18. The 3D maps can be further examined in Appendix C. For all the anisotropic cokes there are some pronounced large grains that clearly have not been consumed at the same rate as the rest, while for the isotropic anode E the spherical grains of different sizes appear to have been consumed roughly at the same rate. One grain was identified in anode E with less consumption, and is likely an anisotropic grain, and can be further examined in Appendix C.

The TA/PA ratios before and after electrolysis is presented in Table 7.5. Anodes A, B and C all had a roughness increase of 20 %, while E only had 10 %, confirming the visual inspection of the optical images in Figure 7.18. Anode D also increased with 10 %, but the start value was the highest and a variation in grain consumption is still observed in the optical images. The values are somewhat lower than expected based on the work by Sommerseth [16] as well as EIS measurements by Thonstad [54]. However, the level of consumption differed considerably from these studies; Sommerseth applied 1 A/cm^2 for 25 minutes and Thonstad reported an average wear of 2 mm.
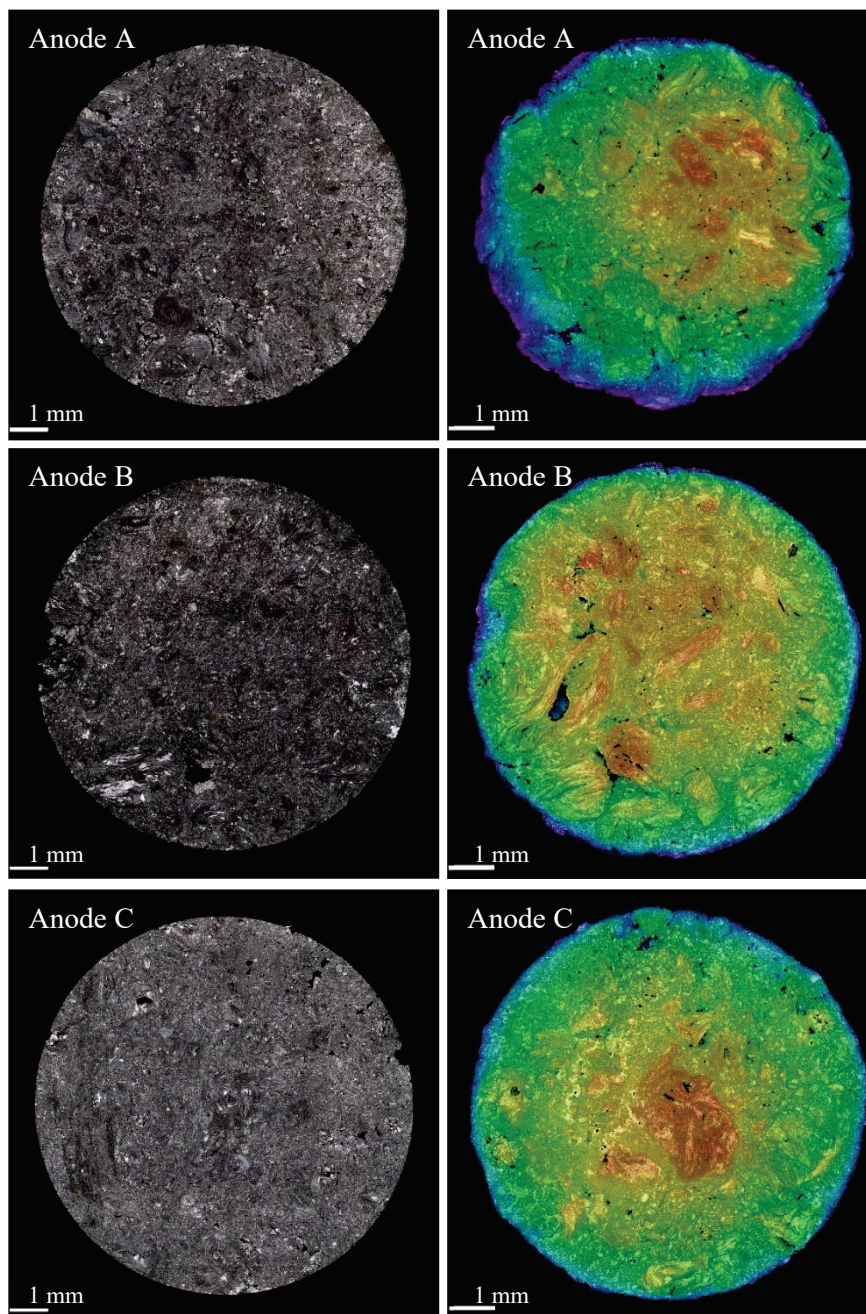
Figure 7.17: Imaging of anodes before (surface map) and after (contour map) electrolysis for 40 minutes, 1 A/cm^2, for anodes A, B and C.
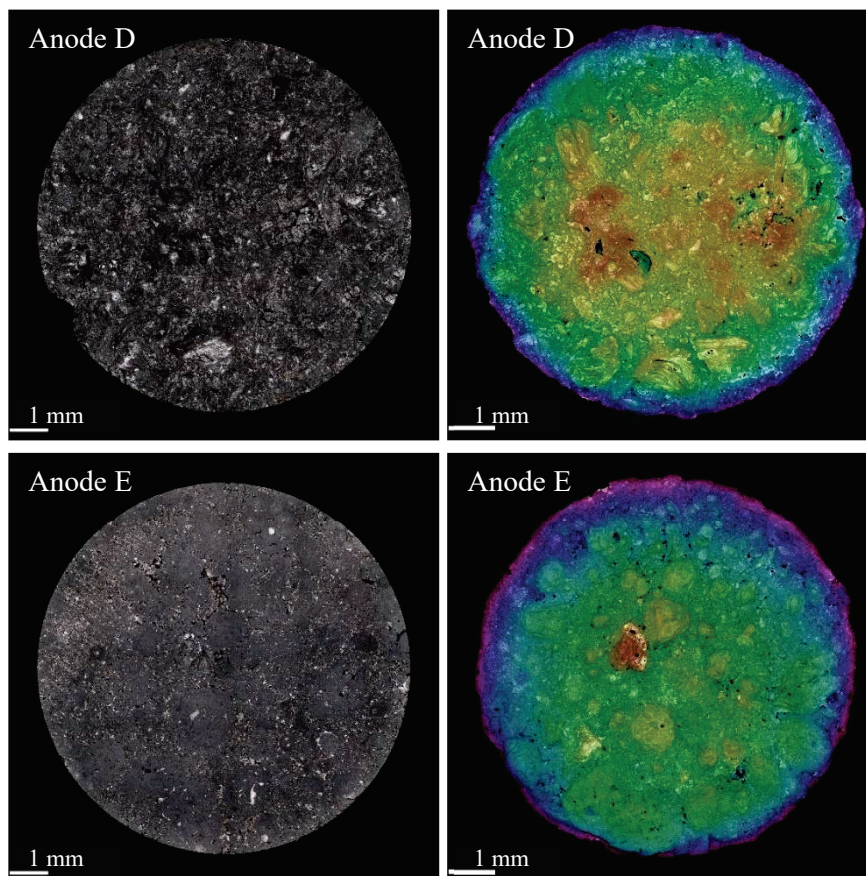
Figure 7.18: Imaging of anodes before (surface map) and after (contour map) electrolysis for 40 minutes, 1 A/cm^2, for anodes D and E.

Table 7.5: Roughness increase for the anodes before and after electrolysis of 40 minutes at 1 A/cm^2. The anodes were polished before electrolysis.

Anode	TA/PA before	TA/PA after	Increase in surface roughness (%)
A	1.23	1.49	21.0
B	1.17	1.42	21.4
C	1.10	1.30	17.5
D	1.26	1.40	10.9
E	1.15	1.27	10.1

The results from the single anodes cannot be directly transferred to the results concerning the horizontal and vertical anode assembly. Only one sample of each anode was investigated, and the surface was polished. The results on anode A did confirm the possibility of large pores and porosity of this anode resulting in a higher roughness and possibly affecting the bubble behaviour, as anode A had a high initial TA/PA even after the surface was polished.

7.3.5 Evaluating Microstructural Properties of Coke

Thorne *et al.* [20] and Sommerseth *et al.* [38] previously observed some correlations between the anodic reaction overpotential, electrochemically wetted surface area (evaluated by C_{dl}) and anode-electrolyte wettability when comparing anisotropic and isotropic cokes. Except for the wettability, which was not measured in this work, similar results were obtained in this study, with the isotropic coke having slightly lower overpotential and higher C_{dl} than the anisotropic anodes. In the work of Thorne *et al.* [20], the cokes were also (extensively) characterised. The isotropic cokes had more reactive edge sites, lower $CO:CO_2$ ratio, more small pores (width < 16 nm) and higher impurity content [20]. The air reactivity was also evaluated, and a trade-off was suggested; a reduction in anode overpotential by allowing higher air reactivity using isotropic coke [24]. The behaviour was proposed to be caused by more reactive edge sites and a difference in oxide groups for the isotropic cokes. However, the properties of the same anodes [21] showed a large permeability and noticeably larger TA/PA for the isotropic anodes compared to the anisotropic anodes, which also could explain the difference in electrochemical reactivity. Some of the observations contradicts what is observed for the cokes in Chapter 5 [45], which shows the difficulty in separating "isotropic cokes" from "anisotropic cokes"; a larger collection of both types is necessary to make strong conclusions.

The microstructure of the coke materials in this study was thoroughly examined in Chapter 5 [45]. The isotropic coke E had less edge sites (more basal planes) and higher $CO:CO_2$ ratio than the anisotropic cokes, while the opposite was observed by Thorne *et al.* [20]. In this work, it was also observed that coke D had significantly more basal planes and defect sites than the rest of the anisotropic cokes, correlating to the higher amount of S-S bound sulfur observed for these cokes [44] and higher portion of small pores. With respect to electrochemical performance, anodes made of coke D behaved more closely to the anisotropic anodes than the isotropic anode E.

The improved electrochemical reactivity previously documented for isotropic cokes, in agreement with the results in this study for anode E, is likely an effect

of both coke and anode properties. The variation between the anisotropic coke materials, and different combinations concerning impurities, porosity and reactive sites as identified by edge sites (*vs* basal planes) had a very small effect on the electrochemical reactivity. The low voltage oscillations observed for the low-sulfur anode A was likely an effect of the anode properties, while the remaining anisotropic anodes with similar physical properties had the same voltage oscillations. These observations indicate that that anode properties are an important factor regarding the electrochemical investigations for the anisotropic anodes rather than the microstructure of the grains.

7.3.6 Evaluating the Effect of Sulfur

Previous investigations by Thorne *et al.* [20, 21] focused on the comparisons between isotropic and anisotropic anode materials, while Sommerseth blended anisotropic and isotropic material [16]; Thorne included two anisotropic petroleum cokes with anode sulfur levels of 0.94 and 2.40 wt% S respectively. No significant differences were discovered between these, and they behaved similarly with respect to electrochemical characterisation in both horizontal [21] and vertical [20] anode assemblies. Differences between anisotropic and isotropic anodes were however clear and comparable to this study, but whether this was an effect of the coke properties or anode properties could not be confirmed. Gebarowski *et al.* [25] focused on the effect of sulfur in anisotropic anode materials and discovered small differences regarding the horizontal anode measurements. He also mentioned an effect of the anode permeability, which was assumed to cause large difference in the voltage oscillations. Permeability was also questioned by Thorne *et al.* [21] and Sommerseth [16], since the spherical isotropic grains are more difficult to pack and usually results in an anode with higher permeability.

The anisotropic anodes, with a large variation in coke sulfur content (1.4-5.5 wt% S), exhibit a very similar electrochemical performance in this study, both with horizontal and vertical anode assemblies. The lower voltage oscillations for low sulfur anode A is most likely an effect of the porosity and surface roughness rather than the low sulfur and metal content, similarly to what Gebarowski *et al.* discussed [25]. Coke C had 2 wt% more sulfur than anode B, while having the same metal content, density and SER, as well as only small differences in permeability and TA/PA ratio. However, considering the large standard deviation between samples, differences in the reaction overpotential between anisotropic anodes could not be confirmed, indicating no negative effects on the electrochemical performance of anodes by using high sulfur coke. A similar comment can be made related to metallic impurities. The significant variation in

the level of some impurities, like V, does not seem to impact the electrochemical performance.

The aluminium industry needs to utilise more high-sulfur cokes in the future. In practice, anodes are made from a blend of cokes, and blended anodes might give very different results depending on what cokes and what recipes are used. If a negative effect for high sulfur cokes is higher overpotential, the effect can possibly be remedied by also blending with some isotropic coke. These cokes have repeatably been shown to have positive effects on overpotential and electrode-electrolyte wetting, but both thermal expansion and problems with packing need to be kept in mind when fabricating these types of anodes. However, using high sulfur cokes in anode production will lead to a larger production of SO_2, which for many smelters will be very important.

7.4 Conclusions

Electrochemical characterisation of pilot anodes made of single source industrial cokes showed very small differences between the anisotropic cokes with sulfur levels varying from 1.4 to 5.5 wt%, and also with a wide range of various metallic impurities. The isotropic coke resulted in anodes with lower charge transfer resistance and higher double layer capacitance, as well as lower voltage oscillations and bubble frequency related to bubble formation and growth. These effects are likely a combination of anode properties, and coke properties associated with isotropic cokes. Similar bubble behaviour was also observed for the highly permeable, low density, anisotropic anode. This is attributed to the high permeability, and low density, of this anode, resulting in large pores acting as nucleation points on the surface. The difference in porosity was not found to affect the reaction overpotential or double layer capacitance when comparing with the other anisotropic anodes only. An increase in sulfur and metal in cokes will influence the purity of the primary metal and the produced SO_2, but considering the anisotropic anodes only, no negative effects on the electrochemical reactivity could be identified in this work.

The lab scale investigation cannot be directly transferred to industrial scale due to the very different size of the anodes and the progressive rougher surface during electrolysis. Knowing how anodes made from a single coke behaves can be a good basis for further explaining behaviour of blended anodes.

References

[1]   J. Thonstad, P. Fellner, G.M. Haarberg, J. Híveš, H. Kvande and Å. Sterten. *Aluminium Electrolysis: Fundamentals of the Hall-Héroult Process.* 3rd ed. Aluminium-Verlag: Düsseldorf, 2001.

[2]   H. Kvande and W. Haupin. Cell Voltage in Aluminum Electrolysis: A Practical Approach. *JOM* (2000), **52**(2), pp. 31-37.

[3]   A. Gomez and R. Heilgendorff. Carbon Plant Performance with Blended Coke. *Light Metals* (2005), pp. 535-538.

[4]   L. Edwards, F. Vogt and J. Wilson. Coke blending at Anglesey Aluminium. *Light Metals* (2001), pp. 689-694.

[5]   L. Edwards. The History and Future Challenges of Calcined Petroleum Coke Production and Use in Aluminum Smelting. *JOM* (2015), **67**(2), pp. 308-321.

[6]   L. Edwards, N. Backhouse, H. Darmstadt and M.-J. Dion. Evolution of Anode Grade Coke Quality. *Light Metals* (2012), pp. 1204-1212.

[7]   T.A. Aarhaug and A.P. Ratvik. Aluminium Primary Production Off-Gas Composition and Emissions: An Overview. *JOM* (2019), **71**(9), pp. 2966-2977.

[8]   S.S. Jones and R.D. Hildebrandt. Influence of High-Sulfur Cokes on Anode Performance. *Light Metals* (1979), pp. 553-574.

[9]   P.J. Rhedey. Carbon Reactivity and Aluminum Reduction Cell Anodes. *Light Metals* (1982), pp. 713-725.

[10]   K.N. Tran, S.K. Bhatia, A.J. Berkovich and A. Tomsett. Influence of Sulfur and Metal Microconstituents on the Reactivity of Carbon Anodes. *Energy Fuels* (2009), **23**(4), pp. 1909-1924.

[11]   H. Alhajibrahim and B. Morsi. Desulfurization of Petroleum Coke: A Review. *Ind. Eng. Chem. Res.* (1992), **31**, pp. 1835-1840.

[12]   L.C. Edwards, K.J. Neyrey and L.P. Lossius. A Review of Coke and Anode Desulfurization. *Light Metals* (2013), pp. 130-135.

[13]   T. Eidet. *Reactions on Carbon Anodes in Aluminium Electrolysis.* PhD thesis. Norwegian University of Science and Technology, 1997.

[14]   G.J. Houston and H.A. Øye. Consumption of anode carbon during aluminium electrolysis. I-III. *Aluminium* (1985), **61**, pp. 251-254, 346-349, 426,428.

[15]   L. Edwards, F. Vogt, M. Robinette, R. Love, A. Ross, M. McClung, R.J. Roush and W. Morgan. Use of Shot Coke as an Anode Raw Material. *Light Metals* (2009), pp. 985-990.

[16]   C. Sommerseth. *The Effect of Production Parameters on the Performance of Carbon Anodes for Aluminium Production.* PhD thesis. Norwegian University of Science and Technology, 2016.

[17] A. Kisza, J. Thonstad and T. Eidet. An Impedance Study of the Kinetics and Mechanism of the Anodic Reaction on Graphite Anodes in Saturated Cryolite-Alumina Melts. *J. Electrochem. Soc.* (1996), **143**(6), pp. 1840-1847.

[18] W.E. Haupin. Electrochemistry of the Hall-Heroult process for aluminum smelting. *J. Chem. Educ.* (1983), **60**(4), pp. 279.

[19] G.S. Picard, E.C. Prat, Y.J. Bertaud and M.J. Leroy. Evidencing the Electrochemical Mechanism at Carbon/Bath Interface by Means of Impedance Measurement: An Improved Approach to the Aluminum Reduction Process. *Light Metals* (1987), pp. 507-517.

[20] R.J. Thorne, C. Sommerseth, A.M. Svensson, A.P. Ratvik, S. Rørvik, E. Sandnes, L.P. Lossius and H. Linga. Correlation between Coke Type, Microstructure and Anodic Reaction Overpotential in Aluminium Electrolysis. *J. Electrochem. Soc.* (2015), **162**(12), pp. E296-E307.

[21] R.J. Thorne, C. Sommerseth, A.M. Svensson, A.P. Ratvik, S. Rørvik, E. Sandnes, L.P. Lossius and H. Linga. Bubble Evolution and Anode Surface Properties in Aluminium Electrolysis. *J. Electrochem. Soc.* (2015), **162**(8), pp. E104-E114.

[22] K. Grjotheim and H. Kvande. *Introduction to Aluminium Electrolysis: Understanding the Hall-Héroult Process.* 2nd ed. Aluminium-Verlag: Düsseldorf, 1993.

[23] W. Gebarowski, C. Sommerseth, A.P. Ratvik, E. Sandnes, L.P. Lossius, H. Linga and A.M. Svensson. Interfacial Boundary between Carbon Anodes and Molten Salt Electrolyte. *Light Metals* (2016), pp. 883-888.

[24] R.J. Thorne, C. Sommerseth, A.M. Svensson, E. Sandnes, L.P. Lossius, H. Linga and A.P. Ratvik. Understanding Anode Overpotential. *Light Metals* (2014), pp. 1213-1217.

[25] W. Gebarowski, A.P. Ratvik, S. Rørvik, L.P. Lossius, H. Linga and A.M. Svensson. Effect of Coke Properties on the Bubble Formation at the Anodes During Aluminium Electrolysis in Laboratory Scale. *Light Metals* (2017), pp. 1203-1211.

[26] J.A. Leistra and P.J. Sides. Hyperpolarization at gas evolving electrodes—II. Hall/heroult electrolysis. *Electrochimica Acta* (1988), **33**(12), pp. 1761-1766.

[27] S.F. Jones, G.M. Evans and K.P. Galvin. Bubble nucleation from gas cavities — a review. *Adv. Colloid Interface Sci.* (1999), **80**(1), pp. 27-50.

[28] J. Zoric and A. Solheim. On gas bubbles in industrial aluminum cells with prebaked anodes and their influence on the current distribution. *J. Appl. Electrochem.* (2000), **30**, pp. 787-794.

[29] K.E. Einarsrud. *A Treatise on Interpolar Transport Phenomena.* PhD thesis. Norwegian University of Science and Technology, 2012.

[30]   K.E. Einarsrud and S.T. Johansen. Modelling of bubble behaviour in aluminium reduction cells. *Prog. Comput. Fluid Dyn.* (2012), **12**(2-3), pp. 119-130.

[31]   L. Cassayre, T. A. Utigard and S. Bouvet. Visualizing Gas Evolution on Graphite and Oxygen-Evolving Anodes. *JOM* (2002), **54**, pp. 41-45.

[32]   Z. Zhao, Z. Wang, B. Gao, Y. Feng, Z. Shi and X. Hu. Observation of Anodic Bubble Behaviors Using Laboratory Scale Transparent Aluminium Electrolysis Cells. *Light metals* (2015), **2015**, pp. 801-806.

[33]   K.E. Einarsrud and E. Sandnes. Anodic Voltage Oscillations in Hall-Heroult Cells. *Light Metals* (2011), pp. 555-560.

[34]   L. Kiss. Transport processes and bubble driven flow in the Hall-Heroult cell. *Proceedings of the Fifth International Conference on CFD in the Process Industries* (2006), pp. 1-7.

[35]   L.I. Kiss and S. Poncsák. Effect of the Bubble Growth Mechanism on the Spectrum of Voltage Fluctuations in the Reduction Cell. *Light Metals* (2002), pp. 217-223.

[36]   R.J. Aaberg, R.J. Ranum, W. K. and B.J. Welch. The Gas under Anodes in Smelting Cells. Part II: Gas Volume and Bubble Layer Characteristics. *Light Metals* (1997), pp. 341-346.

[37]   K.E. Einarsrud, I. Eick, P.J. Witt, A. Solheim and Y. Feng. Impact of Variable Bath Chemistry and Wetting on Gas Bubble Flow in Aluminium Electrolysis Cells. *Light Metals* (2016), pp. 649-654.

[38]   C. Sommerseth, R.J. Thorne, A.P. Ratvik, E. Sandnes, S. Rørvik, L.P. Lossius, H. Linga and A.M. Svensson. Electrochemical Reactivity and Wetting Properties of Anodes Made from Anisotropic and Isotropic Cokes. *Light Metals* (2016), pp. 865-870.

[39]   S. Jarek and J. Thonstad. Double-layer capacitance and polarization potential of baked carbon anodes in cryolite-alumina melts. *J. Appl. Electrochem.* (1987), **17**(6), pp. 1203-1212.

[40]   J. Thonstad. The electrode reaction on the C, CO2 electrode in cryolite-alumina melts—II. Impedance measurements. *Electrochim. Acta* (1970), **15**(10), pp. 1581-1595.

[41]   S. Jarek and Z. Orman. The Faradaic Impedance of the Carbon Anode in Cryolite-Alumina Melt. *Electrochim. Acta* (1985), **30**(3), pp. 341-345.

[42]   S. Jarek and J. Thonstad. Wetted Surface Area and Polarization Potential of Carbon Anodes in Cryolite-Alumina Melts. *Light Metals* (1987), pp.

[43]   S. Pietrzyk and J. Thonstad. Influence of the Sulphur Content in the Carbon Anodes in Aluminium Electrolysis – a Laboratory Study. *Light Metals* (2012), pp. 657-664.

[44]   G. Jahrsengene, H.C. Wells, S. Rørvik, A.P. Ratvik, R.G. Haverkamp and A.M. Svensson. A XANES Study of Sulfur Speciation and Reactivity in

Cokes for Anodes Used in Aluminum Production. *Metall. Mater. Trans. B* (2018), **49**(3), pp. 1434-1443.

[45]   G. Jahrsengene, S. Rørvik, A.P. Ratvik, L.P. Lossius, R.G. Haverkamp and A.M. Svensson. Reactivity of Coke in Relation to Sulfur Level and Microstructure. *Light Metals* (2019), pp. 1247-1253.

[46]   G. Jahrsengene, H.C. Wells, C. Sommerseth, A.P. Ratvik, L.P. Lossius, R.G. Haverkamp and A.M. Svensson. Vanadium Speciation in Petroleum Cokes for Anodes used in Aluminium Electrolysis. *TRAVAUX - Proceedings for the ICSOBA Conference* (2017), **46**, pp. 617-624.

[47]   L.P. Lossius, I. Holden and H. Linga. The Equivalent Temperature Method for Measuring the Baking Level of Anodes. *Light Metals* (2006), pp. 609-613.

[48]   D.A. Harrington and B.E. Conway. ac Impedance of Faradaic Reactions Involving Electrosorbed Intermediates—I. Kinetic theory. *Electrochim. Acta* (1987), **32**(12), pp. 1703-1712.

[49]   M. Orazem, I. Frateur, B. Tribollet, V. Vivier, S. Marcelin, N. Pebere, A. Bunge, E. White, D. P. Riemer and M. Musiani. Dielectric Properties of Materials Showing Constant-Phase-Element (CPE) Impedance Response. *J. Electrochem. Soc.* (2013), **160**, pp. C215-C225.

[50]   L.P. Lossius, M. Lubin, L. Edwards and J. Wyss. Relationships between Coke Properties and Anode Properties — Round Robin 19. *Light Metals* (2013), pp. 1183-1188.

[51]   A.M. Martinez, O. Paulsen, A. Solheim, H. Gudbrandsen and I. Eick. Wetting Between Carbon and Cryolitic Melts. Part I: Theory and Equipment. *Light Metals* (2015), pp. 665-670.

[52]   A. Solheim, H. Gudbrandsen, A.M. Martinez, K.E. Einarsrud and I. Eick. Wetting Between Carbon and Cryolitic Melts. Part II: Effect of Bath Properties and Polarisation. *Light Metals* (2015), pp. 671-676.

[53]   C. Sommerseth, R. Thorne, W. Gebarowski, A.P. Ratvik, S. Rørvik, H. Linga, L.P. Lossius and A.M. Svensson. Electrochemical Behaviour of Carbon Anodes Produced with Different Mixing Temperatures and Baking Levels—A Laboratory Study. *Light Metals* (2019), pp. 1311-1318.

[54]   J. Thonstad. Double layer capacity of graphite in cryolite-alumina melts and surface area changes by electrolyte consumption of graphite and baked carbon. *J. Appl. Electrochem.* (1973), **3**(4), pp. 315-319.

Chapter 8 Conclusions

This study focused on characterising the sulfur and metal impurities present in selected, calcined petroleum cokes used in the aluminium industry, and the effects the coke properties have on the electrochemical behaviour of anodes made from these cokes.

When investigating the sulfur speciation by XANES, it was discovered that some cokes had significant different sulfur chemistry than others. The work showed two key types of sulfur; the expected organic sulfur was present in all cokes, as polycyclic thiophene and thiazines, and a significant amount of an unidentified sulfide compound (S-S bound sulfur) was identified in some cokes. The presence of large quantities of this sulfur type has not previously been identified in cokes, using XANES or other methods. The fraction of the different sulfur types was independent of the total sulfur content in the coke, and was observed in both isotropic and anisotropic cokes. The quantity of S-S bound sulfur was further observed to correlate well with CO_2 reactivity, and can possibly explain cokes diverging from the expected trend of reducing CO_2 reactivity with increasing total sulfur content. S-S sulfur also correlated with the portion of small pores (pore diameter < 50 nm). The results can provide useful knowledge for optimising the coke blends with respect to level of sulfur, as it was clear that the increased total level of sulfur not necessarily meant improving the CO_2 reactivity. Sulfur chemistry can also be assumed to be an important factor to improve the understanding of desulfurization during the calcination.

The metals, Ni, V, and Fe, was found by XANES and EXAFS to be present in the cokes as hexagonal sulfides, possibly using the aromatic carbon compounds as templates to form. The metals are present as soluble organometallic complexes, and as such, highly dispersed in crude oil, and the results indicate that the formed metal sulfides are also dispersed in the coke and not present as inclusions. The total metal sulfide amount does not correlate with the S-S sulfur identified, clearly signifying that the S-S sulfur identified by S XANES is another type of sulfide. In contrast to the varying sulfur chemistry found in different cokes, the metal chemistry was the same for the cokes investigated.

The anisotropic anodes with similar physical properties, but a large variation in the level of sulfur and metallic impurities, showed a similar electrochemical behaviour. The isotropic anode had a significantly lower potential oscillations and screening related to the growth and release of CO_2 bubbles on the anode surface

than most of the anisotropic anodes. This effect is likely caused by a combination of coke and anode properties. A higher double layer capacitance for isotropic cokes compared to anisotropic cokes were observed; the capacitance is approximately 30 $\mu F/cm^2$ higher for the isotropic anode. This implies a higher electrochemically active surface area for the isotropic cokes. One of the anisotropic anodes, the low-sulfur anode, showed similar electrochemical behaviour as the isotropic anode when evaluating the effect of bubbles, however, the electrochemically active area was similar to the remaining anisotropic anodes. These observations were attributed to the high, non-ideal permeability for this anode rather than the impurities. The fact that impurities do not affect negatively the electrochemical reactivity is a positive observation from an industrial perspective, as their focus can be on handling the sulfur emissions relating to using higher sulfur cokes rather than the effect it has on the electrochemical performance

Chapter 9 Ideas for Further Research

Further research includes expanding the coke knowledge obtained in this study, and transfer the information acquired on coke properties to the electrochemical behaviour. The following focus points are suggested.

Generally, a **larger selection of cokes** should be investigated to say something about certain trends relating to the different observations in this study. 3-5 points cannot be used to identify possible linear trends. Cokes in the entire relevant range of S content should be investigated, ideally with both a linear correlation between S and V content, and several cokes diverging from this trend. Expanding the knowledge on more cokes would make a better basis for choosing cokes to make pilot anodes (the electrochemical tests are very time consuming). Also, a wider selection of isotropic cokes should be included, to determine whether the significant differences observed for the one isotropic coke in this study is also observed for other isotropic cokes.

The XAS studies, especially the **S *K*-edge XANES study**, could easily be expanded as the method was simple and close to automatic. After initially beginning a large series of samples, little to no manual interruptions was needed, in contrast to many other synchrotron investigations requiring frequent change of samples and manually starting each measurement. The results were also very repeatable for the coke materials, demanding few parallels. An expansion could include

- More coke types
- Different coke particle sizes
- Investigating the sulfur "history", by investigating green coke, coke calcined at several different temperatures as well as over-calcination, and possibly baked anodes
- A more specific S reference selection, to more easily identify the correct S-S sulfur type (and more details on the organic sulfur type)

Some cokes, with identical total sulfur content and otherwise similar coke properties, have previously been shown to have a very large difference in **desulfurization rate**. Is this correlating to the S-S content or other differences regarding sulfur speciation? Desulfurization during baking is for many smelters an extremely important factor and finding a method to identify cokes with high

and low desulfurization without the time-consuming methods used today is economically motivated.

If S-S truly is affecting the CO_2 reactivity, desulfurization or other important parts of the electrolysis process, more investigations on how to **identify the S-S sulfur** by other means than XAS methods should be done. Is it possible to distinguish higher S content using SEM and EDS? Is a difference observed by doing gas chromatography on evolved gases during heating of coke? Does it correlate with other properties more easily measured?

The electrochemical investigations showed that the anisotropic anode with significantly higher **permeability** (and lower density) exhibited the same effects as the isotropic anode regarding bubble behaviour. This should be further investigated by fabricating anodes with variable permeability, density and coke quality, and do the electrochemical characterisation. Due to problems packing with spherical isotropic grains, this is also suggested for isotropic anodes, to better be able to identify if the positive effect for the isotropic anodes are based on the coke properties, anode properties, or a combination of the two.

Anodes can be made both by the single source cokes, and by choosing to **blend** the cokes based on e.g. isotropy, S-S content and CO_2 reactivity. Possible combinations to investigate chemically and electrochemically to compare with the single source anodes include (but are not limited to) blending

- Low and high sulfur anisotropic cokes with similar sulfur speciation
- Low and high sulfur anisotropic cokes with dissimilar sulfur speciation (varying amount of S-S sulfur)
- Regular anode coke with different types of isotropic cokes
- Choose cokes based on CO_2 reactivity

To expand the understanding of the electrochemical behaviour the anodes should be tested for **wettability** with electrolyte (and the effect of polarisation).

The lab scale results should also be verified with respect to more **industrial related considerations**. This includes larger fractions, larger anodes, and a more relevant alumina content.

APPENDICES

Appendix A   Characterisation of Horizontal Anodes

A.1 Chronopotentiometry
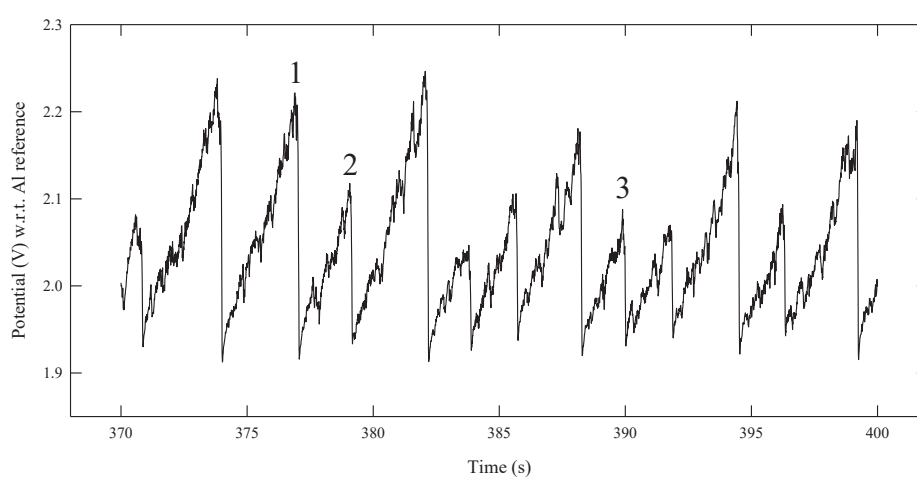
Figure A.1: Examples of bubbles measured at 1.0 A/cm^2 for one parallel of anode D, with 10 Hz sampling frequency, showing different bubble sizes but similar growth rate (see details on bubble 1, 2 and 3 in Table A.1).

Table A.1: Evaluation of the three marked bubbles in Figure A.1, showing the same growth rate.

Bubble	Δt (s)	ΔE (V)	$\Delta E/\Delta t$ (V/s)
1	3.05	0.301	0.099
2	2.11	0.205	0.097
3	1.73	0.175	0.101
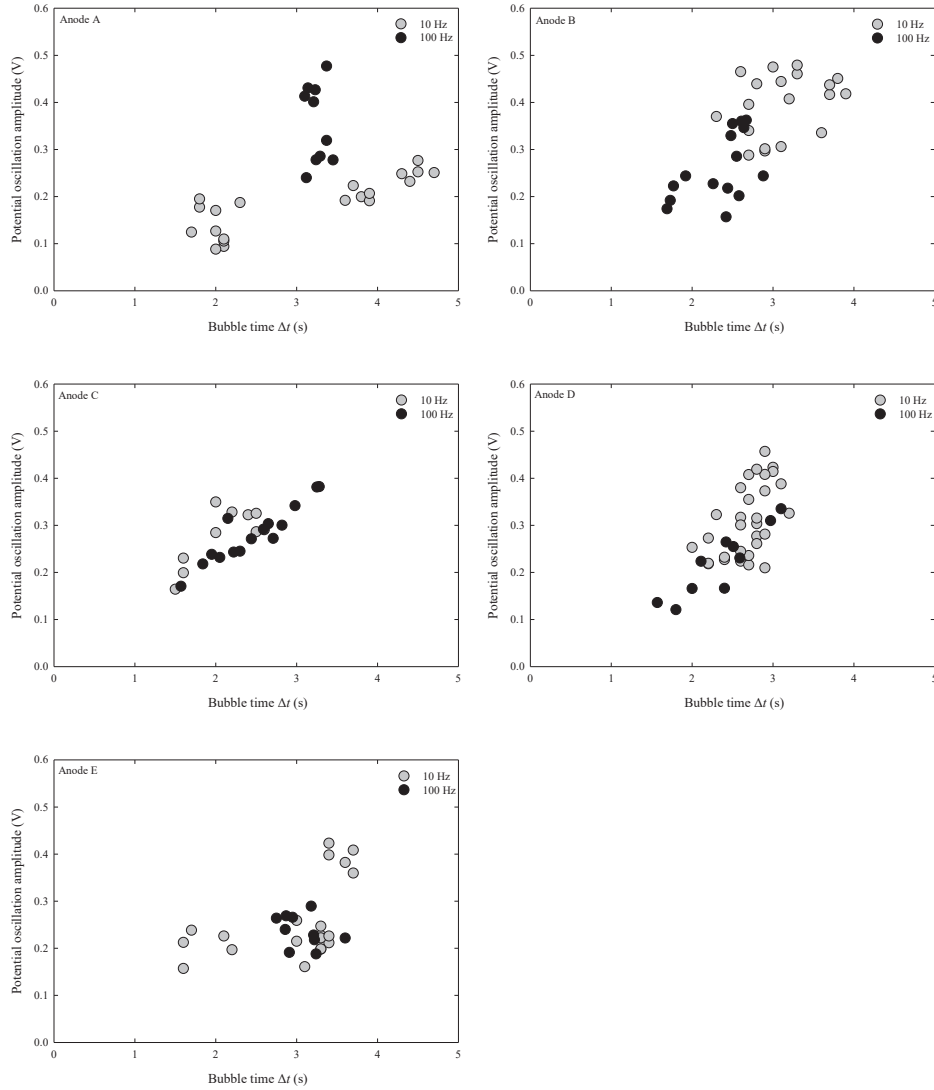
Figure A.2: The relationship between bubble oscillation amplitude and bubble time Δt extracted for five bubble periods near the end of 400 s at 1.0 A/cm^2 was approximately linear.

(a)   **(b)**
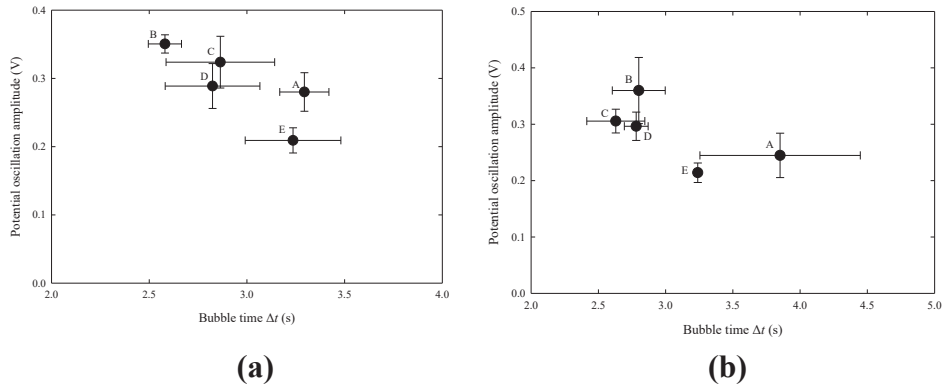
Figure A.3: Comparison between the potential oscillation amplitude and bubble time for **(a)** averages for five bubbles for *one* parallel obtained with 100 Hz sampling frequency and **(b)** average of all bubbles for *3-4 parallels*. The anodes with higher amplitude also have faster forming bubbles.
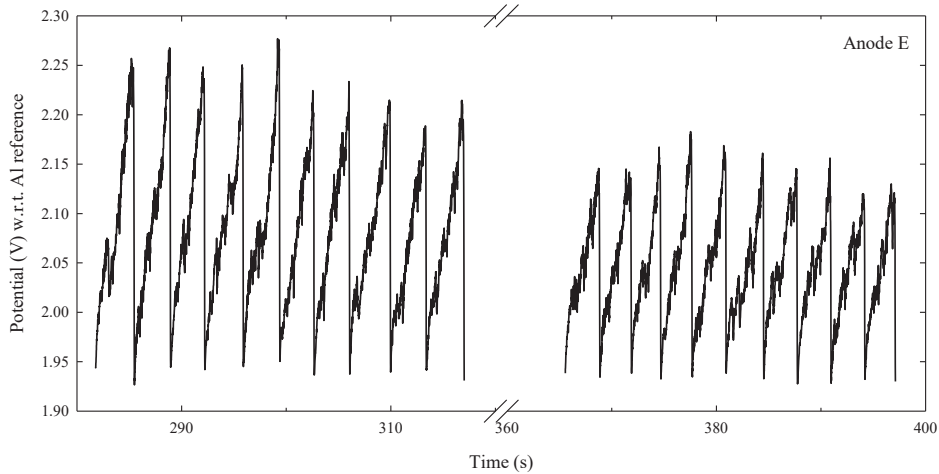
Figure A.4: The potential oscillations for the first 10 bubbles and last 10 bubbles included in the FFT analysis for one parallel of anode E at 1.0 A/cm^2. There is a clear trend of decreasing amplitude and Δt during the two minute period, which is reflected in the wider frequency distribution when evaluating the FFT results.

Table A.2: Comparison between Δt from analysing five bubbles at the end of the two minute period and the maximum peak from the FFT analysis for the two minute period. The grey parallels are obtained with higher sampling frequency (100 per second *vs* 10 per second).

Anode	Parallel	Oscillation amplitude (V)	Δt from 5 bubble analysis (s)	Δt from FFT max peak (s)	Comment on FFT result
A	1	0.280	3.29	3.23	-
	2	0.252	4.48	4.44	-
	3	0.202	3.78	3.64	-
B	1	0.351	2.58	2.67	-
	2	0.306	2.86	3.00	-
	3	0.423	2.96	3.00	-
C	1	0.324	2.86	3.25	Wide peak, higher frequency match better
	2	0.311	2.44	2.40	-
	3	0.283	2.58	2.35	Wide peak
D	1	0.314	2.74	2.79	-
	2	0.264	2.88	2.79	-
	3	0.319	2.68	2.35	-
	4	0.289	2.82	2.45	Clearly variation in bubble size
E	1	0.233	3.26	4.13	Wide, another at higher frequency better
	2	0.200	3.22	2.79	Wide peak
	3	0.209	3.24	3.53	Wide peak, see Figure A.4
Graphite	1	0.450	1.77	1.79	-
	2	0.423	1.72	1.74	-
	3	0.457	1.88	1.90	-
	4	0.395	1.78	1.82	-

A.2 Chronoamperometry

Table A.3: The calculated bubble screening by formed CO_2 bubble obtained at 2.0 V. The average current density is calculated based on the first 30 seconds and the geometric area of the sample. The average current density is around 1 A/cm^2 for the greyed out anode data (higher sampling frequency), and higher for the parallels obtained a different day (lower sampling frequency) due to different reference electrode.

Anode	Parallel	Screening (%)	Average i (A/cm^2)
	1	43.2	1.01
A	2	40.6	1.37
	3	36.0	1.39
	1	45.3	0.92
B	2	43.2	1.20
	3	55.2	1.24
	1	49.4	0.90
C	2	27.5	1.23
	3	41.3	0.97
	1	37.6	1.22
D	2	36.4	1.24
	3	36.9	1.19
	4	42.7	0.97
	1	36.7	1.40
E	2	31.8	1.36
	3	33.3	0.97
	1	67.9	0.69
Graphite	2	64.0	0.71
	3	66.3	0.64
	4	64.3	0.63

Table A.4: Comparison between maximum surface coverage by CO_2 bubbles at 2.0 V and 2.2 V, 100 Hz sampling frequency.

	Voltage (V)	Coverage (%)	Average i (A/cm^2)
A – Parallel 1	2.0	43.2	1.01
	2.2	43.8	1.31
B – Parallel 1	2.0	45.3	0.92
	2.2	48.2	1.22
C – Parallel 1	2.0	49.4	0.90
	2.2	53.1	1.21
D – Parallel 4	2.0	42.7	0.97
	2.2	45.7	1.26
E – Parallel 3	2.0	33.3	0.97
	2.2	33.3	1.32
Graphite – Parallel 1	2.0	67.9	0.69
	2.1	65.5	0.92
	2.2	63.9	1.20
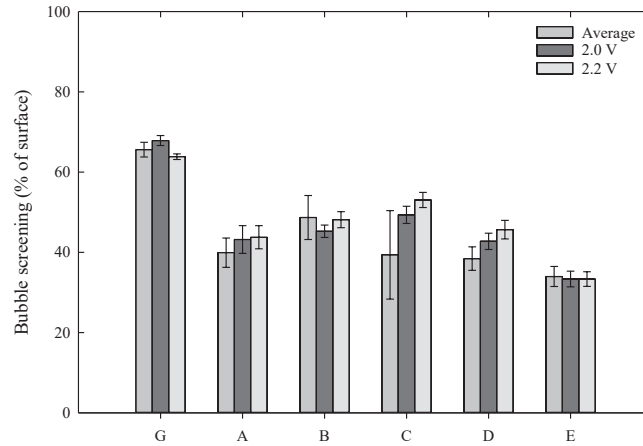
Figure A.5: The bubble screening the surface with different voltages for one single sample compared to the average for all the samples. The standard deviation for the average is for all (3-4 samples), while the standard deviation for the different voltages is for the 5 bubbles that were included in the analysis using the high frequency measurements (only one parallel sample, see Table A.4).
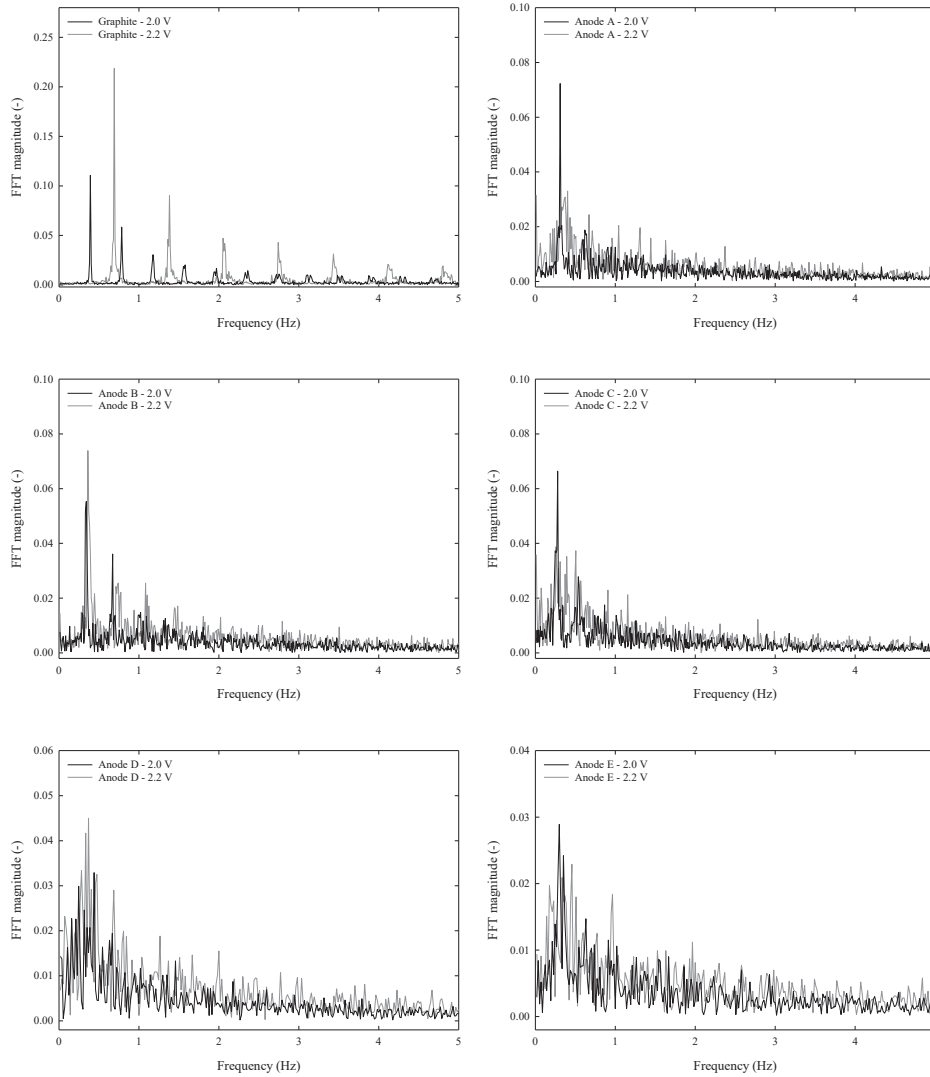
Figure A.6: The frequency distribution from the FFT analysis of the 60 seconds of constant potential 2.0 V and 2.2 V for graphite and anodes. A distinct increase in bubble frequency when increasing the voltage is observed, more so for graphite than the anodes. More noise is observed when increasing the voltage for the anodes, and wider distribution is observed.

Appendix B   Characterisation of Vertical Anodes

B.1 Potential and Overpotential

Table B.1: The average potential measured the last 50 seconds of a 400 s 1.0 A/cm^2 measurement period for graphite samples in the beginning, middle and end of the day after IR_{OCP} -correction (series resistance R_s found at Open Circuit Potential (OCP)), for two separate experimental days. The difference between the graphite is assumed equal to the variation between the Al reference the two days.

Graphite parallel	Potential last 50 s IR_{OCP}-corrected (V)	Average graphite potential same day (V)	Voltage difference each day (V)
1 – Day 1	1.760		
2 – Day 1	1.763	1.766	
3 – Day 1	1.775		
			0.059
4 – Day 2	1.827		
5 – Day 2	1.811	1.825	
6 – Day 2	1.837		
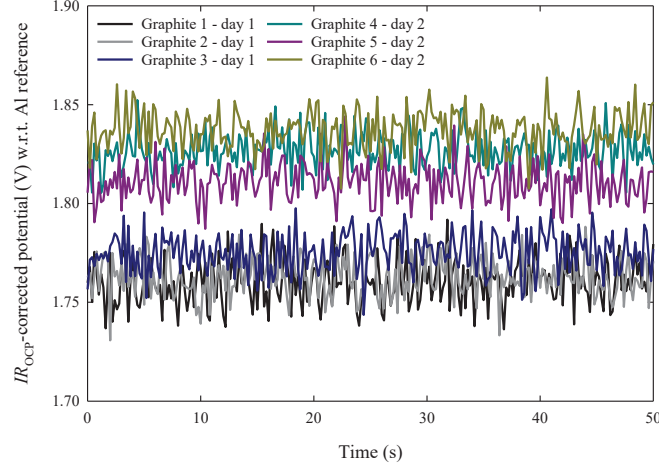
Figure B.1: The IR_{OCP}-corrected chronopotentiometry results for the two days show approximately 0.06 V difference between the days.

Table B.2: The average potential measured the last 50 seconds of a 400 s 1.0 A/cm^2 measurement period for the anode samples after IR-correction, based on the R_s found by EIS at different potentials. The grey parallels are obtained day 2.

Anode	Parallel	Potential IR-corrected by R_s found from EIS different voltages (V)			
		OCP	1.5 V	1.6 V	1.65 V
A	1	1.670	1.601	1.583	-
	2	1.769	1.689	1.637	1.613
	3	1.746	1.679	1.619	1.602
B	1	1.705	1.639	1.596	-
	2	1.677	1.616	1.585	-
	3	1.695	1.661	1.601	-
C	1	1.770	1.722	1.639	1.618
	2	1.753	1.720	1.626	1.615
	3	1.775	1.707	1.620	1.613
D	1	1.694	1.619	1.591	-
	2	1.734	1.666	1.615	-
	3	1.684	1.631	1.591	-
E	1	1.677	1.639	1.606	-
	2	1.684	1.636	1.603	-
	3	1.707	1.654	1.615	-
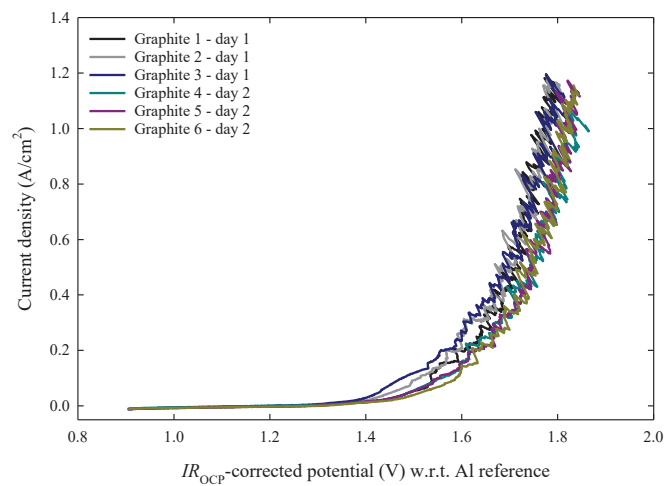
Figure B.2: The cyclic voltammetry result for the graphite samples after IR_{OCP}-correction, using the second forward scan (of three cycles) with scan rate 0.1 V/s.

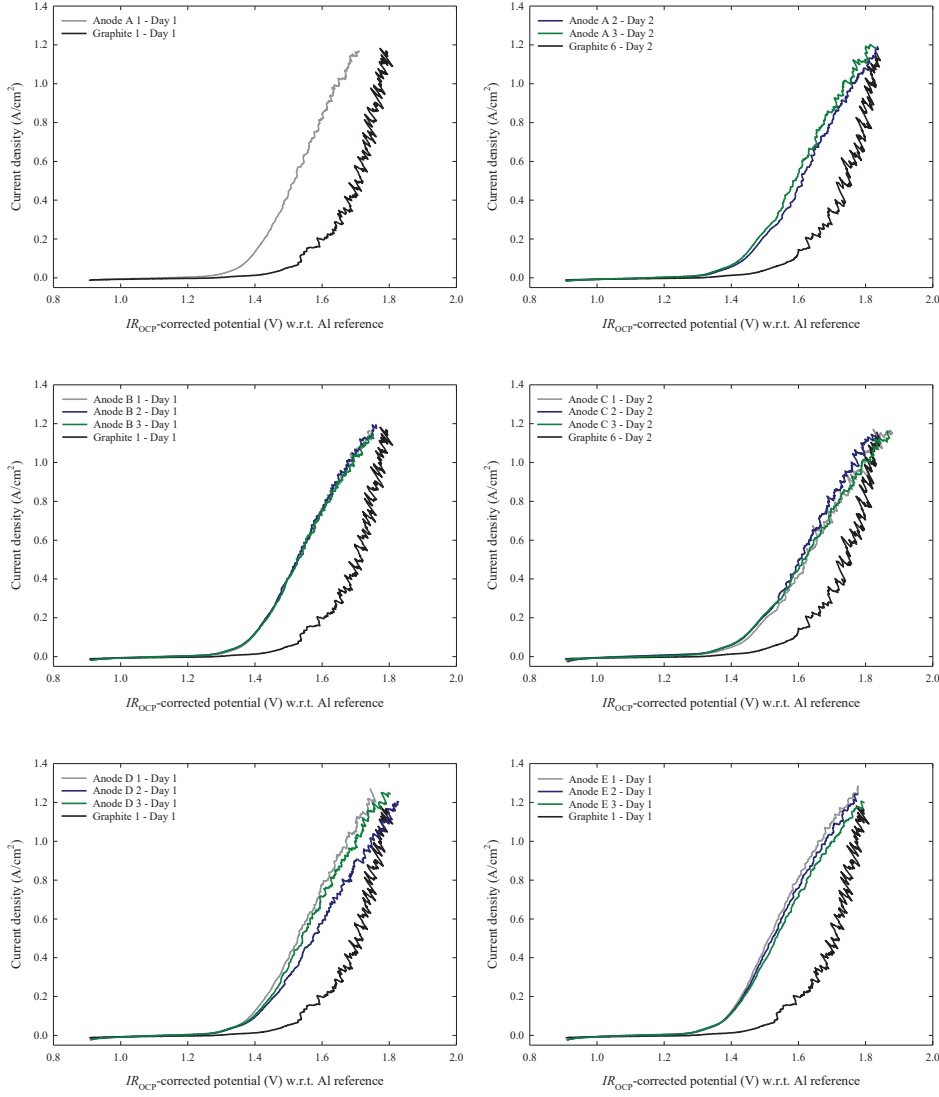**Figure B.3:** The cyclic voltammetry result for the anode samples (with a graphite parallel from the same day) after IR_{OCP}- correction, using the second forward scan (of three cycles) with scan rate 0.1 V/s for each parallel. Anode D had a large variation for one parallel while anode B had very small differences.

B.2 EIS Results

Table B.3: The best fits for the different EIS measurements for anode A at different voltages using the LR(Q(R(LR))) equivalent circuit. Parallel 1 was obtained a different day than 2 and 3.

	E (V)	i (A/cm^2)	L (H)	R_s (Ω)	Q (µF)	α (-)	$R_{ct,1}$ (Ω)	$R_{ct,2}$ (Ω)	L_{ads} (H)	C_{eff} (µF/cm^2)
1		0.19	$1.35 \cdot 10^{-6}$	0.31	170	0.96	0.19	0.06	$3.58 \cdot 10^{-4}$	71.5
2	1.5	0.12	$1.17 \cdot 10^{-6}$	0.31	579	0.83	0.31	0.05	$1.25 \cdot 10^{-3}$	58.0
3		0.13	$1.19 \cdot 10^{-6}$	0.30	436	0.86	0.29	0.05	$9.24 \cdot 10^{-4}$	63.0
1		0.33	$1.34 \cdot 10^{-6}$	0.32	142	0.98	0.11	0.05	$1.03 \cdot 10^{-4}$	71.2
2	1.6	0.23	$1.14 \cdot 10^{-6}$	0.34	290	0.90	0.17	0.05	$1.80 \cdot 10^{-4}$	61.3
3		0.23	$1.15 \cdot 10^{-6}$	0.35	184	0.94	0.16	0.05	$2.09 \cdot 10^{-4}$	60.7
1		-	-	-	-	-	-	-	-	-
2	1.65	0.30	$1.14 \cdot 10^{-6}$	0.36	178	0.95	0.13	0.04	$1.34 \cdot 10^{-4}$	65.7
3		0.30	$1.15 \cdot 10^{-6}$	0.35	246	0.92	0.12	0.05	$1.26 \cdot 10^{-4}$	63.1

Table B.4: The best fits for the different EIS measurements for anode B at different voltages using the LR(Q(R(LR))) equivalent circuit.

	E (V)	i (A/cm^2)	L (H)	R_s (Ω)	Q (µF)	α (-)	$R_{ct,1}$ (Ω)	$R_{ct,2}$ (Ω)	L_{ads} (H)	C_{eff} (µF/cm^2)
1		0.18	$1.38 \cdot 10^{-6}$	0.30	318	0.91	0.19	0.06	$3.55 \cdot 10^{-4}$	76.6
2	1.5	0.18	$1.38 \cdot 10^{-6}$	0.31	333	0.89	0.20	0.06	$3.03 \cdot 10^{-4}$	66.6
3		0.18	$1.38 \cdot 10^{-6}$	0.33	340	0.89	0.21	0.06	$3.67 \cdot 10^{-4}$	67.5
1		0.32	$1.36 \cdot 10^{-6}$	0.33	181	0.97	0.11	0.04	$9.28 \cdot 10^{-5}$	83.0
2	1.6	0.31	$1.37 \cdot 10^{-6}$	0.33	163	0.95	0.11	0.05	$9.06 \cdot 10^{-5}$	63.3
3		0.30	$1.36 \cdot 10^{-6}$	0.35	148	0.97	0.12	0.04	$9.57 \cdot 10^{-5}$	66.9

Table B.5: The best fits for the different EIS measurements for anode C at different voltages using the LR(Q(R(LR))) equivalent circuit.

	E (V)	i (A/cm^2)	L (H)	R_s (Ω)	Q (μF)	α (-)	$R_{ct,1}$ (Ω)	$R_{ct,2}$ (Ω)	L_{ads} (H)	C_{eff} (μF/cm^2)
1		0.11	1.16·10^{-6}	0.24	2741	0.69	0.35	0.05	1.28·10^{-3}	53.7
2	1.5	0.11	1.22·10^{-6}	0.29	2942	0.68	0.36	0.04	1.13·10^{-3}	49.7
3		0.13	1.19·10^{-6}	0.27	1471	0.74	0.33	0.03	5.73·10^{-4}	51.0
1		0.23	1.13·10^{-6}	0.29	547	0.83	0.18	0.05	1.72·10^{-4}	51.5
2	1.6	0.21	1.17·10^{-6}	0.35	529	0.83	0.20	0.05	1.27·10^{-4}	47.7
3		0.22	1.15·10^{-6}	0.32	385	0.86	0.18	0.05	1.36·10^{-4}	47.9
1		0.30	1.12·10^{-6}	0.30	426	0.87	0.14	0.03	8.67·10^{-5}	63.6
2	1.65	0.27	1.17·10^{-6}	0.36	220	0.91	0.15	0.04	8.17·10^{-5}	49.8
3		0.30	1.14·10^{-6}	0.33	334	0.88	0.13	0.04	5.04·10^{-5}	55.4

Table B.6: The best fits for the different EIS measurements for anode D at different voltages using the LR(Q(R(LR))) equivalent circuit.

	E (V)	i (A/cm^2)	L (H)	R_s (Ω)	Q (μF)	α (-)	$R_{ct,1}$ (Ω)	$R_{ct,2}$ (Ω)	L_{ads} (H)	C_{eff} (μF/cm^2)
1		0.19	1.28·10^{-6}	0.28	325	0.90	0.19	0.05	2.34·10^{-4}	68.9
2	1.5	0.16	1.38·10^{-6}	0.33	457	0.85	0.25	0.05	4.15·10^{-4}	55.2
3		0.17	1.39·10^{-6}	0.29	469	0.85	0.23	0.05	3.25·10^{-4}	57.2
1		0.33	1.28·10^{-6}	0.30	227	0.92	0.11	0.04	6.91·10^{-5}	62.3
2	1.6	0.27	1.33·10^{-6}	0.36	176	0.95	0.13	0.05	1.16·10^{-4}	61.5
3		0.30	1.35·10^{-6}	0.32	231	0.91	0.12	0.05	8.60·10^{-5}	56.4

Table B.7: The best fits for the different EIS measurements for anode E at different voltages using the LR(Q(R(LR))) equivalent circuit.

	E (V)	i (A/cm^2)	L (H)	R_s (Ω)	Q (μF)	α (-)	$R_{ct,1}$ (Ω)	$R_{ct,2}$ (Ω)	L_{ads} (H)	C_{eff} (μF/cm^2)
1		0.20	1.37·10^{-6}	0.29	526	0.88	0.18	0.05	3.02·10^{-4}	88.3
2	1.5	0.20	1.37·10^{-6}	0.28	535	0.87	0.19	0.05	3.00·10^{-4}	80.5
3		0.19	1.38·10^{-6}	0.29	506	0.87	0.19	0.05	3.17·10^{-4}	78.5
1		0.34	1.36·10^{-6}	0.31	322	0.94	0.10	0.04	8.44·10^{-5}	104.9
2	1.6	0.35	1.37·10^{-6}	0.30	282	0.95	0.10	0.04	8.43·10^{-5}	100.1
3		0.34	1.36·10^{-6}	0.31	265	0.95	0.10	0.04	9.07·10^{-5}	94.6

The LRC circuit, and Equations 7.7 and 7.8 was used on the high frequency data (100 000-5 000 Hz).
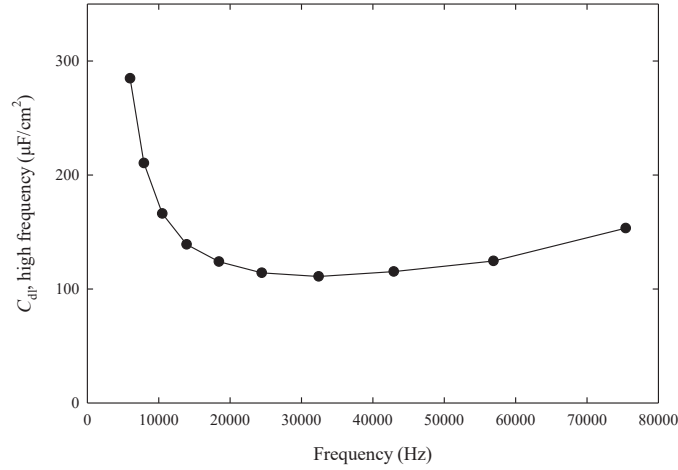

Figure B.4: Example of evaluating the double layer capacitance using the high frequency data. The capacitance is approximately constant part of this range, and an average in this specific range was used as C_{dl} for the specific parallel. The frequency range for this constant part varied greatly between samples.

Table B.8: Comparison between C_{eff} and C_{dl} for anode A at different voltages. Parallel 1 was obtained a different day than 2 and 3.

	E	i	C_{eff}	C_{eff} average	C_{dl}	C_{dl} average
	(V)	(A/cm^2)	(μF/cm^2)	(μF/cm^2)	(μF/cm^2)	(μF/cm^2)
1		0.19	71.5		78.9	
2	1.5	0.12	58.0	64.2	66.2	72.0
3		0.13	63.0		70.9	
1		0.33	71.2		84.0	
2	1.6	0.23	61.3	64.4	72.1	74.7
3		0.23	60.7		66.8	
1		-	-	-	-	-
2	1.65	0.30	65.7	64.4	81.2	76.7
3		0.30	63.1		72.1	

Table B.9: Comparison between C_{eff} and C_{dl} for anode B at different voltages.

	E	i	C_{eff}	C_{eff} average	C_{dl}	C_{dl} average
	(V)	(A/cm^2)	(µF/cm^2)	(µF/cm^2)	(µF/cm^2)	(µF/cm^2)
1		0.18	76.6		84.7	
2	1.5	0.18	66.6	70.2	77.8	80.2
3		0.18	67.5		65.6	
1		0.32	83.0		88.0	
2	1.6	0.31	63.3	71.1	77.9	80.7
3		0.30	66.9		76.3	

Table B.10: Comparison between C_{eff} and C_{dl} for anode C at different voltages.

	E	i	C_{eff}	C_{eff} average	C_{dl}	C_{dl} average
	(V)	(A/cm^2)	(µF/cm^2)	(µF/cm^2)	(µF/cm^2)	(µF/cm^2)
1		0.11	53.7		73.0	
2	1.5	0.11	49.7	51.5	69.8	70.5
3		0.13	51.0		68.6	
1		0.23	51.5		75.7	
2	1.6	0.21	47.7	49.0	68.7	68.9
3		0.22	47.9		61.9	
1		0.30	63.6		79.8	
2	1.65	0.27	49.8	56.3	65.4	70.3
3		0.30	55.4		65.6	

Table B.11: Comparison between C_{eff} and C_{dl} for anode D at different voltages.

	E	i	C_{eff}	C_{eff} average	C_{dl}	C_{dl} average
	(V)	(A/cm^2)	(µF/cm^2)	(µF/cm^2)	(µF/cm^2)	(µF/cm^2)
1		0.19	68.9		80.6	
2	1.5	0.16	55.2	60.4	67.5	72.4
3		0.17	57.2		69.1	
1		0.33	62.3		85.7	
2	1.6	0.27	61.5	60.1	69.5	74.8
3		0.30	56.4		69.0	

Table B.12: Comparison between C_{eff} and C_{dl} for anode E at different voltages.

	E	i	C_{eff}	C_{eff} average	C_{dl}	C_{dl} average
	(V)	(A/cm^2)	(μF/cm^2)	(μF/cm^2)	(μF/cm^2)	(μF/cm^2)
1		0.20	88.3		100.9	
2	1.5	0.20	80.5	82.4	93.4	95.4
3		0.19	78.5		92.0	
1		0.34	104.9		120.2	
2	1.6	0.35	100.1	99.9	113.1	113.7
3		0.34	94.6		107.8	
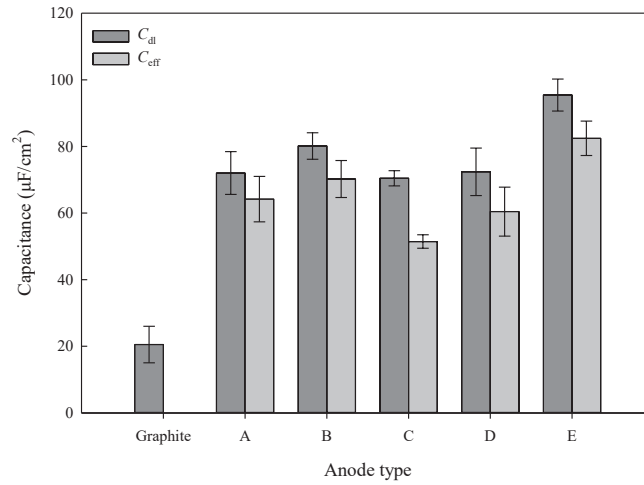
Figure B.5: Comparison between the two methods giving C_{dl} and C_{eff} at 1.5 V. C_{dl} found by using the LRC circuit and only high frequency data gives higher values than C_{eff} found by the LR(Q(R(LR))) circuit.

B.3 Reaction Kinetics and Adsorption

Equations 7.9 and 7.10 was used to assess information on reaction kinetics.

Table B.13: Kinetic and adsorption information for anode A. Parallel 1 was obtained a different day than 2 and 3.

	E	i	$1/R_{ct}$	$1/R_{ct}$ average	τ	τ average
	(V)	(A/cm^2)	(A/V)	(A/V)	(ms)	(ms)
1		0.19	4.08		7.93	
2	1.5	0.12	2.73	-	26.9	-
3		0.13	2.90		21.3	
1		0.33	6.53		8.29	
2	1.6	0.23	4.50	-	13.26	-
3		0.23	4.63		15.86	
1		-	-	-	-	-
2	1.65	0.30	5.81		4.05	
3		0.30	5.74	5.78	3.54	3.80

Table B.14: Kinetic and adsorption information for anode B.

	E	i	$1/R_{ct}$	$1/R_{ct}$ average	τ	τ average
	(V)	(A/cm^2)	(A/V)	(A/V)	(ms)	(ms)
1		0.18	3.98		7.98	
2	1.5	0.18	3.90	3.88	6.89	7.75
3		0.18	3.75		8.37	
1		0.32	6.56		8.15	
2	1.6	0.31	6.18	6.30	6.79	7.60
3		0.30	6.16		7.85	

Table B.15: Kinetic and adsorption information for anode C.

	E	i	$1/R_{ct}$	$1/R_{ct}$ average	τ	τ average
	(V)	(A/cm^2)	(A/V)	(A/V)	(ms)	(ms)
1		0.11	2.56		31.6	
2	1.5	0.11	2.45	2.58	29.2	26.8
3		0.13	2.73		19.7	
1		0.23	4.33		13.4	
2	1.6	0.21	4.02	4.22	8.78	10.5
3		0.22	4.32		9.31	
1		0.30	5.78		3.13	
2	1.65	0.27	5.19	5.59	2.42	2.38
3		0.30	5.79		1.60	

Table B.16: Kinetic and adsorption information for anode D.

	E	i	$1/R_{ct}$	$1/R_{ct}$ average	τ	τ average
	(V)	(A/cm^2)	(A/V)	(A/V)	(ms)	(ms)
1		0.19	4.12		5.86	
2	1.5	0.16	3.31	3.65	10.10	7.89
3		0.17	3.54		7.70	
1		0.33	6.40		5.55	
2	1.6	0.27	5.56	5.92	9.22	6.88
3		0.30	5.80		5.86	

Table B.17: Kinetic and adsorption information for anode E.

	E	i	$1/R_{ct}$	$1/R_{ct}$ average	τ	τ average
	(V)	(A/cm^2)	(A/V)	(A/V)	(ms)	(ms)
1		0.20	4.28		7.48	
2	1.5	0.20	4.21	4.20	7.67	7.72
3		0.19	4.11		8.02	
1		0.34	7.19		8.16	
2	1.6	0.35	7.26	7.19	8.04	8.31
3		0.34	7.13		8.74	
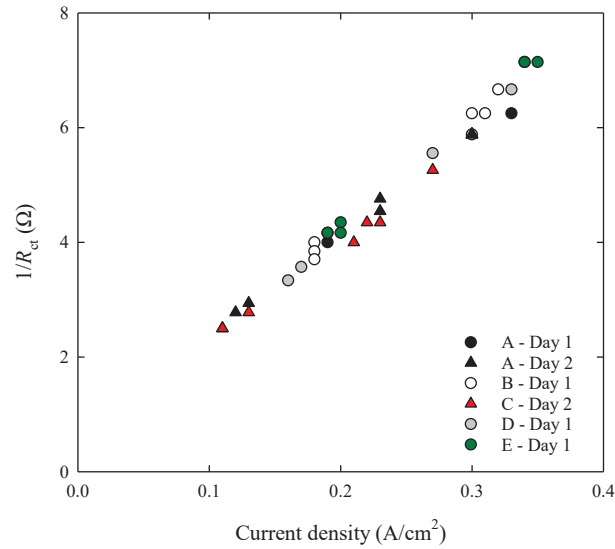
(a)
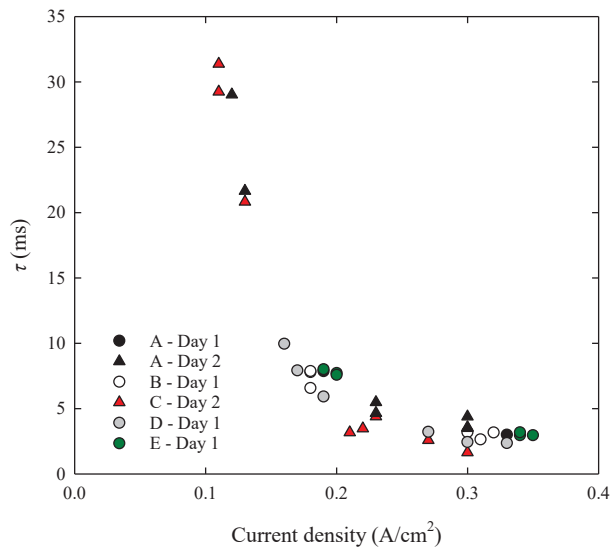
(b)

Figure B.6: The kinetic parameters **(a)** $1/R_{ct}$, which is related to the charge transfer reaction, and **(b)** τ, which is the time constant related to the speed of adsorption, plotted in the range 0.1-0.35 A/cm^2.
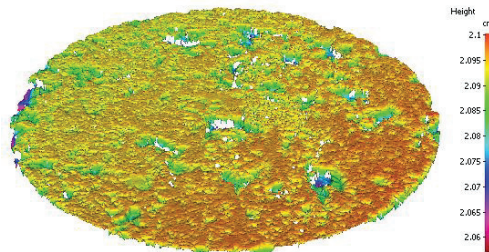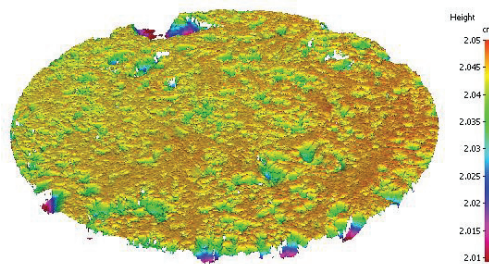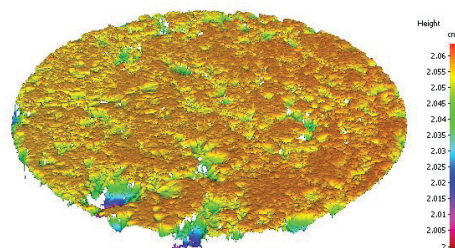
Appendix C   Confocal Microscopy Images

C.1 Roughness
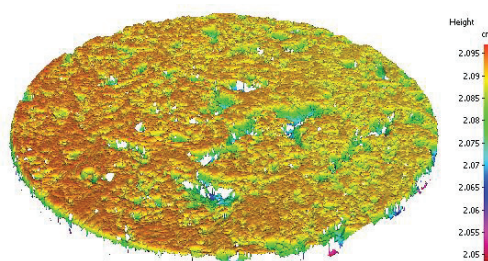
Figure C.1: Example of 3D contour image of pilot anode A obtained by confocal microscopy before electrolysis. TA/PA is 1.39. The vertical scan height is around 0.5 mm and vertical resolution is 100 nm.
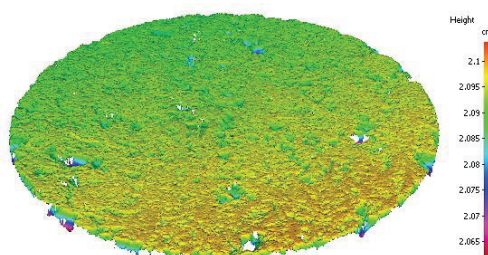
Figure C.2: Example of 3D contour image of pilot anode B obtained by confocal microscopy before electrolysis. TA/PA is 1.24. The vertical scan height is around 0.5 mm and vertical resolution is 100 nm.

Figure C.3: Example of 3D contour image of pilot anode C obtained by confocal microscopy before electrolysis. TA/PA is 1.31. The vertical scan height is around 0.5 mm and vertical resolution is 100 nm.

Figure C.4: Example of 3D contour image of pilot anode D obtained by confocal microscopy before electrolysis. TA/PA is 1.31. The vertical scan height is around 0.5 mm and vertical resolution is 100 nm.

Figure C.5: Example of 3D contour image of pilot anode E obtained by confocal microscopy before electrolysis. TA/PA is 1.29. The vertical scan height is around 0.5 mm and vertical resolution is 100 nm.

C.2 Carbon Consumption on Polished Samples
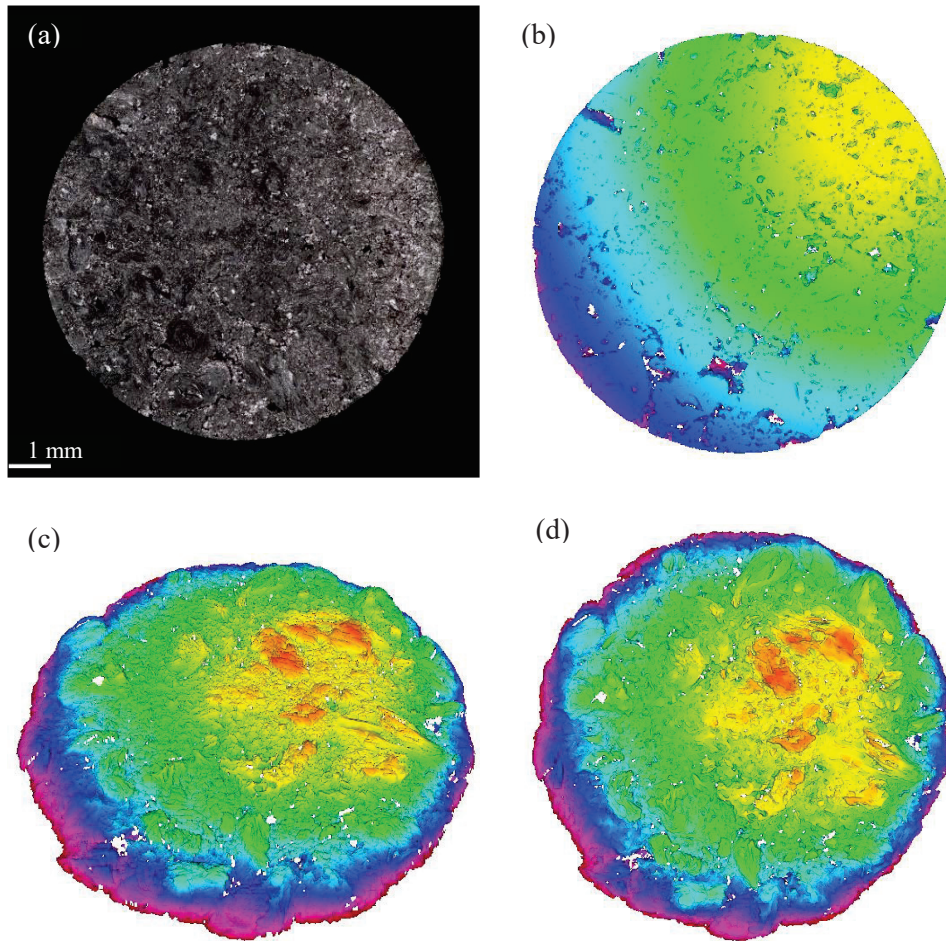
Figure C.6: Confocal microscopy images **(a)-(b)** before and **(c)-(d)** after electrolysis at 1 A/cm^2 for 40 minutes on anode A. The colour scale for contour images **(b)-(d)** is the same. The increase in surface roughness is 21.0 %.
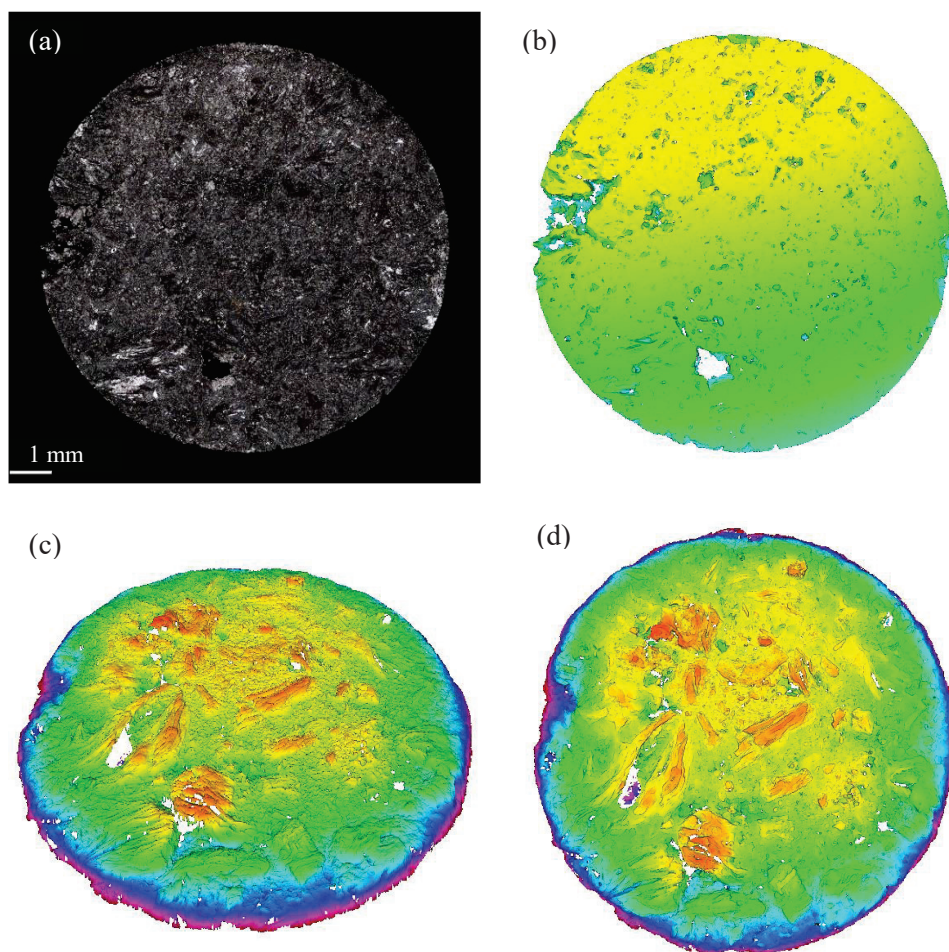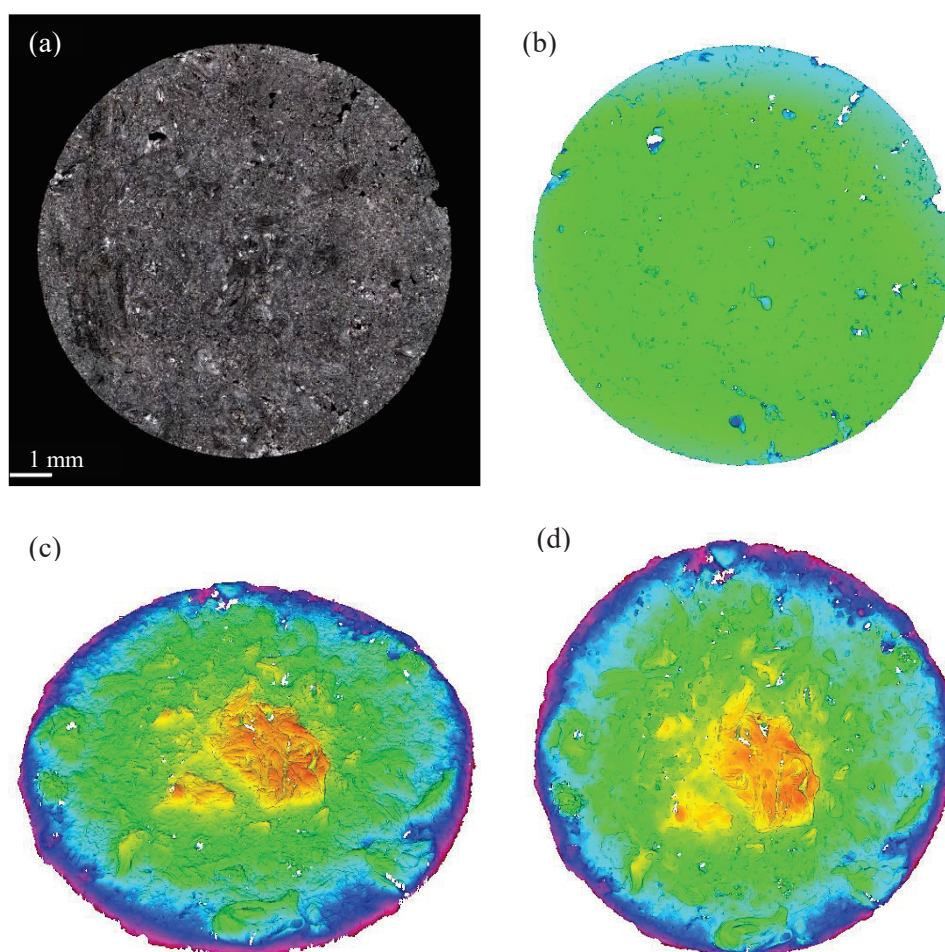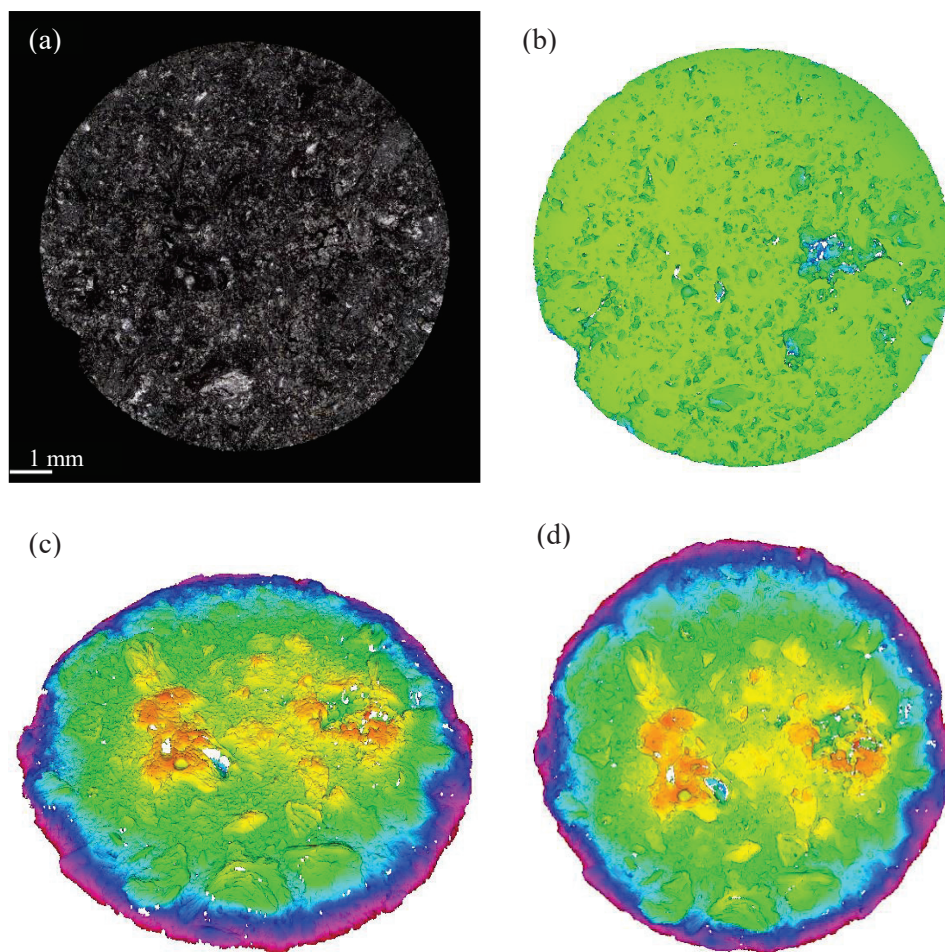
Figure C.7: Confocal microscopy images **(a)-(b)** before and **(c)-(d)** after electrolysis at 1 A/cm^2 for 40 minutes on anode B. The colour scale for contour images **(b)-(d)** is the same. The increase in surface roughness is 21.4 %.

Figure C.8: Confocal microscopy images **(a)-(b)** before and **(c)-(d)** after electrolysis at 1 A/cm^2 for 40 minutes on anode C. The colour scale for contour images **(b)-(d)** is the same. The increase in surface roughness is 17.5 %.
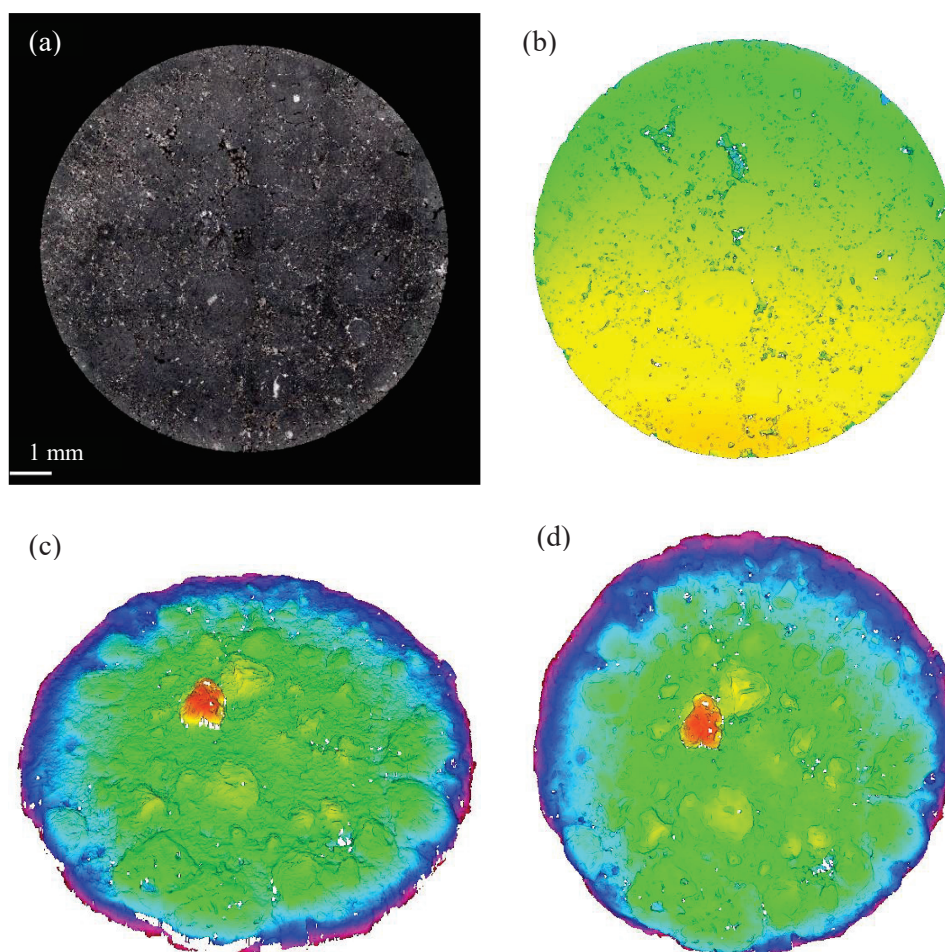
Figure C.9: Confocal microscopy images **(a)-(b)** before and **(c)-(d)** after electrolysis at 1 A/cm^2 for 40 minutes on anode D. The colour scale for contour images **(b)-(d)** is the same. The increase in surface roughness is 10.9 %.

Figure C.10: Confocal microscopy images **(a)-(b)** before and **(c)-(d)** after electrolysis at 1 A/cm² for 40 minutes on anode E. The colour scale for contour images **(b)-(d)** is the same. The increase in surface roughness is 10.1 %.
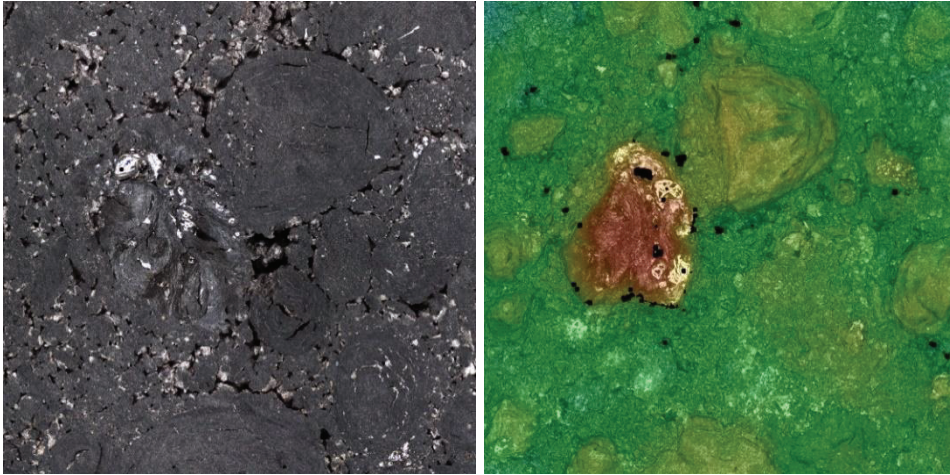
Figure C.11: Extracted visual of the significantly different grain in anode E, showing the different morphology of this grain (likely anisotropic *vs* the rest of the isotropic grains). This resulted in different consumption during electrolysis.

Appendix D   ICSOBA Paper 2017

Vanadium Speciation in Petroleum Cokes for Anodes used in Aluminium Electrolysis

Gøril Jahrsengene[1], Hannah C. Wells[2], Camilla Sommerseth[3], Arne Petter Ratvik[4], Lorentz Petter Lossius[5], Richard G. Haverkamp[6] and Ann Mari Svensson[7]

1. PhD Candidate
7. Professor
Department of Material Science and Engineering, Norwegian University of Science and Technology (NTNU), Trondheim, Norway
2. Research Fellow
6. Professor
School of Engineering and Advanced Technology, Massey University, Palmerston North, New Zealand
3. Research Scientist
4. Senior Research Scientist
SINTEF Materials and Chemistry, Trondheim, Norway.
5. Principal Engineer, Hydro Aluminium PMT, Årdalstangen, Norway
Corresponding author: goril.jahrsengene@ntnu.no

Abstract

The expanding aluminium industry is facing challenges with availability in raw materials. A wider range of petroleum cokes are being taken into use, blurring the border between anode grade and fuel grade coke in anode production. Vanadium, a common impurity in coke, is known to be a catalyst for air-reactivity burn-off, which may increase the consumption rate of the anodes. Additionally, vanadium is an unwanted impurity in the finished aluminium. Levels of vanadium and sulfur are typically correlated in petroleum cokes, but as vanadium is present mostly as porphyrins in crude oil, it is assumed this is the case in the resulting coke as well, rather than as vanadium-sulfur compounds. In this work the actual speciation of vanadium was investigated using X-ray absorption spectroscopy techniques. Six different industrial cokes were characterized with XANES, and they all seem to have the approximate same vanadium speciation. Based on the comparison with different vanadium reference standards, it was shown that vanadium is not present as the previously anticipated porphyrin. Based on the EXAFS spectrum, bonds between vanadium and sulfur were identified. Close to identical speciation of the vanadium was found in all the cokes, and this was reflected in a linear increase in air reactivity with vanadium content.

Keywords: Petroleum coke, X-ray absorption spectroscopy, vanadium speciation, air reactivity.

1.   Introduction

Carbon anodes are used in the only commercially available method for producing aluminium, the Hall-Héroult process [1]. In modern cells, pre-baked anodes with a lifetime of 25-30 days are used. The remaining anode butt is cleaned and recycled to be used in the production of new anodes. Green anodes are made by mixing calcined petroleum coke (CPC) and recycled butts together with coal tar pitch, and the formed anodes are stacked within an anode baking furnace and exposed to three-week heat treatment. As it is important to have a dense, stable and unreactive anode to achieve stable performance in the cells, anode smelters have strict requirements concerning the CPC quality. This includes bulk and real density, particle size, thermal expansion coefficient, sulfur and trace metal impurity content. All these properties have an impact on the process [2]. Because the carbon anode is consumed during the electrolysis, cost is also a consideration, meaning that very high quality and expensive coke material is unfavourable. Since petroleum coke is a by-product from the petroleum refining process, both quality and price of the coke depend on this industry rather than the aluminium industry, although a high demand from the aluminium industry may drive the price upwards.

A change in raw material quality due to changes in the petroleum industry and increased demand for anode grade coke has resulted in the need for the aluminium industry to investigate the effect of lower quality coke in anode production. Readily available coke is likely to be less dense and have more sulfur and trace metal impurities than conventional anode-grade cokes, which is believed to increase reactivity of the anode and reduce the anode stand time. Smelters have specifications on sulfur and content of vanadium, nickel, calcium, iron, silicon and sodium. These metals originate both from the precursors of the coke, and, for sodium, calcium and iron, also from the bath residue in the butts. Acceptable sulfur levels are decided based on law enforcement regarding emission of SO_2 from the plant, although smelters in some countries with strict restrictions on sulfur emissions have installed wet scrubbers. Several of the metal impurities end up in the finished aluminium, and thus the specification is determined based on the corresponding requirements of the aluminium alloys. Sulfur is in the quantity of percent rather than the metal traces of ppm, and a higher sulfur level usually also results in a higher metal impurity level. A linear correlation between sulfur and vanadium is usually observed in green coke [3], which indicates that a higher toleration of sulfur, usually obtainable by SO_2-scrubbers, also will include an increase in the level of vanadium.

Several of the impurities are known to catalyse reactions between the carbon anode and air or CO_2. Vanadium is known to be a strong catalyser for the airburn

reaction at elevated temperatures, which can cause problems if any of the anode surface is exposed to air. To avoid airburn the anode is covered with anode cover material, usually alumina. In modern cell operation the airburn is reduced due to good covering practice, but still not insignificant. The effect of vanadium on carboxy reactivity is believed to be low or moderate, but as sulfur is believed to lower this reactivity the exact effect is difficult to determine [4]. The metals are usually present in the crude oil as organometallic complexes [2], which are soluble in the crude and tend to concentrate in the residual streams and thus in the coke by-product rather than the high end products. It is believed the metals are still in this form in the coke. Vanadium is believed to be in the form of porphyrins in the coke due to its presence in the crude oil [5], but there have been little to no investigations into vanadium speciation in cokes.

X-ray absorption spectroscopy (XAS) techniques can be used to investigate speciation in many materials. Coals, chars, cokes and other organic matter have been investigated for sulfur speciation using X-ray absorption near edge spectroscopy (XANES) [6-12], but because of the low quantity of vanadium compared to sulfur, any vanadium-sulfur species will not be identified when investigating sulfur. A review of K-edge XANES of a number of vanadium compounds was done by Wong [13] in 1984 revealing a number of trends observed for the vanadium spectra, but the use of the technique to investigate carbon materials did not begin until several decades later. Duchesne [14] investigated oxidation states of V in petroleum coke gasification samples by XANES and revealed the expected differences in oxidation state from feed to by-products, but the exact specification presented here only included oxides and not organic complexes. Oil sands fluid petroleum cokes were investigated by Nesbitt [15], and using μXANES V(IV) revealed porphyrins and octahedrally coordinated V(III) were the major vanadium components.

In this work, XAS techniques are used to study six calcined petroleum cokes to determine vanadium speciation. XANES is used to identify differences between the cokes, as well as recognize the oxidation state of V. Vanadium porphyrins and vanadium sulfides could be identified by comparing the spectrum of the cokes to known vanadium reference species. The extended X-ray absorption fine structure (EXAFS) is then used to identify the probability of bonding to different atoms. Finally, any correlations of the speciation of vanadium with air reactivity are also investigated.

2.   Experimental

Six industrial CPC samples were chosen from a larger selection based on sulfur and vanadium content (determined by X-ray fluorescence), and how close the structure was to regular anode coke regarding isotropy and texture. Five cokes were anisotropic with close to typical anode coke texture, while one coke was isotropic with fine mosaic texture. Three of the anisotropic cokes had a linear relationship between sulfur and vanadium, while the last two have either higher vanadium or sulfur than the linear trend. Data for the chosen cokes is presented in Table 1. Pilot scale anodes were made using 100 % of each coke, and the anode air reactivity was measured on small test pieces using a thermogravimetric analysis method similar to ISO 12989-2:2004. Except for coke F, all the anodes were investigated for air reactivity.

Table 1. Composition the six cokes. Sulfur (S), vanadium (V) and total metal (M) content were measured on coke material using XRF. M include Na, Mg, Al, Si, Ca, V, Fe and Ni.

	S (%)	V (ppm)	M (ppm)	Notes
Coke A	1.42	116	761	Anisotropic
Coke B	3.56	402	1323	Anisotropic
Coke C	5.54	432	1356	Anisotropic
Coke D	3.86	714	1668	Anisotropic
Coke E	4.42	624	2009	Isotropic
Coke F	4.76	541	2861	Anisotropic, very high M, no air reactivity measurements performed

XAS was performed at the Australian Synchrotron using the XAS beamline in fluorescence mode. All six cokes were investigated at the vanadium K-edge, as well as the eight vanadium reference standards presented in Table 2 including vanadium foil. The reference standards were purchased from Sigma Aldrich, with the exception of V_2S_3 purchased from American Elements. The samples were ground and mounted in sample holders and loaded into the specimen chamber. The reference standards were mixed with cellulose to a concentration giving a good signal, 5000 ppm for most standards, before mounting and loading. From -10 eV to +50 eV around the K-edge (around 5465 eV) the steps were 0.25 eV, however, a larger step size was used before and after this region. The vanadium K-edge XAS spectra were processed using Athena software [16], and analysis done on the averaged spectra of three scans. All spectra were normalized by defining the signal before the pre-edge to 0 and the signal in the post-edge region to 1, and these two regions will then be presented as two parallel lines. XANES is

the region within ~50 eV from the edge, and the EXAFS region is at higher energies, with an example presented in Figure 1. The EXAFS region was investigated using the Artemis software by fitting known crystal data to the experimental spectra.

Table 2. Vanadium reference standards, concentration of V obtained by mixing with cellulose, and oxidation states.

Standard	V concentration, mixed with cellulose (ppm)	Oxidation state
Vanadium foil	-	0
V_2O_3	5000	+3
VO_2	5000	+4
V_2O_5	5000	+5
V_2S_3	5000	+3
VC	3333	+4
5,10,15,20-Tetraphenyl-21H,23H-porphine vanadium(IV) oxide	2000	+4
$VOSO_4$	5000	+4
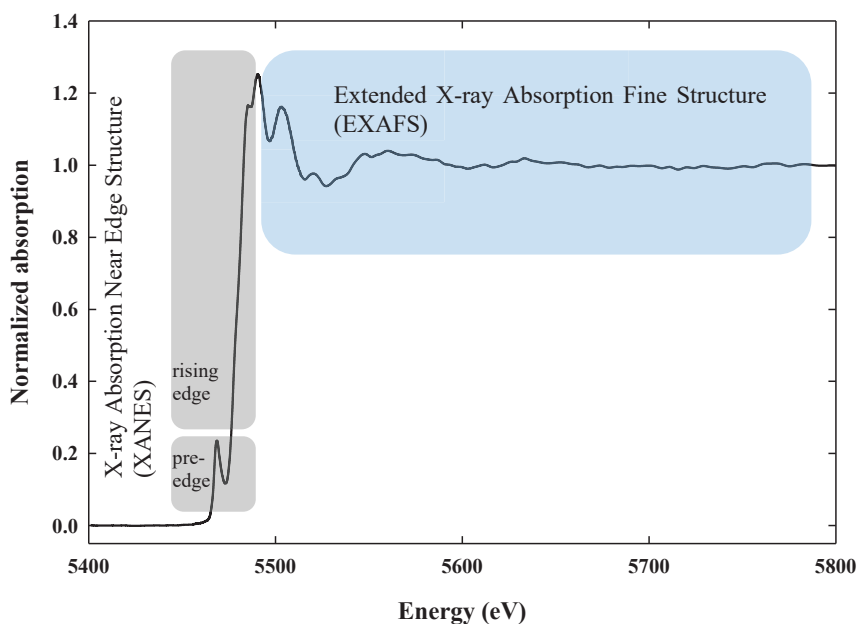
Figure 1. XAS spectrum for vanadium dioxide (VO_2).

The energy calibration from the transmission data on the foil was evaluated and it was found that the beamline was very stable in energy between scans and no corrections were needed.

3.   Results and Discussion

3.1   XAS

The vanadium reference standard XAS spectra are presented in Figure 2. The rising edge moves to higher energies with a higher oxidation state, clearly visible for the oxides in (a), and the similar oxidation state of the standards in (b) show the rising edge at approximately the same energy level. V^{3+} and V^{4+} are known to have an overlap (as well as V^{4+} and V^{5+}) at higher energies. The distinct vanadium pre-edge can be observed in all standards except for V_2O_3. This is consistent with previous data [13].
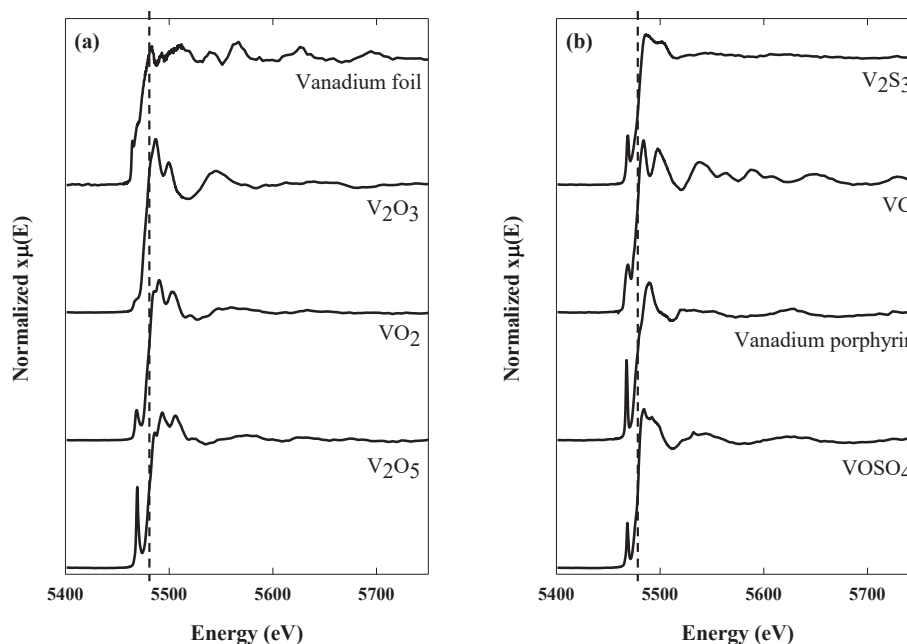
Figure 2. Vanadium K-edge XAS spectra for reference standards, (a) the vanadium foil and vanadium oxides, and (b) vanadium sulfide, carbide, porphyrin and vanadyl sulfate.

The coke XAS spectra are presented in Figure 3, and the similarities between the graphs indicate that the vanadium speciation is similar in all six cokes. A pre-edge peak, more visible in Figure 3b, is observed at 5467.5 eV. For this peak the intensity was higher for cokes A, B and D than C, E and F. None of the standards in Figure 2 had a pre-edge in this region, or an edge at these low energies, besides V foil with a pre-edge at 5464.5 eV.
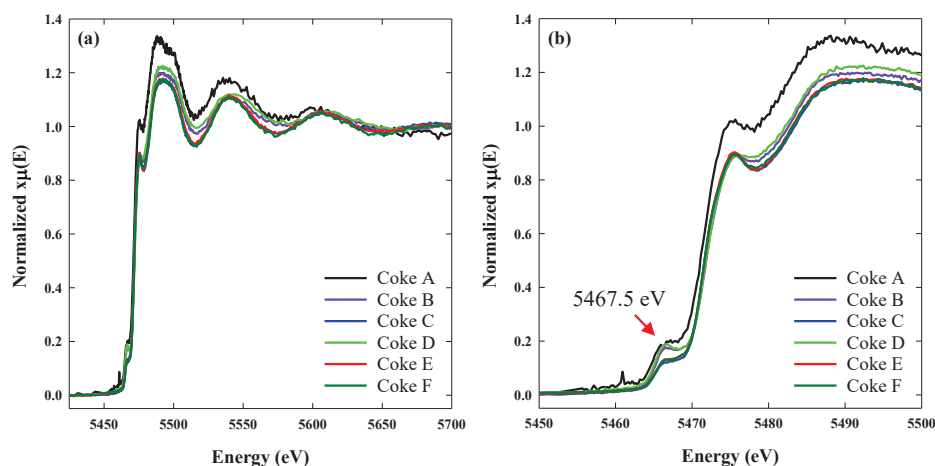

Figure 3. The vanadium K-edge XAS spectra for six industrial cokes. (a) XANES and EXAFS region and (b) XANES region only.

The edge position, located at 5471-5472 eV, is about the middle of the steep rising part, or the peak maximum of the derivative spectrum illustrated for coke D in Figure 4a (the first peak in this spectrum is the steepest part of the rise of the pre-edge, sometimes called the threshold). All the references have the edge above this value. Vanadium foil has the closest value at 5473 eV, but the pre-edge is wrong, and the general shape of the XAS spectrum is very different from the cokes' shape. Furthermore, VC has an edge a little higher than V foil, and the other references investigated in this study, including the vanadium sulfide and vanadium porphyrin, are 5-15 eV higher than the K-edge of the coke. A comparison between coke D and some of the standards is presented in Figure 4b show the differences better.
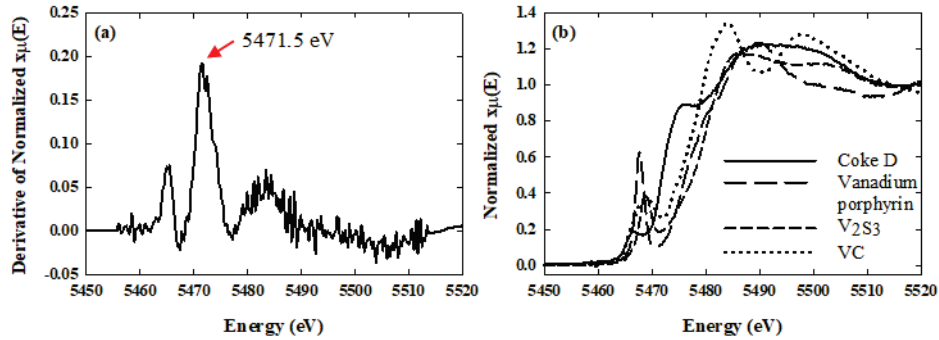
Figure 4. (a) The derivative spectrum of coke D and (b) XANES region of coke D and some reference standards.

While an XANES analysis yielded some information on vanadium speciation in the cokes, an EXAFS analysis can provide additional information on the structure and chemistry of the vanadium bonding. A preliminary EXAFS analysis suggests that the V is present as a vanadium sulfide, of which there are many possible forms. A detailed analysis will be conducted, but is outside the scope of this paper. So far it can be concluded that V_2S_3 is not the correct compound.

3.2   Evaluation of Catalysed Air Reactivity Burnoff

Air reactivity increased with increasing vanadium and metal content, as presented in Figure 5. The difference between the graphs indicates that vanadium, the metallic element most abundant in the cokes, is most likely the element with highest effect on this factor. Note that coke E, with highest total metal content, as shown in (b), has a lower reactivity than coke D which has the highest vanadium content. It appears to be an approximate linear relationship between airburn and vanadium content, with coke C deviating a little from this trend. All measurements on the anodes from coke C were practically identical, giving almost no error bar on this point, while the measurements on coke D had the largest variations.
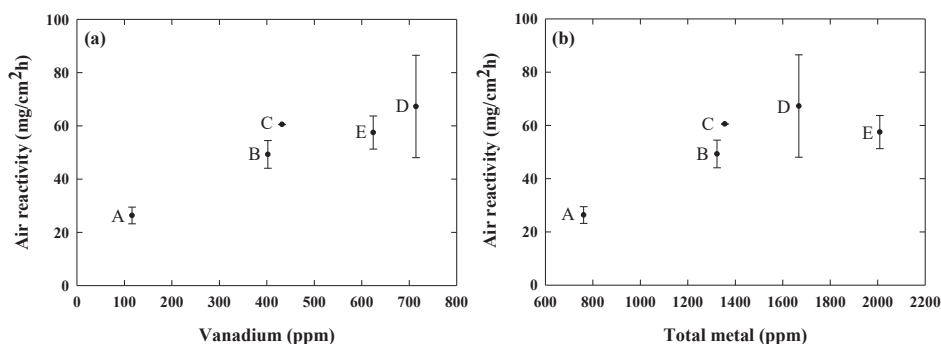
Figure 5. Air reactivity for anodes made of the cokes concerning (a) vanadium and (b) total metal content.

It is well known that vanadium is a strong catalyst for the reaction between air and carbon at the operating temperatures of electrolysis cells, something this study also shows. Despite the large uncertainty in the reactivity measurements of the anode made from coke D, the fact that this has higher reactivity than coke E, with more total metal can be taken to further illustrate the strong catalytic effect of V. Overall, these are indications that vanadium is most likely the element with the highest contribution to mass loss due to airburn. Iron is also known to be a strong airburn catalyst, and part of the high total metal content is from a doubling of this trace metal impurity in this coke, as well as much more of Al and Si, which effects are believed to be less than vanadium and iron, although not classified as weak. The XAS results showed no difference in speciation, meaning the catalytic effect of V is not a speciation dependent property. A coke with high vanadium content is expected to have higher mass loss due to reaction between air and carbon than a coke with lower vanadium content.

4.   Conclusion

Characterizing the cokes with XAS showed that the six industrial calcined petroleum cokes in this study, with vanadium content varying from 100 to 700 ppm, had the same vanadium speciation. Based on the XANES results, the previously reported vanadium porphyrin is excluded as a compound, while the preliminary EXAFS analysis shows that it is most likely vanadium in a sulfur compound that is present in these cokes. This is in good correspondence with the well known observation that vanadium and sulfur content have a significant positive correlation in cokes. The air reactivity is not a large problem during use of carbon anodes during aluminium production, however a higher reactivity correlates with higher vanadium content, which is not a speciation dependent property.

These cokes have been considered for use as anode raw material. Further understanding of how the type of vanadium bonding influences the air reactivity is clearly of interest when evaluating the risks and additional loss of materials of using these raw materials.

5.   Acknowledgement

6.   References

1.   K. Grjotheim, J. Thonstad, and C. Krohn, *Aluminium electrolysis : the chemistry of the Hall-Héroult process*. 1977, Düsseldorf: Aluminium-Verlag.
2.   L. Edwards, *Rain CII: Responding to Changes in Coke Quality*. 2007.
3.   L. Edwards, The History and Future Challenges of Calcined Petroleum Coke Production and Use in Aluminum Smelting. *JOM*. Vol. 67, No. 2, (2015), 308-321.
4.   G.J. Houston and H.A. Øye, *Consumption of anode carbon during aluminium electrolysis*. 1985, Düsseldorf: Aluminium-Verlag.
5.   J.G. Reynolds, et al., Characterization of the binding sites of vanadium compounds in heavy crude petroleum extracts by electron paramagnetic resonance spectroscopy. *Energy & Fuels*. Vol. 1, No. 1, (1987), 36-44.
6.   J.H. Cai, E. Morris, and C.Q. Jia, Sulfur speciation in fluid coke and its activation products using K-edge X-ray absorption near edge structure spectroscopy. *Journal of Sulfur Chemistry*. Vol. 30, No. 6, (2009), 555-569.
7.   S.J. Hay, J. Metson, and M.M. Hyland, Sulfur speciation in aluminum smelting anodes. *Ind. Eng. Chem. Res.* Vol. 43, No. 7, (2004), 1690-1700.
8.   M. Kasrai, et al., Sulphur characterization in coal from X-ray absorption near edge spectroscopy. *International Journal of Coal Geology*. Vol. 32, No. 1, (1996), 107-135.

9.   I.J. Pickering, et al., Sulfur K-edge X-ray absorption spectroscopy for determining the chemical speciation of sulfur in biological systems. *FEBS Letters*. Vol. 441, No. 1, (1998), 11-14.

10.   D. Solomon, J. Lehmann, and C.E. Martínez, Sulfur K-edge XANES Spectroscopy as a Tool for Understanding Sulfur Dynamics in Soil Organic Matter. *Soil Science Society of America Journal*. Vol. 67, No. 6, (2003), 1721-1731.

11.   G.S. Waldo, et al., Sulfur speciation in heavy petroleums: Information from X-ray absorption near-edge structure. *Geochimica et Cosmochimica Acta*. Vol. 55, No. 3, (1991), 801-814.

12.   M. Wang, et al., Sulfur K-edge XANES study of sulfur transformation during pyrolysis of four coals with different ranks. *Fuel Processing Technology*. Vol. 131, (2015), 262-269.

13.   J. Wong, et al., K-Edge Absorption Spectra of Selected Vanadium Compounds. *Phys. Rev. B, Condens. Matter*. Vol. 30, No. 10, (1984), 5596-5610.

14.   M.A. Duchesne, et al., Vanadium Oxidation State Determination by X-Ray Absorption Spectroscopy*, Advances in Molten Slags, Fluxes, and Salts: Proceedings of the 10th International Conference on Molten Slags, Fluxes and Salts* 2016, 1405-1412.

15.   J. Nesbitt and M. Lindsay, Vanadium Geochemistry of Oil Sands Fluid Petroleum Coke. *Environmental Science & Technology*. Vol. 51, No. 5, (2017), 3102-3109.

16.   B. Ravel and M. Newville, Athena, Artemis, Hephaestus: data analysis for X-ray absorption spectroscopy using IFEFFIT. *Journal of Synchrotron Radiation*. Vol. 12, (2005), 537-541.